Open access • Journal Article • DOI:10.1039/C8CS00887F

New trends in tailoring active sites in zeolite-based catalysts. — Source link

Mariya Shamzhy, Maksym Opanasenko, Patricia Concepción, Agustín Martínez

Institutions: Charles University in Prague, Polytechnic University of Valencia

Published on: 18 Feb 2019 - Chemical Society Reviews (The Royal Society of Chemistry)

Topics: Isomorphous substitution

New trends in tailoring the active sites in zeolite-based catalysts

Mariya Shamzhy[1], Maksym Opanasenko*[1], Patricia Concepción[2], and Agustín Martínez*[2]

[1]Department of Physical and Macromolecular Chemistry, Faculty of Science, Charles University in Prague, Hlavova 2030, 12840 Prague 2, Czech Republic.

[2]Instituto de Tecnología Química, Universitat Politècnica de València-Consejo Superior de Investigaciones Científicas (UPV-CSIC), Avenida de los Naranjos s/n, 46022 Valencia, Spain.

* Corresponding authors.

1. Introduction

The development of catalysis remarkably impacted a rapid progress of the chemical industry, improvement of the quality of human life and growth of world economy. Today over 90% of all industrial chemicals are produced with the aid of heterogeneous (~70% of the processes[1]) catalysts. The replacement of hazardous catalysts like H_2SO_4, HF, and $AlCl_3$ with acidic zeolites revolutionized the petrochemical industry in the second half of the twentieth century; the application of zeolites containing metal particles as catalysts for hydroisomerization, hydrocracking, and reforming processes have allowed the large-scale production of high-quality fuels and bulk chemicals. A combination of acid functionalities, uniform micropores providing shape selectivity, and easy regeneration are the key points by which zeolites represent a real revolution in the field of catalysis. However, a big progress achieved by using zeolite catalysts for industrially relevant processes would had been never realized without accumulating fundamental knowledge on the design of active sites, porosity and crystal morphology of these materials.

For a long time zeolites have been thought as crystalline microporous aluminosilicate frameworks built up of corner-sharing TO_4 tetrahedra (T = Si, Al). Indeed, Si^{4+} and Al^{3+} are characterized by close values of ionic radii, T–O bond lengths, and T–O–T bond angles making Al^{3+} a perfect element to isomorphously substitute Si^{4+} in zeolite frameworks. However, the possibility of changing the "fine structure" of the framework (angles and lengths of the bonds) compensating the structural strains arising during isomorphous substitution permits the incorporation of different heteroelements into zeolites allowing to tailor the nature and catalytic function of formed Brønsted and Lewis acid sites. Introducing multifunctional active centres to zeolites by simultaneous isomorphous substitution and loading with metal species of different size (single atoms, clusters, and nanoparticles) remarkably extended a scale of reactions efficiently catalyzed by zeolites.

Recent progress in the synthesis of extra-large pore zeolites and in designing the morphology of zeolite crystals using different heteroatoms as framework-building elements, and in the incorporation of metal species in zeolite voids allowed constructing both micro- and micro-mesoporous heterogeneous catalysts with specific properties. By mainly covering the investigations reported in the period 2000-2018, this review provides updated information on the recent results, achievements, and trends which we consider relevant to tune key characteristics of active sites (nature, structure, concentration) that determine the catalytic performance of zeolite-based catalysts, with a special focus on novel extra-large pore, layered (2D), nanocrystalline, and hierarchical micro-mesoporous zeolites. The first part of this review summarizes the recent achievements in isomorphous incorporation of 3- and 4-valent elements in zeolites. A particular attention is paid to the recently developed methods allowing a control over the nature and accessibility of active centres in zeolites. The role of the synthesis conditions and nature of framework-building elements on the structure of formed active sites and their acid strength is discussed and related to the catalytic behaviour of isomorphously substituted zeolites in important acid-catalyzed reactions. The second part of the review is devoted to the design of composite materials comprising zeolites and metal species of different size. Particular focus is given to the recent studies on small metal entities (single atoms and small clusters) stabilized in the voids of zeolite frameworks, and the use of nanosized and hierarchical zeolites with high accessible surfaces as supports for dispersing metal nanoparticles. The dynamic behaviour of metal species hosted in zeolites under certain reactive atmospheres, revealed thanks to the use of advanced *in situ* spectroscopic and imaging techniques with enhanced resolutions, and its implications in catalysis is also addressed. Finally, the catalytic features of metal-zeolite composites in industrially relevant processes and in emerging sustainable catalytic applications are illustrated through selected case-examples.

2. Tailoring acid sites in zeolites

2.1. General aspects of isomorphous substitution

Isomorphous substitution, i.e. replacement of framework atoms of crystalline compounds by atoms of other elements without changing the type of the crystal structure, is a key way to tune the properties of active sites in zeolite-based catalysts for particular applications.

According to one of the first theories of isomorphous substitution, proposed by Pauling[2], cations prefer tetrahedral coordination if the ratio of ionic radii $p = r_T/r_{O^{2-}}$ is in the range 0.225 – 0.414. However, being valid for ionic compounds, Pauling criteria is not strictly applicable to zeolites possessing T–O bonds of polar covalent character. Moreover, there are examples of zeolite frameworks possessing elements that can exhibit coordination states other than tetrahedral or octahedral (e.g., Be^{2+}, B^{3+}, Ti^{4+}).

Alternatively, thermodynamics treats the ability of compounds to form solid solutions from the point of view of the minimum free energy. The possibilities and limits of isomorphous substitution depend on the competition of two factors: 1) the energy consumption for the deformation of the crystal lattice caused by incorporation of atoms of different size and/or charge at regular positions of the framework, and 2) the gain of energy due to the growth of the configuration entropy with decreasing system ordering and increasing variety of the elements in the system. Isomorphous substitution is possible between atoms (ions) characterized by similar nature of the chemical bond (i.e. having close electronegativity), and close sizes (atomic or ionic radii). It is usually assumed that the critical difference for the isomorphous substitution is 15% for the radii of the ions, and the difference in the values of the electronegativity is 0.4 a.u. in the Pauling scale. These limits are very conditional and can be expanded depending on the composition/structure of the crystal and the conditions of its formation.[3]

In accordance with the aforementioned criteria, zeolite frameworks were found accepting isomorphous incorporation of Be^{2+}, Zn^{2+}, B^{3+}, Al^{3+}, Ga^{3+}, Fe^{3+}, Ge^{4+}, Ti^{4+}, and Sn^{4+}. Incorporation of tri- (T^{3+}) and tetravalent (T^{4+}) heteroatoms used for modification of the structure and properties of acid sites in zeolites is further discussed in Section 2.2, with a specific focus on recent studies addressing the effect of introduced T-elements on the structure, stability, and strength of the formed acid centres (Sections 2.2.1 and 2.2.2). The information gathered from these studies is essential for understanding the general principles of designing zeolite-based catalysts via isomorphous substitution.

2.2. Structure and properties of acid sites in zeolites

The number of $T^{3+}O_4$ units in zeolite framework controls its overall negative charge. If the charge is compensated by a proton, the resulting domain of the zeolite framework represents a Brønsted acid centre acting as active site in acid-catalyzed transformations of organic molecules.[4] Such key characteristics as the strength and density of the Brønsted acid sites influencing the activity and selectivity of zeolites are tuned by changing the type of the trivalent cation substituting silicon and its concentration in the silicate framework, respectively.[5] Moreover, it is known that during zeolite activation dehydroxylation of bridging OH groups occurs to some extent. This leads to the formation of extra-framework species, which act as electron-acceptor (i.e. Lewis acid) sites. These sites were shown to enhance the acidity of Brønsted sites, e.g. in fluid catalytic cracking (FCC), light paraffin isomerization and aromatization processes.[6] However, T^{3+}-associated Lewis acidity in zeolites is poorly understood compared to Brønsted acidity.

In contrast to T^{3+}, incorporation of tetrahedrally coordinated metals T^{4+} (e.g. Ti, Sn) into a silica framework may generate isolated Lewis acid sites, which properties can easily be tuned. The Lewis acid character arises from the partial positive charge on the metal atom that is formed when valence electrons of the metal covalently bind with adjacent framework oxygen atoms. The metal site can accept electron pairs from reactants without inducing a charge imbalance in the framework, and this can lead to chemical activation of substrates with electron-rich groups. Variation in the properties of the T^{4+} site (e.g., electronegativity, electronic configuration, coordination state, hydration) is critical in achieving high activity of the catalyst.

2.2.1. Brønsted acid centres

Trivalent elements such as B, Al, Ga, and Fe are known to be isomorphously incorporated into zeolite frameworks to generate bridging hydroxyl groups ($\equiv Si(OH)-T^{3+}\equiv$) donating or at least partially transferring the proton when interacting with basic molecules and, hence, acting as Brønsted acid sites. Recent studies on the influence of the nature of T^{3+} element on the structure, stability, and acid strength of formed Brønsted acid sites are valuable for the design of heterogeneous catalysts with desirable characteristics.

Koningsberger and Miller[7] were the first to determine the local aluminium structure associated with the zeolitic Brønsted acid site by low energy XAFS in 1994. The use of hydrated H-Y, NH_4-Y, and Na-Y samples was expected to lead to a more ordered tetrahedral site. A clear difference in local structure around the framework aluminium atom was observed when varying the charge-balancing cation (e.g. H^+ or NH_4^+, Scheme 1) in zeolite Y.

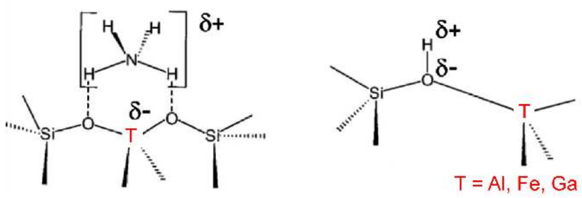

Scheme 1. Local environments of T^{3+} heteroatoms incorporated into zeolitic frameworks. Adapted from ref. [8]

Similarly to aluminium, the local environment of trivalent Fe^{3+} and Ga^{3+} hosted in the MFI framework was recently found to be tetrahedral, exhibiting 4 equivalent T^{3+}–O bonds (with lengths 1.85 Å and 1.80 Å for Fe[9] and Ga[10], respectively) in the presence of tetrapropylammonium or NH_4^+ cations. At the same time, the tetrahedral symmetry of T^{3+} is strongly distorted when the negative framework charge is compensated by a proton, showing one elongated T–O bond (2.10 Å and 1.99 Å for Fe and Ga, respectively) in ≡Si–(OH)–T^{3+}≡ bridge and three equivalent T–O–(Si) bonds (1.87 Å and 1.79 Å for Fe and Ga, respectively).

XANES results obtained for as-prepared B-SSZ-13 reveal the presence of $[B(OSi)_4]$ units with tetrahedral (Td) geometry (sp^3-hybridized B atoms). In contrast to other trivalent heteroatoms discussed above, removal of organic structure-directing agents (SDAs) caused the break of a B–O–Si bond resulting in formation of $[B(OSi)_3]$ units with D_{3h} symmetry (sp^2-hybridized B atoms).[11] The XANES study fully confirms the parallel infrared experiment, where template removal results in the appearance of the strong IR band at 1390 cm^{-1} due to the asymmetric B–O stretching of BO_3 units in D_{3h} symmetry. Such a transformation of boron coordination upon calcination/dehydration and subsequent variation of the local geometry explains the weaker acidic character of borosilicate zeolites vs. their Al-substituted counterparts.

Likewise, the stability of Ga or Fe in T positions is lower in comparison with tetrahedrally coordinated Al atoms. [12] Thus, thermal treatments frequently cause the migration of Ga or Fe to extra-framework positions and their progressive aggregation to form dimeric and then polymeric species. These Ga- and Fe-associated extra-framework Lewis acid sites were proven heavily contributing to the catalytic activity of the respective zeolites. There is evidence that enhanced aromatization on gallium-containing MFI[13, 14] and *BEA[13] zeolites is the result of a bifunctional catalytic process involving both framework and extra-framework gallium atoms. Extra-framework iron cations can show different valence states depending on the reducing or oxidizing character of the reagents present in the catalyst environment and hence, show redox properties not available in Al- or Ga-substituted analogues. Zeolites with extra-framework Fe species show high activity in, for instance, the hydroxylation of benzene to phenol with nitrous oxide,[15] the selective reduction of nitric oxide with ammonia[16], and the decomposition of N_2O.[17]

Besides stability of acid sites, the nature of the T^{3+} element (in particular, the similarity of the ionic radii of T^{3+} and Si^{4+}, and the ability of T^{3+} to exhibit tetrahedral coordination) was also shown determining the degree of silicon substitution. Thus, the degree of isomorphous substitution of Si in MFI framework is known to increase in the order: Fe (Si/Fe = 22) < Ga (Si/Ga = 18) < Al (Si/Al = 12.5).[18] Recently, the same trend was also found for extra-large pore UTL zeolites isomorphously substituted with 3-valent elements.[19]

The acid strength of the bridging $\equiv Si–(OH)–T^{3+}\equiv$ groups is another characteristic of Brønsted-acid zeolites controlled by the type of trivalent cation. Quantum chemical calculations of the deprotonation energy (DPE), which estimates the intrinsic acid strength of the protonic site, indicated an increasing DPE value and, thus, a decreasing acid strength of $\equiv Si–(OH)–T^{3+}\equiv$ groups in the sequence Al > Ga > B.[20] The order of acidity is reproduced for isomorphously substituted MFI zeolites independently on the zeolite model size, while the absolute values of DPE depend on structural models, functionals, and basis sets used.[21] The DPE values for B-, Ga-, and Al-containing extra-large pore UTL zeolites calculated at the density functional theory (DFT) level using the local density approximation (LDA) and the generalized gradient approximation (GGA) were recently shown to decrease in the following sequence: B-UTL > Ga-UTL > Al-UTL.[22] Noticeably, based on the adsorption energies of NH_3, the acid strength of Al-UTL was concluded to be comparable with that of Al-MOR. [22]

DPE values calculated for each distinct location of Si–(OH)–Al groups in zeolites MFI, *BEA, MOR, FER, FAU, and CHA using periodic DFT differ up to 77 kJ/mol, although ensemble-averaged DPE values were similar among zeolites with different topologies.[23] In contrast, the strength of Bronsted acid sites differs substantially when comparing conventional three-dimensional (3D) with layered (2D) zeolites. In particular, higher strength of acid sites in layered (DPE = 1042 – 1091 kJ/mol for Si/Al = 3 – 63) vs. 3D CHA zeolite (DPE = 1233 kJ/mol, Si/Al = 11) was concluded by Rybicky and Sauer based on hybrid quantum mechanics/molecular mechanics calculations of absolute DPE values for Brønsted sites in both materials with various Si/Al ratios. [24, 25] The result was ascribed to the smaller effective dielectric constant (1.6 – 1.9 a.u.) of an ultra-thin dielectric in vacuum compared to that of the corresponding bulk systems (3.0 a.u. for 3D CHA), which leads to a better stabilization of the charge created upon deprotonation.

2.2.2. Lewis acid centres

Commonly, Ti and Sn atoms are isomorphously incorporated into zeolite frameworks to generate isolated Lewis acid sites. The two elements possess a different electronic configuration (Sn: $5s^2 5p^2$; Ti: $3d^2 4s^2$) and atomic radius (Sn: 1.40 Å; Ti: 1.36 Å), leading to diverse distortion of the $T^{4+}O_4$ tetrahedron in the zeolite and, as a result, to different chemical properties and catalytic activity. A comparison between Ti- and Sn-based silicates is useful to understand the influence of the nature of T^{4+} on the structure and performance of Lewis acid sites in catalysis.

The isomorphous substitution of Ti in tetrahedral framework positions is straightforwardly detected in vacuum-activated zeolites by XANES spectroscopy. The typical average Ti–O distance in Ti-silicalite-1 (TS-1) is 1.79 ± 0.01 Å (Td symmetry) that moves to 1.82 and 1.83 Å upon adsorption of H_2O and NH_3, respectively[26] (Scheme 2). The incorporation of bulkier Sn distorted the zeolite framework in a higher extent: EXAFS analysis of Sn(IV) in Sn-*BEA showed that the Sn–O distance in the tetrahedrally coordinated framework Sn is as long as 1.91 Å.[27]

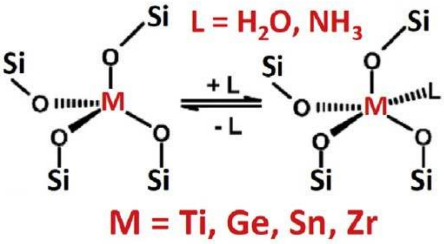

Scheme 2. Local environments of T^{4+} heteroatoms (M) incorporated into zeolitic frameworks. Vacuum-activated materials experience a Td-like environment with four equivalent M–O distances. Upon interaction with ligands (L = H_2O or NH_3) the T^{4+}-atom modifies its local environment coordinating one ligand molecule in its first coordination sphere. Adapted from ref. [8]

Further, it was observed that one Ti–O–Si bond of framework Ti^{4+} (so-called 'closed' configuration) reversibly hydrolyzed forming Si–OH and Ti–OH species ('open' sites, Scheme 3). Computational studies showed that the formation of the first Ti–OH group stabilized the metal ion in the framework, while further hydrolysis of Ti–O–Si bonds was energetically unfavourable.[28] There is theoretical and experimental evidence for the formation of 'open' sites also for Sn- and Zr-containing zeolites.[29]

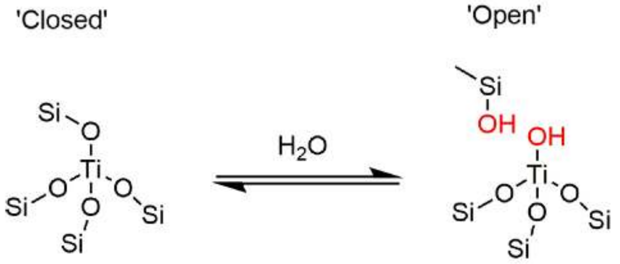

Scheme 3. Closed and opened Ti centres in zeolites.

'Open' sites were shown to be more active for the epoxidation of alkenes over Ti-MFI, Baeyer-Villiger (BV) oxidation of cyclic ketones over Sn-*BEA, and Meerwein–Ponndorf–Verley (MPV) reduction of cyclic ketones with aliphatic alcohols over both Sn- and Zr-*BEA.[30] Sushkevich et al. correlated the initial rates of ethanol condensation to butadiene with the number of 'open' sites in Zr-*BEA determined by FTIR spectroscopy of adsorbed CO.[29] DFT calculations suggest that stronger acidity and greater flexibility of the 'open' sites are responsible for their higher reactivity. [29]

However, in contrast to Brønsted acid sites, generalized quantification of the strength of Lewis acid centres is difficult as the affinity scale in this case strongly depends on the nature of the employed reference base molecule. This is related to the fact that the energy of Lewis acid-base interaction depends on the relative position of the highest occupied molecular orbital (HOMO) of the base and the lowest unoccupied molecular orbital (LUMO) of the acid, i.e. on the identity of the metal. For Sn it is the σ^*(SnO) orbitals, whereas for Ti (as well as for Zr and Hf) it is the d_{z^2} atomic orbitals of the heteroatom which are involved in the interaction. Several computational studies were performed to quantify the Lewis acidity of T^{4+}-substituted zeolites. Yang et al.[31] calculated descriptors for Lewis acidity such as LUMO energies, Fukui functions, absolute electronegativity, and absolute hardness using DFT to discriminate the strength of Lewis sites in T^{4+}-substituted MFI. It was found that none of these descriptors, which depend only on the zeolite itself, correlated with the Lewis acidity observed experimentally. Instead, the calculated adsorption energy of ammonia provided a more accurate prediction of the Lewis acid strength order for MFI zeolites: Ge < Ti < Pb ≤ Sn ≤ Zr. The same order of increasing Lewis acid strength was found by computationally evaluating adsorption energies of ammonia, pyridine, water, and trimethylphosphine oxide molecules for T^{4+}-substituted COE-4 zeolite.[32] The work of Gunther et al. is a rare if not the only example of experimental study of Lewis acid strength associated with isolated T^{4+} atoms in the zeolite framework.[33] The ^{15}N chemical shift of adsorbed pyridine in MAS NMR was found to correlate linearly with the Mulliken electronegativity of the metal centre in the order Ti < Hf < Zr < Nb < Ta < Sn.

Similarly to T^{3+} heteroelements, T^{4+} metal sites can be altered or removed from the zeolite framework under extreme activation or reaction conditions. Change of the local environment of Sn and Hf centres in T^{4+}-substituted *BEA during MPV reduction and etherification of hydroxymethylfurfural with ethanol was investigated in detail using ^{119}Sn MAS NMR and FTIR spectroscopies.[34] The results indicate hydrolysis of Sn–O–Si bonds and distortion of the tetrahedral angles consistent with weakening of the Lewis acid sites for the spent catalyst. Hf-*BEA showed a higher degree of site evolution when compared to Sn-*BEA at the same turnover number. Notably, while the changes in site distribution did not affect the zeolite activity for MPV reduction, the etherification activity decreased. The result suggests that the MPV reduction may occur on different or multiple sites, while etherification requires a specific type of site.

Thus, the nature of the heteroatom determines its local environment at framework positions, e.g. Td, distorted Td or near-tetrahedral C_{3v}. Moreover, isomorphously substituted T-atoms exhibit different stabilities depending on their nature and the specific zeolite structure, and the simple process of template removal may cause the migration of a fraction of heteroatoms from framework into extra-framework positions. Consequently, the local structure, reactivity, and nuclearity of heteroatoms may significantly deviate from that of the initially synthesized materials. Thus, the distribution of acid sites in zeolites can be heavily influenced by the synthetic method used. Differences can arise from varying the nature of acid sites, T-site location (inner vs. outer surface of crystals), and local surrounding (concentration of neighbour defect sites). The synthetic methods developed to tune these features of zeolite catalysts are described in the next Section 2.3.

2.3. Synthesis of Brønsted- and Lewis-acid zeolites

Recent advances in zeolite synthesis allowed to design a number of exciting materials especially prospective in catalytic transformation of bulky molecules. They include:

1) **extra-large pore zeolites** possessing micropores with diameter higher than 0.85 nm.[35] So far, around 20 different extra-large pore zeolites were synthesized with pore sizes up to about 2 nm. Most of these zeolites were prepared as germanosilicates.[36]

2) **zeolite nanocrystals** with dimensions smaller than 100 nm.[37] Decreasing the crystallite size aims at shortening the diffusion paths within the micropores. Most of the industrially used zeolites (including FAU, MFI, *BEA, MOR) can be prepared in a nanosized form.[38]

3) **two-dimensional zeolites** having one of three crystallographic dimensions about 1–3 nm thick. Direct methods are based on hydrothermal synthesis assisted by simple low-molecular or complex multifunctional SDAs[39] depending on the topology of the required zeolite. Seeding during the synthesis assisted by multi-ammonium surfactants results in zeolites with nanosponge-like morphology. An interesting post-synthesis approach towards two-dimensional zeolites is the controllable disassembly of 3D zeolites with anisotropic distribution of labile building units.[40]

4) **mesoporous zeolites** prepared via either hydrothermal synthesis using carbons[41], polymers[42], and inorganic solids [43] as hard templates or post-synthesis modifications of 3D or 2D zeolites.

The variation of the framework composition during *direct hydrothermal synthesis* is the most widely used approach to tune the chemistry of a particular zeolite (Section 2.3.1). Alternatively, the *post-synthesis* replacement of framework T-elements by heteroatoms (Section 2.3.2) is a suitable method to introduce heteroatoms into tetrahedral framework positions when direct synthesis of the material fails or is difficult to achieve.

2.3.1. Hydrothermal synthesis

Hydrothermal synthesis in aqueous media is a traditional way of zeolite preparation. The reaction mixture typically contains a source of framework-building elements, inorganic and/or organic cations and a solvent. Organic cations play a decisive role in the crystallization of zeolites by: i) contributing to the formation of certain typical inorganic oligomeric anions in the reaction mixture; ii) directing the condensation of such oligomers towards the formation of particular structural building units; iii) stabilizing the zeolite framework through host-guest interactions; and iv) compensating the framework charge influencing in this way the Si/T^{3+} framework ratio. Tetraalkylammonium (TAA) compounds are typically used as SDAs. The use of specially designed tetraalkylphosphonium cations, proton sponges, and amphiphilic organic molecules as SDAs resulting in new zeolitic materials including 2D zeolites was recently reviewed by Corma et al.[44]

Recent developments in analytical methods[45] enabling detailed studies of the mechanism of zeolite crystallization and the role of heteroelements in zeolite formation allowed understanding the structure-directing propensity of particular framework-building elements toward extra-large pore zeolites and controlling the zeolite crystal size to produce zeolite nanocrystals. Section 2.3.1.2 discusses a piece of knowledge accumulated to date on the effect of heteroelement nature in different stages of the crystallization process as an important step towards the rational design of zeolite catalysts.

2.3.1.2. Impact of the nature of heteroelement on crystallization of zeolites

The widely accepted mechanism of zeolite crystallization includes four main sequential steps: i) *prenucleation period* involving depolymerization of starting reagents and subsequent condensation into oligomeric anions, ii) *primary nucleation* involving the assembly of oligomeric (element)silicates and SDA$^+$ into clathrate-like primary units prior to nucleation, iii) *formation of nucleation centres* by aggregation of the silicate clusters formed on the previous step, and iv) *crystal growth*.

Recent studies evidence a remarkable influence of heteroelement nature and concentration not only on the rate of zeolite crystallization, but also on the structure and distribution of different oligomeric silicate species, and the metallate and mixed metallosilicate ions formed in prenucleating solutions (Scheme 4).[46, 47]

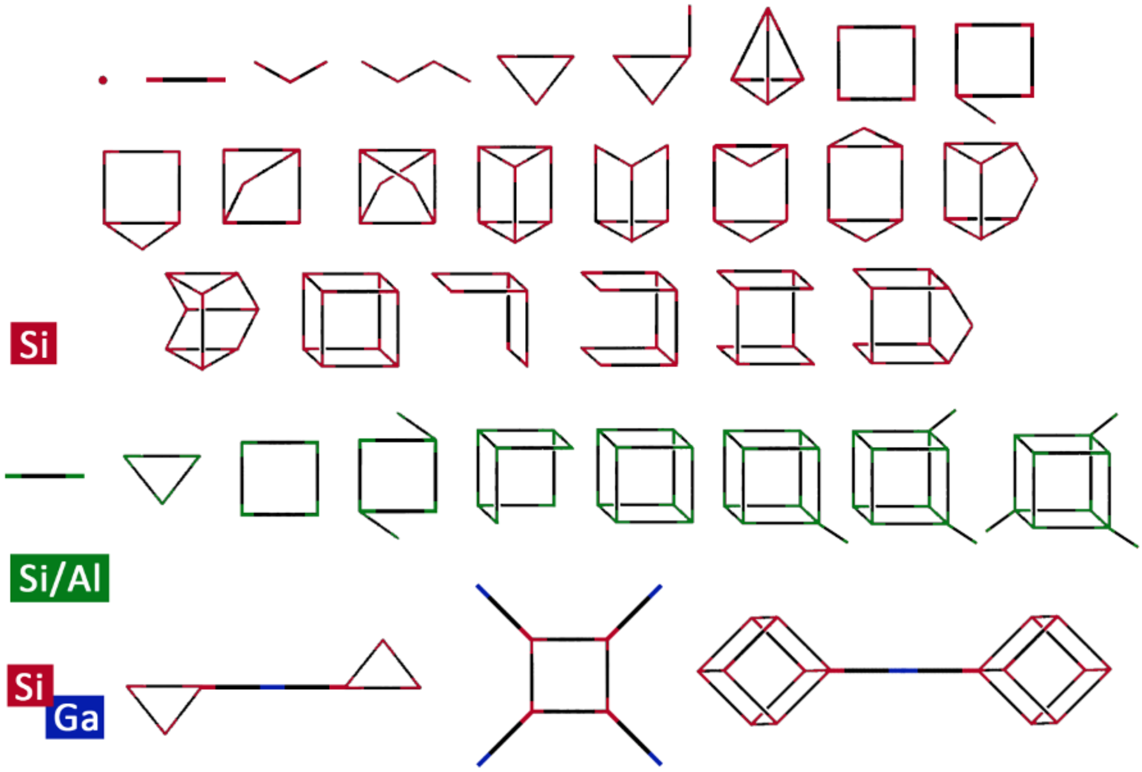

Scheme 4. (top) Silicate structures in basic aqueous solution identified by analysis of solution-state ^{29}Si NMR.[46] Each line in the stick figure represents a **Si–O–Si** siloxane linkage. (middle) Aluminosilicate species detected by high resolution MS in prenucleating solutions of Al-containing zeolites.[48] (bottom) Ga-containing species detected by MS/MS in prenucleating solutions containing gallium.[47]

Both NMR spectroscopy and electrospray ionization mass spectrometry (ESI-MS) results indicate isomorphous substitution of Si in silicate anions by Al at the early crystallization stage. Dimeric, linear, trimeric, and cyclic trimeric silicate anions containing ≥ 1 aluminium atoms were detected in TPA$^+$-containing aluminosilicate systems using liquid state ^{29}Si and ^{27}Al NMR, while double four ring (D4R) aluminosilicate anions were also found when using TMAOH as SDA.[46] The increase in the relative concentration of monomeric, dimeric and cyclic trimeric aluminosilicate anions at maintenance of mixed aluminosilicate D4R anions with the increase in Al concentration allowed to conclude a higher degree of aluminium incorporation into lower weight silicate oligomers. Oligomeric species detected in aluminosilicate TPAOH-containing systems by high resolution ESI-MS are shown in Scheme 4.[49] Random distribution of Al among different anions is consistent with previous NMR studies,[46, 50] while formation of Al–O–Al bonds during the prenucleation step is an unexpected finding, indicating a higher degree of freedom of the species in solution vs. zeolite frameworks. The formation of Al–O–Al linkages in the latter is forbidden due to disinclination for tetrahedral units of alumina to exist adjacent to one another (Lowenstein rule), though the possibility for violations of this rule in high and low silica zeolites was recently reported.[51]

Time-resolved ESI-MS allowed to identify the presence of dimerized homoanions of $Si_2O_7H_5^-$ and heteroanions of $SiGaO_7H_6^-$ in gallosilicate reaction systems in the presence of TPA^+ in 10 min after mixing the components. [47] Mixed gallosilicate anions of different structure were formed in the system after 2.5 h due to the attachment of gallate anions to cyclic and bicyclic silicate anions. Independently on the nature of SDA, two types of anions were found in the gallosilicate systems: 1) ones formed by attaching monomeric gallate ions to the vertices of silicate cyclic anions, or 2) silicate anions connected by a monomeric gallate bridge (Scheme 4). Thus, unlike aluminium, gallium does not isomorphously substitute silicon in the anions formed in the reaction mixture during the prenucleation period. In addition, lower degree of gallium incorporation into mixed metallosilicate ions is characteristic for gallosilicate vs. aluminosilicate systems.

The development of ESI-MS technique also allowed to explore germanium-containing prenucleating solutions, difficult to study by other techniques.[47] The obtained results demonstrated that, independently of the nature of the organic template (TMAOH, TEAOH, or TPAOH), the major species observed in the synthesized prenucleating solutions were single four rings (S4Rs) and D4Rs containing up to three Ge atoms. This observation agrees with: i) the preferential location of Ge in D4R units of zeolites,[52] ii) the faster crystallization of zeolites containing D4Rs in Ge-containing reaction mixtures,[53] and iii) the tendency of Ge for stabilization of such structures.[54]

A combination of ESI-MS with dynamic light scattering (DLS), XRD, energy-dispersive X-ray spectroscopy (EDX), and NMR methods was used to provide a comprehensive understanding of the nucleation of D4R-containing zeolites ITQ-21, *BEA, and LTA in germanosilicate mixtures, essential for the preparation of new extra-large pore zeolites.[48, 53] For these three systems, the following similar trends were observed: i) the increasing concentration of anionic oligomers (S4R, D4R, D4R pairs bridged by one silicate unit) containing up to 3 Ge atoms with increasing reaction time, and ii) the decrease in oligomers concentration at the time when the first solid (nanoparticles) is formed. This observation suggests that the synthesis conditions for specific zeolites favour the formation of species characteristic of these structures already during the prenucleation step and that the formed high molecular weight species are involved in the initial particle formation process.

Characterization of zeolite crystal growth with DLS and conventional X-ray diffraction allowed to address the influence of heteroelements on the kinetics of zeolite crystallization, which is important for designing nanocrystalline catalysts. The crystallization kinetics for Sn-containing MFI zeolite prepared by hydrothermal and dry-gel conversion route have been reported in ref.[55]. Both the apparent activation energies of nucleation (E_n) and crystallization (E_c) for the dry-gel conversion method (E_n = 50 kJ/mol and E_c = 53 kJ/mol) were found to be lower than those of the conventional hydrothermal route (E_n = 56 kJ/mol and E_c = 60 kJ/mol). The nucleation rate depends on the nature of the metal cationic species and their ability to condense with the silicate species. In this respect, the obtained E_n for Sn-MFI is much lower in comparison with the values previously found for T^{3+}-substituted MFI: Al-MFI (E_n = 118 kJ/mol) < Fe-MFI (145 kJ/mol) < Ga-MFI (155 kJ/mol).[56]

Thus, the nature of the heteroelement (ionic radius, characteristic coordination number) affects the crystallization of zeolites already from the very initial prenucleation step, determining the structure and distribution of oligomeric metallosilicate species and their further aggregation to zeolite nuclei of particular structure, i.e. phase selectivity of zeolite formation. Understanding the influence of heteroelement on the crystallization kinetics is crucial for the rational design of new zeolite structures and morphologies.

2.3.1.3. Tailoring the nature of acid sites

A number of conventional small-, medium- and large-pore zeolites possessing framework Al, B, Ga, Fe, Ti, and Sn atoms have been synthesized to date using bottom-up synthesis approaches. Features of hydrothermal synthesis as well as properties and catalytic application of such heteroelement-substituted zeolites were comprehensively reviewed elsewhere.[57] Herein we will discuss the most recent advances in the field focusing on the design of T^{3+}- and T^{4+}-substituted zeolites with enhanced accessibility of active sites (e.g. extra-large pore, nanolayered, nanosized and mesoporous zeolites).

New extra-large pore zeolites. The potential of extra-large-pore zeolites (with the channel openings consisting of more than 12 tetrahedra) to serve as catalysts in the transformation of bulky molecules made them highly desired synthesis targets. The use of rigid and bulky SDAs with the appropriate polarity/hydrophilicity allowed to synthesize the first high-silica extra-large-pore zeolites DON (UTD-1)[58] and CFI (CIT-5)[59]. The recent progress in this area is mainly connected with the use of the structure-directing propensity of some heteroatoms toward the formation of specific building units (e.g. 3R, D4R) stabilizing low-framework-density zeolites. The analysis of the structures of organic SDAs recently used for the preparation of extra-large pore zeolites (Table 1) reveals that bulkiness and rigidity of the SDA are not mandatory. In contrast, the presence of B, Ga, and Ge in the reaction mixture was shown and rationalized (Section 2.3.1.2) to be crucial for the crystallization of extra-large pore zeolites. Some of reported isostructural extra-large pore zeolites (e.g. IM-12 and ITQ-15; CIT-13, NUD-2 and SAZ-1) were prepared in the presence of different SDAs, but all in Ge-containing reaction mixtures. Recently, Corma[35] and Zones[60] reviewed the strategies toward creating materials with large channels and multi-dimensional pore systems by taking advantage of the structure-directing ability of Be, B, Ga, and Ge.

When considering the application of extra-large pore zeolites in catalysis, the thermally stable ITT (ITQ-33, 18×10×10-ring pore system), ITV (ITQ-37, 30×30×30-ring), UTL (ITQ-15 or IM-12, 14×12-ring) and IRR (ITQ-44, 18×12×12-ring) zeolites deserve a special note. While ITT (T^{4+}/Al = 55) has been originally synthesized in Al-containing germanosilicate gels with SDA6 (Table 1), the incorporation of Al into ITV zeolite (T^{4+}/Al = 80 – 160) required using the special achiral SDA 3′,4′-dihydro-1′H-spiro[isoindoline-2,2′-isoquinolin]-2-ium.[61] UTL zeolite was originally reported as pure germanosilicate crystallizing either in the presence of SDA4 (IM-12, Table 1) [62] or SDA5 (ITQ-15, Table 1). [63] However, the possibility to introduce aluminium into the UTL framework was shown for both IM-12 and ITQ-15. A systematic study of the influence of various synthesis parameters (e.g. gel composition, pH, duration of crystallization) on UTL crystallization in B-, Al-, Ga-, Fe-containing germanosilicate reaction medium allowed to optimize the conditions for incorporation of different T^{3+} elements into the UTL framework and to prepare a set of extra-large pore zeolites with tuneable concentration and strength of acid sites.[19, 64] While the concentration of Brønsted acid centres in Al-, Ga-, and Fe-UTL was shown to be adjusted by changing the pH of the initial gel, the concentration of Brønsted acid sites associated with framework boron atoms depended neither on pH nor on the concentration of B in the reaction medium. FTIR of adsorbed pyridine and NH_3-TPD measurements clearly showed that incorporation of B, Al, Ga, and Fe into the framework of UTL zeolite resulted in the formation of Brønsted acid sites with the acid strength increasing in the following order: B < Fe < Ga < Al.[19, 65]

Table 1. Extra-large pore zeolites which structures were solved in the last 15 years and respective SDAs used for syntheses.

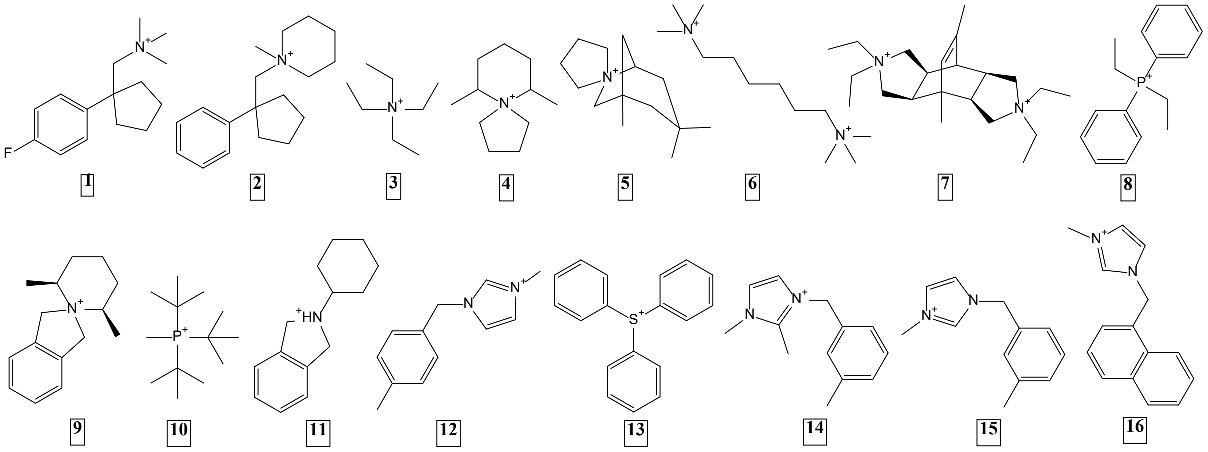

Code	Material	Channel system	Framework composition	SDA	Ref.
SFH	SSZ-53	1D 14R	$B_{1.6}Si_{62.4}O_{128}$	1	66
SFN	SSZ-59	1D 14R	$B_{0.35}Si_{15.65}O_{32}$	2	66
ETR	ECR-34	1D 18R	$Ga_{11.6}Al_{0.3}Si_{36.1}O_{96}$	3	67
UTL	IM-12,	2D 14×12R	$Ge_{13.8}Si_{62.2}O_{152}$	4	62
	ITQ-15	2D 14×12R	$Ge_{8}Si_{68}O_{152}$	5	63
ITT	ITQ-33	3D 18×10×10R	$Ge_{13.8}Al_{1.8}Si_{30.4}O_{92}$	6	68
-ITV	ITQ-37	3D 30×30×30R	$Ge_{80}Si_{112}O_{368}(OH)_{32}$	7	69
-IRY	ITQ-40	3D 16×16×15R	$Ge_{32.4}Si_{43.6}O_{150}(OH)_{4}$	8	70
–	ITQ-43	3D 28×12×12R	$Ge_{49.6}Si_{110.4}O_{320}$	9	71
IRR	ITQ-44	3D 18×12×12R	$Ge_{16.6}Al_{1.6}Si_{33.8}O_{104}$	9	95
-IFT	ITQ-53	3D 14×14×14R	$Ge_{71.6}Si_{80.4}O_{300}(OH)_{8}$	10	72
-IFU	ITQ-54	3D 20×14×12R	$Ge_{65.3}Si_{62.7}O_{252}(OH)_{8}$	11	52
–	NUD-1	3D 18×12×10R	$Ge_{47.81}Si_{50.19}O_{196}$	12	73
–	GeZA	3D 15×12×12R	$Ge_{22.2}Si_{41.8}O_{128}$	13	74
*CTH	CIT-13	2D 14×10R	$Ge_{9.66}Si_{54.34}O_{128}$	14	75
	NUD-2		$Ge_{4}Si_{28}O_{64}$	15	76
	SAZ-1			16	77

Al-, B- and Ga-substituted IRR zeolites were recently prepared using commercial benzyltriethylammonium bromide as SDA.[78] The amount of B and Ga atoms incorporated in IRR was lower than that of Al (T^{4+}/Al = 20). Computational modelling of the relative stabilities of isomorphously substituted IRR zeolites with DFT showed that the pure silicate and aluminosilicate forms are more stable than the germanosilicate ones. [79]

NUD-2 zeolite can be synthesized either in germanosilicate and aluminogermanosilicate reaction mixtures using SDA15 (Table 1). The incorporation of Al atoms in framework positions was confirmed using ^{27}Al NMR. However, acidic and catalytic properties of Al-NUD-1 were not studied to date.[73]

Among T^{4+} elements, only Ti was successfully incorporated by direct synthesis into the framework of extra-large pore zeolites, with Ti-containing DON zeolite being the first example.[80] Recently, two novel extra-large pore titanosilicate zeolites CFI and UTL have been prepared.[81, 82] The degree of isomorphous Si-to-Ti substitution in CIT-5 (Si/Ti = 23 – 106) [81] and UTL (Si/Ti = 139)[82] was found to be lower compared with commercial TS-1 zeolite.[57] Both Ti-CFI and Ti-UTL contained a substantial number of extra-framework Ti atoms, which can partially be removed by treating the as-synthesized materials with acidic solutions. [82]

Thus, several extra-large pore zeolites were found accepting T^{3+}/T^{4+} framework atoms during hydrothermal crystallization allowing the generation of catalytically active sites. On the other hand, the thermal and hydrothermal stability of a number of Ge-rich T^{3+}-substituted extra-large pore zeolites (e.g. ITQ-40 and ITQ-43) needs to be improved to enable their application in catalysis. In addition, the possibility of incorporating T^{3+} or T^{4+} heteroelements into thermally stable extra-large pore germanosilicate zeolites ITQ-53,[72] ITQ-54,[52] CIT-13, [75] and GeZa[74] is an issue that remains to be solved to make use of their beneficial textural properties.

Post-synthesis incorporation of T^{3+} and T^{4+} atoms into extra-large pore zeolites will be discussed in Section 2.3.2 as an alternative approach for tailoring catalytically active sites and improving the stability of novel zeolites.

Restricted crystal growth and design of zeolite nanocrystals. The reduction of particle size from the micrometer to the nanometer scale is another hot area in tailoring zeolite catalysts intensively developed during the past decade.

The effect of different parameters (including SDA nature[83], aging[84] and crystallization time, and temperature[85]) on the crystal size of MFI aluminosilicate zeolite were carefully addressed in the literature. This enabled the preparation of zeolite catalysts with enhanced accessibility of acid sites in diluted reaction mixtures (high H_2O/T ratios) containing an increased amount of SDA (high SDA/T ratios), at low temperatures, and under Na^+-deficient conditions to diminish the aggregation of zeolite nanoparticles.

Vieira et al. used different silica sources to vary the crystal size of Al- and Ga-substituted MFI zeolites during TPA^+-assisted hydrothermal crystallization.[86] While the use of colloidal silica resulted in the formation of large crystals (10 – 12 µm), silica alkoxide provoked the formation of small ones (1.5 µm). The effect of the crystal size and acid strength of the produced Ga- and Al-substituted MFI zeolites was studied in the gas-phase glycerol dehydration reaction.

Nanocrystalline Fe-MFI zeolites were prepared through an emulsion method in a water/polyoxyethylene-(15)-oleyl ether/cyclohexane medium using tetrapropylammonium hydroxide as SDA. [87] The morphology of the resulting Fe-MFI samples depended on the water-to-polyoxyethylene-(15)-oleyl ether (W/P) ratio. A W/P ratio of 4.5 resulted in the formation of nano-Fe-MFI agglomerates with 1000 nm size, while a W/P ratio of 11 lead to monodisperse nanocrystals sizing 100 nm.

Recently, Tolborg et al.[88] evaluated the kinetics of F-assisted crystallization of Sn-*BEA zeolites in relation to Sn content in the initial gel. Prolonged crystallization times were required at increasing tin contents in the reaction mixture. Thus, fully crystalline Sn-*BEA with low content of tin (Si/Sn = 400) was obtained after 4 days, while the synthesis of Sn-*BEA with moderate (Si/Sn = 200 – 150) and high (Si/Sn = 100) concentration of tin required 7 – 14 and 60 days, respectively. The increase in the crystal size was observed with prolongation of crystallization at defined Si/Sn ratio, with crystals of 4, 7 and 12 µm in size being formed after 7, 14 and 30 days of crystallization at Si/Sn = 100 – 400 (Figure 1 a-e). Noticeably, the heteroelement was not distributed evenly in the crystals, showing an outer shell enriched in tin atoms independently on Si/Sn ratio, duration of the synthesis, and nature of tin precursor (Figure 1 g-i). The beneficial behaviour of Sn-*BEA with smaller crystal size was demonstrated in the conversion of 1,3-dihydroxyacetone to methyl lactate catalyzed by Lewis acid sites. The yield of the targeted lactate increased from 18 to 27% with decreasing the size of Sn-*BEA from 12 to 7 µm.

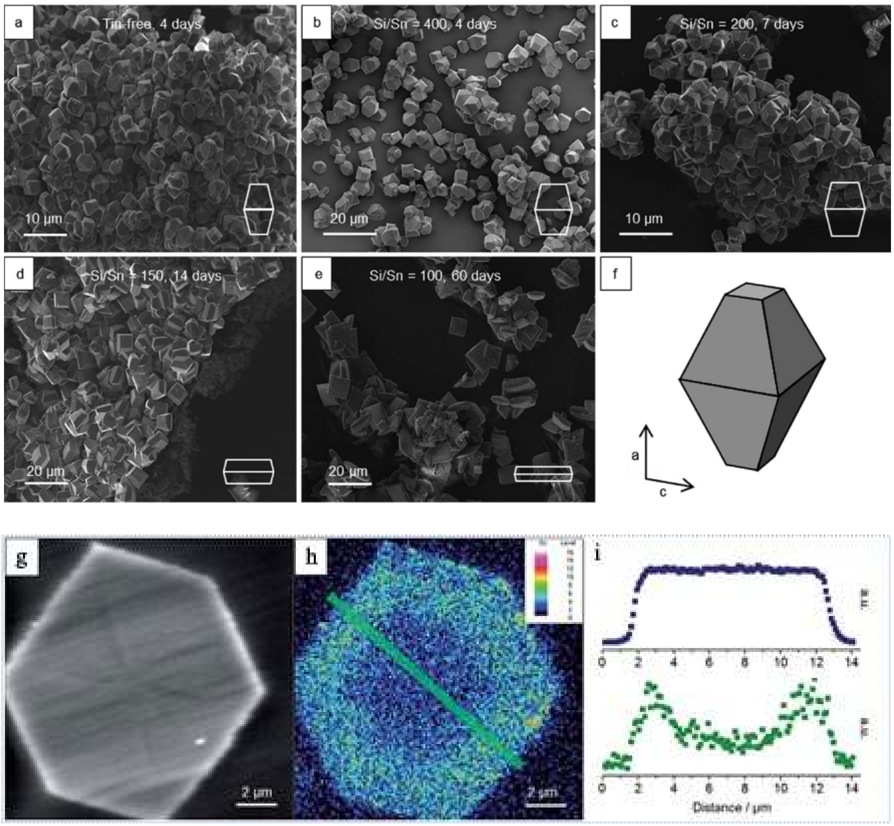

Figure 1. (a-f) SEM images of Sn-*BEA zeolites, showing increasing crystal size with decreasing Si/Sn in initial gel: Si/Sn = ∞ (a), Si/Sn = 400 (b), Si/Sn = 200 (c); Si/Sn = 150 (d), Si/Sn = 100 (e). On (f) the capped bipyramidal morphology of Sn-BEA is shown with the *a* and *c* direction presented. (g-i) Wavelength-dispersive spectrometry (WDS) analysis of Sn-BEA sample (Si/Sn = 200) showing enrichment of outer crystal shell with Sn and even Si distribution: SE image of the investigated crystal (g), Sn X-ray intensity (h), X-ray intensities for Si (🟦) and Sn (🟩) (i). The data for (i) were extracted from the map at the area indicated by the green outline on (h) and averaged across the thickness of the line. Adapted from ref. [88]

In recent years, the efforts in the area of nanosized zeolitic materials were directed at minimization or avoidance in the use of costly organic SDAs. The study of crystal growth kinetics allowed to develop the SDA-free synthesis of EMT zeolite nanocrystals. [89] Ultra-small aluminosilicate EMT nanocrystals (7 − 15 nm) were prepared at room temperature when slowing down the crystal growth and phase transformation into more stable FAU and SOD frameworks. Narrow particle size distribution of the produced EMT, the unnecessity to use costly 18-crown-6 ether, and the possibility to avoid post-synthesis calcination for elimination of the template make this synthesis exceptional.[89] Recently, aluminosilicate NaY zeolite nanocrystals were hydrothermally synthesized via a three-stage temperature control strategy, without adding any organic additives. [90]

Seed-assisted crystallization of zeolite nanocrystals in an organic-free gel was successfully applied for MFI,[91, 92] *BEA,[93] and SAPO-34.[94] The crystallization temperature and the size of seeds crystals added to the synthesis mixture were important parameters influencing the crystal size of the zeolite product.[91, 94] While nonuniform micron-sized cubic crystals and irregular poly-crystals of SAPO-34 were formed when using micron-sized seeds, nanosized SAPO-34 seeds facilitated the formation of uniform nanosized SAPO-34 crystals (Figure 2). [94] On the other hand, while MFI crystals with size ranging 30 – 70 nm were obtained from 3 wt% seeded gels at 100 and 120 °C, the crystallite size increased to 130 – 160 nm at 150 °C and above 200 nm at 170 °C (Figure 2). [91]

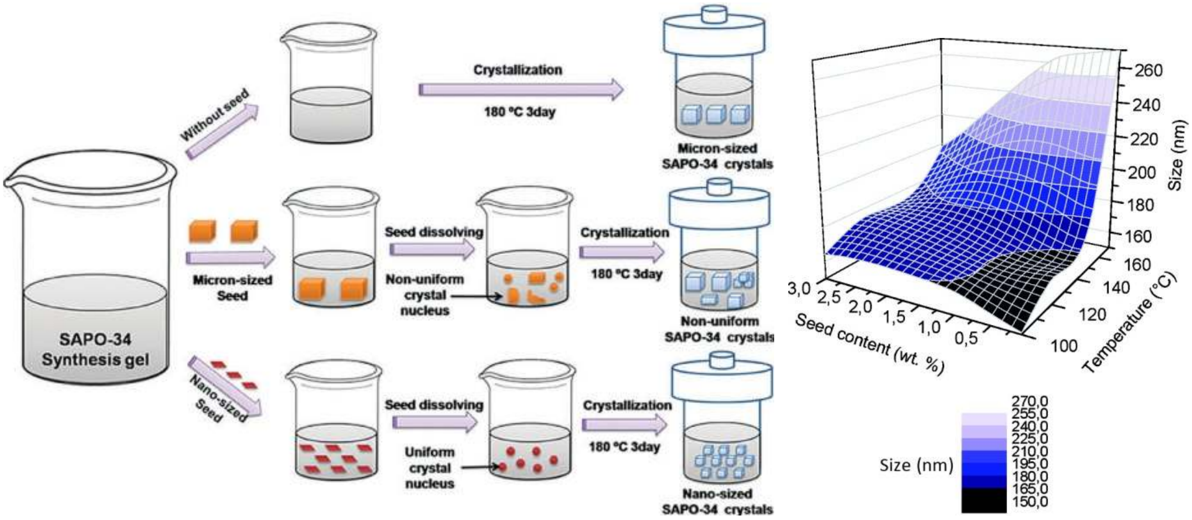

Figure 2. Schematic representation of the influence of seeding on the crystal size of zeolites (left). [94] The mean particle size (number weighted) of Na-MFI zeolite vs. the synthesis temperature and seed content (right). [91]

Limitation of the Ostwald ripening growth mechanism by making use of porous carbons,[95] surfactant organosilanes,[96] and polymers[97] was also applied to control the size of zeolite crystals. Three-Dimensionally ordered Mesoporous (3Dom) carbons with different pore size (10 to 40 nm) as well as carbon replicas of mesoporous silicas (i.e. CMK-1,2,3) have been used as exo-templates for zeolite synthesis. The challenge for the production of zeolite nanocrystals by hard-templating approach was to hinder crystallization out of carbon pores (yielding mesoporous zeolites with intracrystalline mesoporosity discussed vide infra) while allowing zeolite growth inside the solid matrix. For that, steam-assisted crystallization (SAC) of reaction mixtures impregnated into 3Dom carbons[98] and hydrothermal treatment of 3Dom carbons preliminary seeded with zeolite were successfully applied[99]. After zeolite crystallization within the pores of the carbon template, the latter is removed by combustion leaving intercrystalline mesopores. The composition and concentration of zeolite precursor gel, as well as the textural properties (interconnectivity and pore size) of the carbon matrix are the critical variables determining the final characteristics of the zeolite nanoparticles.[100] Using the hard-templating method, size-tuneable nanocrystals of aluminosilicate MFI, *BEA, LTA, FAU, and LTL zeolites [99] and Sn-*BEA (Si/Sn = 125) zeolite with 1 µm-size crystals composed of aggregated primary 30 nm-size particles[101] have been synthesized.

Very recently Wang et al. reported the F127 triblock copolymer-assisted synthesis of mechanically robust mesoporous TS-1 microspheres of 3 to 50 µm in size via a temperature programmed self-assembling route.[97] The role of the triblock copolymer in the formation of mesoporous TS-1 microspheres consisted both in inhibiting the polymerization of SiO_2/nucleation of TS-1 and in promoting the aggregation of TS-1 nanoparticles. As a result, TS-1 nanoparticles of 50 – 100 nm were self-assembled into microspheres containing regular intercrystalline mesopores of diameter in the range of 6 – 10 nm in addition to the original micropores.

Besides nanocrystalline zeolites, the design of T^{3+} and T^{4+}-containing layered zeolites (1 – 3 nm thick nanosheets with zeolite topology) is another development of significance for tailoring zeolite-based catalysts.

Layered zeolites: development of external active sites. The first and the most studied layered MCM-22P zeolite precursor was synthesized accidentally from Al-poor aluminosilicate gel by conventional hexamethyleneimine-assisted hydrothermal synthesis.[102] Variation in composition of the reaction mixture and synthesis conditions in the presence of conventional SDAs was the main approach for the preparation of layered zeolites untill 2009. This method allowed to produce nanolayered forms of more than 10 different zeolite topologies[103] despite the lack of predictability of the outcome in such a trial-and-error synthesis route.

An innovative approach for controlled crystallization of layered zeolites was proposed by Ryoo et al.[39] It consists in using specially designed amphiphilic SDAs composed of a polyquaternary ammonium part and a long hydrophobic tail. SDAs of such type act as both zeolite structure-directing agents and mesopore-generating templates. The use of single-tail SDA like $C_{22}H_{45}-N^+(CH_3)_2-C_6H_{12}-N^+(CH_3)_2-C_6H_{12}$ ($C_{22\text{-}6\text{-}6}$) leads to the formation of MFI 2.5 nm-thick nanosheets of irregular arrangement [104] with a sharp mesopore diameter distribution centered at ~6 nm. The chemical composition of the formed aluminosilicate MFI nanosheets was found easily tuneable in a wide range (Si/Al = 40 – ∞)[105] making them suitable for a number of catalytic reactions. Systematic studies on the influence of synthesis variables on the nanosheet thickness have been performed. The possibility to tailor the thickness of the MFI nanolayers from 2.5 up to 7.5 nm by changing the number of ammonium groups in the surfactants was shown in ref. [106] The thickness of nanosheets was also controlled in the 2.5 – 20 nm range by properly balancing the structure-directing effects of $C_{18\text{-}6\text{-}6}$ SDA in the presence of Na^+ ions promoting the thickening of MFI nanosheets.[107]

In contrast to single-tail multi-ammonium surfactants, gemini-type SDAs [$C_nH_{2n+1}-(N^+(R)_2-C_6H_{12})_m-N^+(CH_3)_2-C_nH_{2n+1}$ (n = 16 – 22; m = 2, 3)] were shown to generate thin zeolite layers with regular ordering.[108] The use of such kind of surfactants allows the fine tuning of both wall thickness and mesoporous structure at the nanometer-length scale by the molecular design of amphiphilic SDAs. In contrast to MFI, irregular 3D networks of nanocrystals (called nanosponges) of aluminosilicate *BEA, MTW, and MRE zeolites were formed via a surfactant-tailored synthesis route. MFI zeolite with nanosponge morphology composed of self-arranged zeolite nanosheets was recently produced by adding the bulk 3D MFI as seeds during the surfactant-assisted hydrothermal synthesis in aluminosilicate reaction mixture.[109]

First layered titanosilicate[110] and stannosilicate[111] zeolites possessed MFI topology and were synthesized using $C_{16\text{-}6\text{-}6}$ SDA. Layered Ti-MFI was composed by crystalline layers of single-unit cell (~2 nm) thickness and contained quite high amount of tetrahedrally coordinated Ti atoms (Si/Ti = 57). Wang et al. succeeded in preparing multilamellar Ti-MFI (by using $C_{22\text{-}6\text{-}6}$ SDA), which behaved as efficient and reusable catalysts for the epoxidation of cyclic alkenes with *tert*-butyl hydroperoxide (TBHP).[112]

In surfactant-assisted preparation of nanosheet Sn-MFI, a strong influence of the tin content as well as of the nature of metal precursor on the properties of the final material was found. In particular, the use of $Sn(OBu)_4$ manifestly resulted in the formation of SnO_x clusters even for Sn-poor reaction mixtures (Si/Sn = 250). In contrast, $SnCl_4$ facilitated the incorporation of Sn into framework positions, although increasing Sn concentration in the gel usually deteriorated the crystallinity of the formed product.

Aluminosilicate and titanosilicate layered zeolites were shown to be efficient catalysts, especially for conversion of bulky molecules, after post-synthesis delamination or interlayer expansion applied to prevent aggregation/condensation of crystalline layers upon SDA removal.[113] Delamination is a multistep treatment that involves: i) contacting the layered zeolite precursor with a cationic surfactant (usually $CTMA^+$) in alkaline environment to expand the interlayer distance, ii) sonicating the swollen zeolite to disjoin crystalline layers, and iii) removing the surfactant, resulting in a collection of disordered zeolite layers/groups of stacked layers possesing intercrystalline mesoporosity. Successful delamination has been reported for Al-MCM-22P,[114] Al- and Ti-FER[115] and NSI[116] layered precursors. Pillaring is another famed approach applied for permanent expansion of interlayer space in 2D zeolites. Generally, pillaring involves: i) swelling of the layered zeolite with $CTMA^+$ cations which are used as either hydroxide or chloride in the mixture with tetrapropylammonium hydroxide, ii) treatment of the swollen material with an excess of TEOS, followed by iii) hydrolysis in water, and iv) calcination, allowing to produce layered zeolites with permanently expanded interlayer space serving as interlamellar mesoporosity. Pillaring of the microporous layered precursor MCM-22(P) resulted in preparation of micro-mesoporous MCM-36 zeolite,[117] while multilamellar layered MFI precursor has been recently successfully pillared without any swelling step.[104]

Recently, the use of small tetrapropylphosphonium SDA was reported resulting in the formation of so-called self-pillared single unit-cell of all-silica MFI, Al-MFI,[118] or Sn-MFI[119] nanosheets being repetitively branched nanolayer rotational MFI/MEL intergrowths (Figure 3). Minor MEL zeolite phase formed connectivities at the MFI layers intersections.

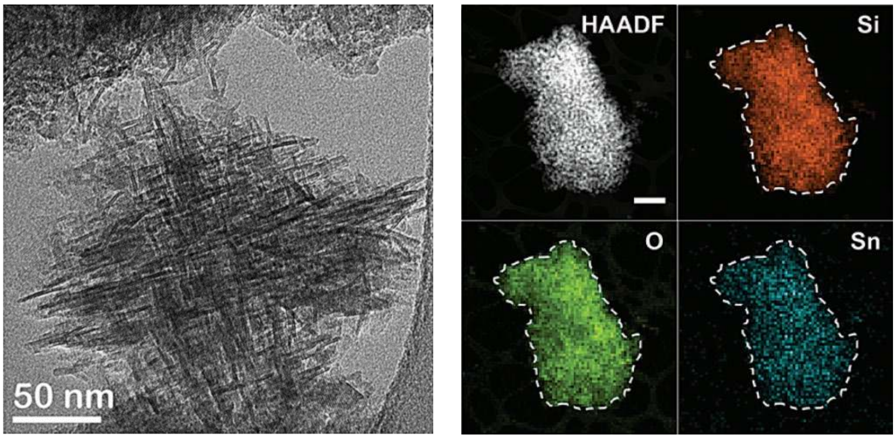

Figure 3. TEM image and EDX-STEM elemental map of self-pillared Sn-MFI (Si/Sn = 186) zeolite. [119]

Nanosponge Ti- and Sn-substituted *BEA zeolites have been prepared using a piperidinium-functionalized multi-ammonium surfactant as the SDA at near-neutral pH by Jo et al.[120]

Synthesis of micro-mesoporous zeolites. Zeolites with intracrystalline mesoporosity is another group of catalytically active materials developing in the last decade. Direct hydrothermal synthesis of such materials involves crystallization of zeolites around various hard templates (e.g. carbon particles, fibers, nanotubes, silylated polymers). Such hard templates trapped inside the zeolite crystals during the hydrothermal treatment are subsequently removed by combustion releasing intraparticle pores. Carbon black particles have been used for the preparation of mesoporous aluminosilicate MFI,[121] MWT[122], *BEA[123] and titanosilicate MEL[124] zeolites with broad pore size distribution, while silica MFI zeolite with uniform cylindrical mesopores were synthesized when using carbon nanotubes or nanofibers.[125] However, the interconnectivity of the generated mesopores with the micropores using this approach is generally poor.

Organosilane-based methods take advantage of the high affinity of organosilanes for grafting on silicate and aluminosilicate species[96, 126, 127] suppressing in this way the uniform growth of the microporous framework. Subsequent calcination leads to a hierarchical zeolite, in which the secondary porosity is directly related to the space occupied by the organosilane species. Moreover, varying the length of the alkyl chain in the organosilane surfactant, $[(RO)_3SiC_3H_6\text{-}N^+(CH_3)_2C_nH_{2n+1}]Cl$ ($n = 16 - 22$), enables the control over the mesopore diameter, as demonstrated for aluminosilicate MFI, LTA, MOR, CHA and FAU zeolites. [96, 126]

Adding silylated polymers to the reaction gel for the synthesis of MFI zeolite was shown to result in the formation of intracrystalline mesopores with a size increasing from 2 to 3 nm with increasing the molecular weight of template.[128] In this synthesis, the role of the silylated polymer consisted in grafting onto the surface of protozeolitic units subsequently aggregating into zeolite crystals. After combustion, intracrystalline mesopores substituted the space occupied by the grafted polymer.

In addition to hydrothermal hard-templated synthesis, the preparation of micro-mesoporous zeolites can be achieved using different post-synthesis modifications (Section 2.3.2).

In summary, a variety of novel zeolites of different chemical compositions and improved accessibility of active sites has been recently prepared using hydrothermal synthesis. While realizing and exploiting the structure-directing propensity of some heteroelements accelerated the discovery of new extra-large pore zeolites, understanding and careful tuning the kinetics of zeolite nucleation and crystal growth increased the number of zeolites prepared as nanocrystals. Furthermore, the innovative application of amphiphilic SDAs gave rise to nanolayered zeolite catalysts. However, despite its obvious benefits, hydrothermal synthesis quite often imposes restrictions on the maximal degree of isomorphous substitution in certain zeolite frameworks. This limit, in particular, can be governed either by the restricted number of charge-compensating organic SDA^+ cations fitting zeolite voids or by a rapid crystallization of admixture phases from gels with non-optimal chemical composition. Alternative to direct hydrothermal crystallization, post-synthesis isomorphous substitution is a facile approach usually allowing to enlarge the limits of heteroelement incorporation.

2.3.2. Post-synthesis isomorphous substitution

Traditionally, post-synthesis incorporation of heteroelements can be achieved by the treatment of a pre-formed zeolite with a volatile source of heteroelement at elevated temperature (gas phase isomorphous substitution) or with neutral, acidic or alkaline solutions of the heteroelement source at moderate temperature (hydrothermal isomorphous substitution). Moreover, solid-state reaction can be applied for tailoring the chemical composition of zeolites.

Removal of some framework atoms (demetallation, e.g. dealumination, desilication, deboronation, degermanation) leading to the formation of “silanol nests” usually precedes the insertion of heteroelements (Figure 4).

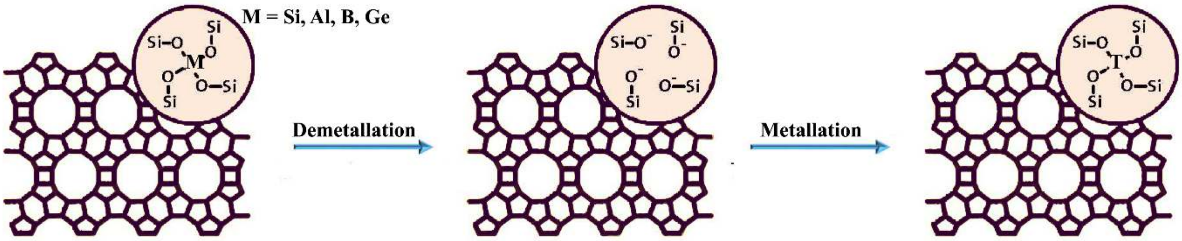

Figure 4. Schematic representation of two-step post-synthesis incorporation of heteroelements into zeolites. The scheme shows the formation of silanol nests upon demetallation treatment and their healing upon incorporation of heteroelement into the zeolite framework.

Dealumination, routinely performed by steaming or treatment of zeolites with mineral acids or the combination of both methods, is one of the pioneer demetallation treatments leading to hierarchical materials. The textural properties can be tailored depending on the nature of a particular zeolite (e.g. FAU, *BEA, MOR) and the type of dealumination process, particularly on the strength and concentration of applied acid. Since the mesopores are generated by the extraction of framework Al, which originally present acid sites, the dealumination causes a decrease in the number of acid sites.[129]

In contrast, desilication in alkaline medium successfully applied to a large variety of zeolites (MOR, *BEA, FER, MFI, etc.) does not cause so significant changes in Si/Al ratio and, therefore, in acidity. Mesoporous textures generated by desilication strongly depend on the concentration and distribution of Al within the zeolite crystals. Silica-rich domains are easily leached out to generate large mesopores while Al-rich domains remain relatively unchanged. Thus, the highest mesopore surface areas were reached after desilication of zeolites with Si/Al ratios within 25 – 50. The desilication procedure clearly allows developing mesoporosity in zeolites but quite often at the expense of losing considerable amounts of microporosity. Different variations of the method have been introduced to overpass this drawback, such as the substitution of sodium hydroxide for tetraalkylammonium hydroxide solutions or the application of partial detemplation prior desilication.[130]

In contrast to dealumination and desilication, leaching of boron or germanium off the zeolite framework requires mild conditions for demetallation, which in turn enables avoiding side reactions such as T-sites (silicon) migration which has been recently proved to occur during the dealumination treatment.[131] Degermanation in mild acidic medium was shown to be an efficient method for tuning the textural characteristics of micro-mesoporous zeolites ITH and IWW by varying pH, temperature and duration of the treatment.[132]

The post-synthetic demetallation can be considered as the most economic route to generate mesopores in addition to the intrinsic micropores in zeolites. However, it may suffer from a lack of control over the size of the formed mesopores and their spatial arrangement/distribution.

Dealumination-metallation

A number of T^{4+}-substituted zeolites (T = Sn, Zr, Ti), broadly applied as efficient heterogeneous catalysts in many fine chemical and biomass-treatment processes[133] were recently prepared using a dealumination-metallation approach. This allowed to achieve a higher metal content in the framework while avoiding long-lasting hydrothermal synthesis of T^{4+}-substituted zeolites usually performed using hazardous HF as mineralizing agent. In addition, post-synthesis isomorphous substitution allows the preparation of smaller crystals of T^{4+}-zeolites, which is impossible to achieve during F^--assisted hydrothermal crystallization, especially at high metal loading.[88]

Al-free nanocrystalline Sn-*BEA (Si/Al > 1770) with up to 6.2 wt% of Sn was prepared using a two-step treatment involving the dealumination of Al-*BEA (Si/Al = 11) with 6M HNO_3 followed by gas-phase metallation with $SnCl_4$.[134] The optimal temperature of the latter step was found to be 500 °C, while Sn incorporation became less efficient and was accompanied with the formation of extra-framework SnO_x species at higher or lower temperatures. The fraction of extra-framework Sn species increased remarkably when the Sn loading exceeded 5 wt%. Similar dealumination-metallation approach was used for incorporation of Sn atoms into the framework of a mesostructured *BEA nanocrystalline zeolite, hydrothermally synthesized in the presence of ammonium-modified chitosan.[135]

Besides gas-phase metallation, liquid-phase reaction was exploited for post-synthesis incorporation of T^{4+} elements into zeolites. Dijkmans et al.[136] performed a comprehensive comparative study of post-synthesized and hydrothermally synthesized Sn-*BEA to explain their catalytic behaviour in different Lewis-acid catalyzed reactions. The concentration and nature of Sn-associated acid sites formed upon post-synthesis modification of zeolite *BEA was shown heavily dependent on the synthesis approach (dealumination followed by either gas-phase isomorphous substitution or grafting) and on the nature (Bu_4Sn, Bu_2SnCl_2, $SnCl_2 \cdot 2H_2O$, $SnCl_4 \cdot 5H_2O$, anhydrous $SnCl_4$) and amount of Sn source. The amount of extra-framework Sn species naturally increased with Sn loading independently on the method of post-synthesis modification, while increasing the number of chloride ligands in the heteroelement precursor resulted in more efficient framework incorporation. For dealuminated *BEA impregnated with $SnCl_4$ in anhydrous isopropanol, formation of isolated Sn sites was shown to occur at Sn loadings below 2 wt%, while oligomeric extra-framework Sn species were observed at higher Sn contents. [136] Characterization of post-synthesized and directly synthesized Sn-*BEA using advanced spectroscopic techniques revealed differences in the local $Sn(OSi)_4$ site geometry resulting in a higher strength of the Lewis acid sites in Sn-*BEA made by dealumination/isopropanol-assisted grafting vs. hydrothermal synthesis.[137]

Incorporation of Sn into *BEA framework can be performed via impregnation of dealuminated zeolite with anhydrous $SnCl_4$ in inert atmosphere. [138] The excess of Sn was removed by washing the impregnated sample with methanol to prevent the formation of extra-framework SnO_x species. Besides the synthesis of Sn-substituted large-pore *BEA zeolite, the use of dealumination-metallation approach allowed the isomorphous incorporation of Sn into zeolite FAU.[139]

Wang et al. showed the preparation of Zr-substituted *BEA zeolite (Si/Zr = 12.5 – 150) via wet impregnation of dealuminated *BEA with $Zr(NO_3)_4$ or $ZrOCl_2$, allowing 7-fold shortening synthesis time and avoiding the use of HF required in the conventional synthesis.[140] However, a substantial part of Zr was found as extra-framework ZrO_x species. Zr atoms have been incorporated into *BEA framework by treatment of dealuminated zeolites with $ZrOCl_2$ in dimethyl sulfoxide under reflux.[141] A decrease in Si/Al ratio from 75 to 19 in the initial *BEA zeolite was shown to increase the Si/Zr ratio from 59 to 157 in Zr-*BEA materials. Preferential grafting of Zr to the terminal silanol groups present on the external surface of zeolite crystals rather than incorporation of Zr into silanol nests was confirmed using FTIR and advanced NMR spectroscopy.

Ti atoms were successfully incorporated into MOR zeolite with crystal size ranging from 110 to 5160 nm using dealumination followed by gas-phase metallation with $TiCl_4$.[142] The efficiency of dealumination (under similar conditions the Si/Al ratio reached 429 and 156 for 110 and 5160 nm-sized MOR crystals, respectively) as well as Ti incorporation (Si/Ti = 73 and 116 for 110 and 5160 nm-sized MOR crystals, respectively) were found to decrease with enlargement of MOR crystals, which was naturally attributed to diffusion limitations.

Alternatively to the gas-phase and liquid-phase metallation usually resulting in the appearance of some fraction of T^{4+} atoms as extra-framework species, the use of solid-state exchange involving mechanical grinding of dealuminated *BEA zeolite and Sn (II) acetate[143] or Zr (IV) ethoxide[144] followed by calcination resulted in high metal loading (8 and 10 wt% for Zr and Sn, respectively) without the formation of bulk $T^{4+}O_2$ species.

Besides being a facile way for post-synthesis fabrication of Lewis acid catalysts, dealumination-metallation was also an efficient approach for the preparation of bifunctional catalysts containing both Brønsted and Lewis acid sites. [145-149] Tailoring zeolites with multifunctional active sites allows replacement of multistep processes usually involving intermediate product separation and purification steps by one-pot processes, as discussed in Section 2.4.3.

Desilication-metallation

Alternative to dealumination-isomorphous substitution, ‘alkaline-assisted metallation’ was recently proposed by Perez-Ramirez et al. for the synthesis of zeolite catalysts comprising isolated Lewis acid sites.[150, 151] The treatment of high-silica MFI (Si/Al = 961)[20] or *BEA (Si/Al = 220)[150] with basic solutions of NaOH or TPAOH in the presence of a tin source (($Sn(SO_4)_2$, $SnSO_4$ or $SnCl_4{\cdot}5H_2O$)) was efficient for producing active catalysts for valorization of renewables. The versatility of the method, being applicable for both Al-rich and Al-poor zeolites under milder conditions, as well as the development of mesopores upon the treatment in alkaline medium are clear advantages of desilication vs. dealumination followed by isomorphous substitution. On the other hand, post-synthetic alkaline-assisted stannation usually resulted in less homogeneous distribution of Sn species compared with direct synthesis or dealumination/stannation approaches.[151] Indeed, the higher number of silanol nests developed upon desilication was shown to favour the formation of large Sn domains upon condensation with the heteroelement precursor.

Sequential desilication/dealumination treatment followed by solid-state metallation using Sn(II) acetate was successfully applied for preparing micro-mesoporous Sn-*BEA zeolite (Figure 5) containing exclusively tetrahedrally coordinated framework Sn atoms (2 wt% Sn loading). [152]

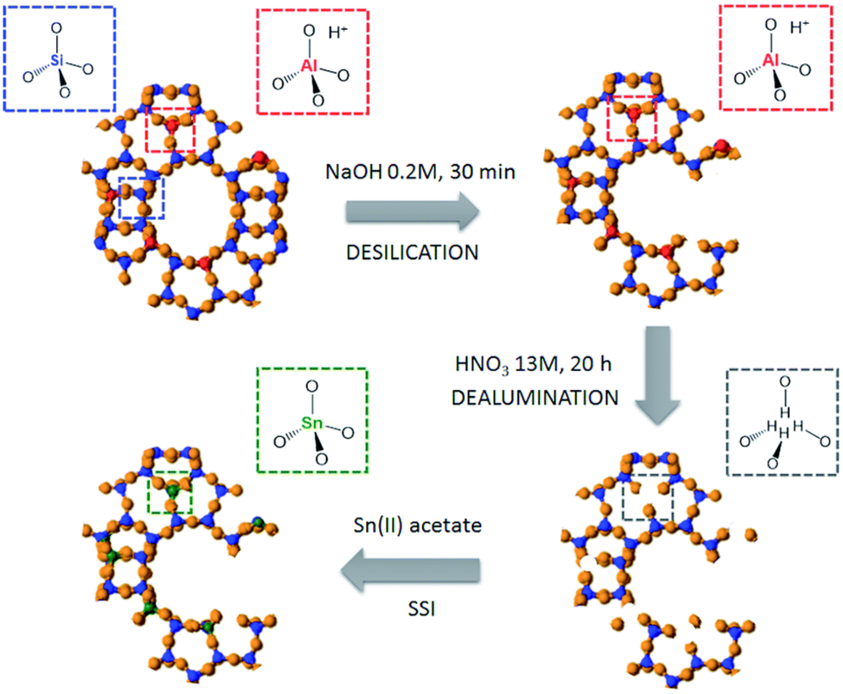

Figure 5. Three-step post-synthesis approach used in ref. [152] for the preparation of mesoporous Sn-substituted *BEA zeolite.

Recently, Tang et al. reported the post-synthesis preparation of hierarchical Zr-, Sn- and Ti-substituted *BEA zeolite starting from the commercially available *BEA aluminosilicate (Si/Al = 16.7) via acid–alkaline treatments and subsequent dry impregnation of $Cp_2T^{4+}Cl_2$.[153]

Deboronation-metallation

Deboronation-alumination was widely applied for incorporation of strong acid centres into borosilicate zeolites. A linear increase of Al-for-B substitution with increasing pH in the range 0.5 – 2.5 as well as mostly tetrahedral coordination of reinserted Al atoms was found for a number of large-pore borosilicate zeolites (e.g. AFI, CON, SFS, *SFV) when treated with $Al(NO_3)_3$ solutions.[154] However, being successful for large- and extra-large pore zeolites, Al incorporation by treatment with $Al(NO_3)_3$ appeared to be not applicable to medium pore boralites (e.g. MEL), which was rationalized by difficulties in the penetration of bulky hydrated aluminium cations into 10-ring pores. This finding was later used for the so-called “pore selective aluminium reinsertion”. As an example, selective substitution of boron for aluminium was achieved in the 12-ring pores of *SFV boralites with a porous system containing domains of intersecting medium 10-ring channels and a minor fraction of large 12-ring pores.[155] The catalytic behaviour of post-synthetically aluminated Al-SFV, containing strong acid sites predominantly in the 12-ring channels, was compared to that of directly synthesized Al-SFV with random distribution of aluminium atoms in the acid-catalyzed isomerization and disproportionation of 1,3-diethylbenzene.[155] The latter zeolite showed higher ratios of 1,4- to 1,2-diethylbenzene (20.9 vs. 12.7) and diethylbenzenes to triethylbenzenes (107.4 vs. 20.8). The results evidenced the higher contribution of monomolecular isomerization vs. bimolecular disproportionation reaction in Al-SFV due to the presence of active sites in the medium-pore channels enhancing the formation of less bulky products (i.e., 1,4- vs. 1,2-diethylbenzene, and diethylbenzenes vs. triethylbenzenes).

Another example of the “pore selective aluminium reinsertion” is given by borosilicate zeolites IFW (3D 10×8×8-ring channel system),[156] SFS (2D 12×10-ring channel system), and SSZ-82 (2D 12×10-ring channel system).[154] The caged structure of the medium-pore IFW zeolite with cages delimited by a 14-ring in the middle and interconnected by 10-ring pores makes this zeolite susceptible for Al reinsertion in contrast to other high-silica zeolites with 10-ring channel systems. [156]

Post-synthesis replacement of boron by aluminium was also carried out in two steps involving extraction of boron followed by insertion of Al.[157] Tong and Koller showed that trigonal boron can be selectively extracted from zeolite frameworks while leaving tetrahedral boron in the structure by treatment with water.[158] However, the high selectivity that could be achieved in the deboronation procedure was not translated in the subsequent Al incorporation reaction when using Al^{3+} aqueous solutions, i.e. the amount of Al reinserted into zeolite *BEA varied by only 10% irrespective of the ratio between tetrahedral and trigonal boron in the starting zeolite. The result was explained by additional deboronation taking place in the highly acidic aqueous solution of the Al^{3+} salt. On the other hand, using ethanolic instead of aqueous Al^{3+} increased the selectivity of Al reinsertion, allowing to control the amount of incorporated Al by changing the Na^+/NH_4^+ ratio in the initial borosilicate *BEA. Besides Al, other heteroatoms were successfully incorporated into the framework of deboronated zeolites, e.g. Ti,[159] and Sn.[160]

Degermanation-metallation

In the last decade, post-synthesis isomorphous substitution in germanosilicate zeolites attracted a lot of attention as an obvious tool to decrease the cost of germanosilicates and to enhance their hydrolytic stability.

The post-synthesis replacement of framework cations, commonly applied to calcined SDA-free zeolites, is frequently not acceptable for germanosilicate zeolites due to their inability to withstand high temperature treatments. Thus, the post-synthesis stabilization of SDA-containing germanosilicate zeolites by isomorphous substitution of Ge with Si,[161, 162] Al,[163, 164] Ti[165] or even Zr[166] was attempted. In a pioneering work, Valtchev et al. reported the incorporation of aluminium into the framework of as-synthesized BEC (Si/Ge = 3.6) zeolite with the simultaneous removal of Ge (Si/Ge ratio increased from 3 to 7) and SDA under low acidic conditions.[163] The aluminated BEC (Si/Al = 20) was maintained intact upon calcination and one-month storage at 67% humidity without loss of crystallinity. The results of ^{27}Al NMR and ion exchange with K^+ evidenced that 94% of the incorporated aluminium atoms remained in framework positions and served as ion exchange sites.

Recently, Ivanova et al. reported an efficient approach for the preparation of thermally stable BEC zeolite possessing Zr-associated Lewis acid sites using two post-synthesis steps (Figure 6), including: 1) solvothermal stabilization of as-made BEC germanosilicate with TEOS, followed by 2) treatment of the partially degermanated zeolite with $ZrOCl_2$ in DMSO under acidic pH. XRD, NMR, FTIR and UV–Vis spectroscopic techniques confirmed the effective incorporation of Zr into framework positions, resulting in an active and selective catalyst for the MPV reduction of levulinic acid with 1,4-butanediol. Similar TOF values found for post-synthesized and hydrothermally synthesized Zr-*BEA evidenced the identical nature of Zr active sites in both catalysts.[166]

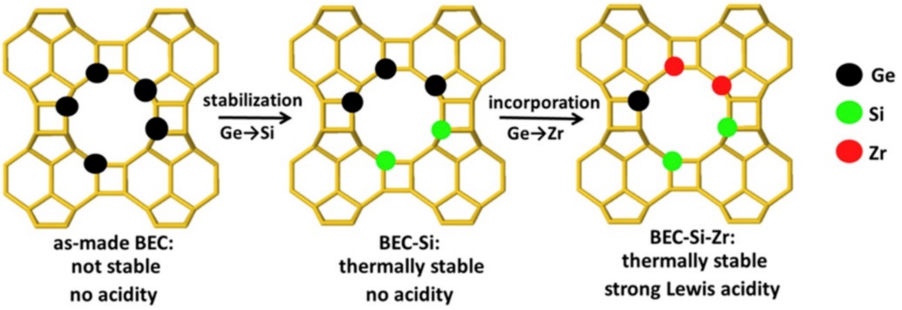

Figure 6. Two-step post-synthesis approach used in ref.[166] for the preparation of Zr-substituted BEC zeolite.

Recent researches have been also focused on tailoring the acidity by alumination of germanosilicate zeolites characterized by unidirectional location of Ge-enriched D4R units, e.g. medium-pore ITH,[132, 167, 168] large-pore IWW,[169] UOV,[170] IWR[171], and extra-large pore UTL[164] zeolites. The concentration of Al incorporated in the framework grew with the rising in 1) the concentration of used $Al(NO_3)_3$ solution (0.1 –1 M), 2) the pH (0.5 – 2), and 3) the temperature of the treatment (25 – 175 °C).[168, 171, 172]

Isomorphous incorporation of Sn atoms into the framework of extra-large pore UTL zeolite was achieved using degermanation-metallation of the as-synthesized germanosilicate (Figure 7).[173] Structural rearrangement of the UTL framework accompanied by degermanation in 1M HNO_3 was the dominating process at elevated temperatures, while restoration of the framework was observed after subsequent hydrothermal treatment in the presence of $SnCl_4{\cdot}5H_2O$. Mainly tetrahedrally coordinated Sn atoms were detected by UV-Vis and ^{119}Sn MAS NMR in the produced Sn-UTL zeolite. A detailed XRD study of the evolution of as-synthesized UTL zeolite upon acidic treatment revealed that removal of SDA and hydrolysis of Ge–O–Si bonds with formation of silanol nests took place initially (t < 75 min), while prolongation of the treatment resulted in the reinsertion of Si atoms into the framework, hindering the incorporation of Sn during the metallation step. Recently, the preparation of Ti-substituted zeolites with continuously tuneable porosity varying from medium pores (10-ring) to extra-large pores (14-ring) was reported by precisely controlling the acidic hydrolysis of UTL zeolite and the H_2TiF_6-assisted isomorphous incorporation of Ti (Figure 7).[174]

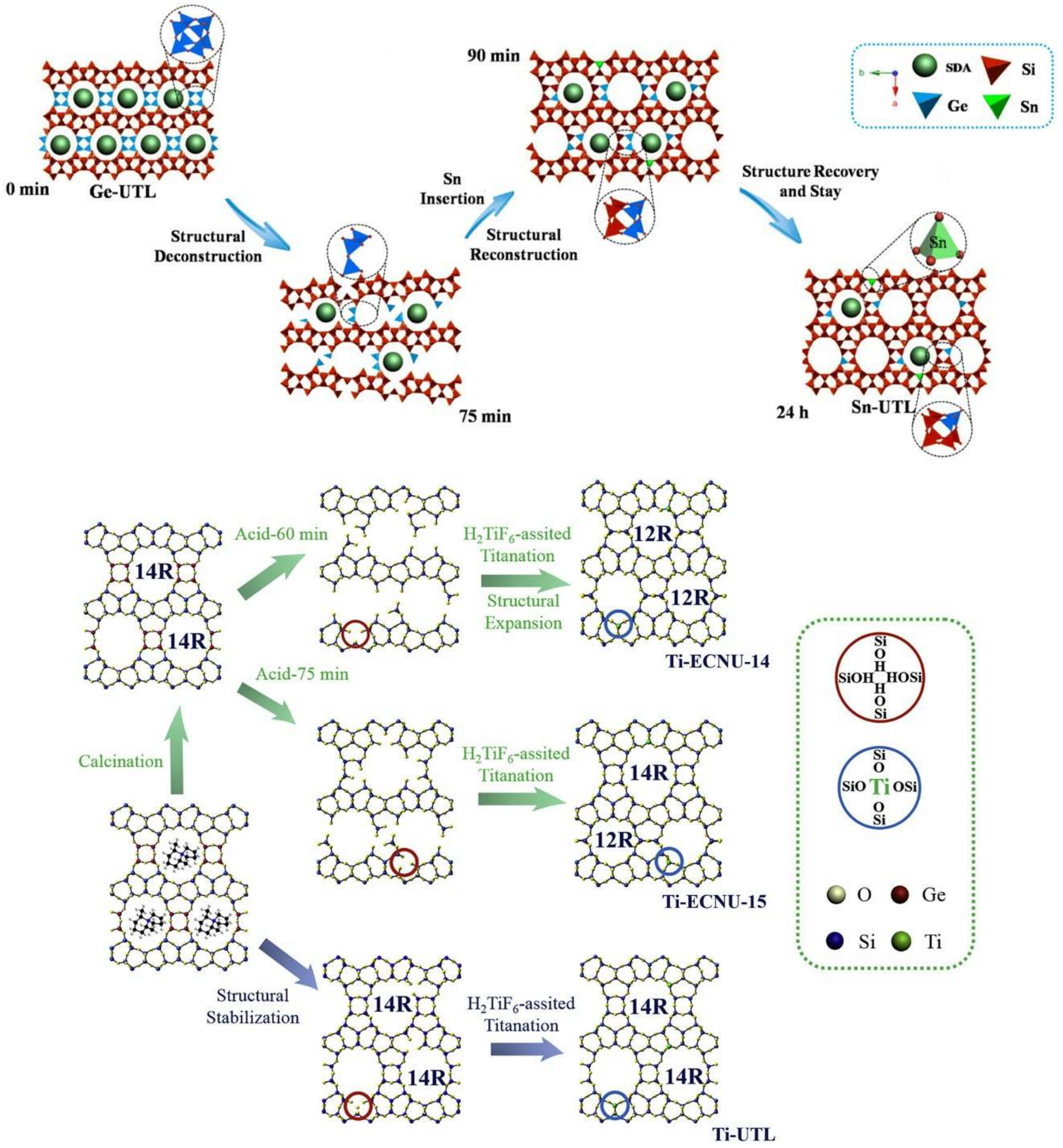

Figure 7. Strategy proposed for post-synthesizing functionalization of extra-large pore UTL zeolite via isomorphous incorporation of Sn atoms (top). Adapted from ref. [173] Strategy for post-synthesis preparation of pore size-tuneable titanosilicates via acid hydrolysis of germanosilicate UTL zeolite and subsequent H_2TiF_6-assisted isomorphous substitution (bottom). Adapted from ref. [174]

Thus, post-synthesis isomorphous substitution of Ge in zeolites is an easy and efficient approach for modification of their acidic characteristics allowing preparation of hydrolytically stable catalysts. Subsequent recovery of the extracted Ge may enhance the application prospects of germanosilicates substituted with different heteroelements.

2.4. Catalysis by Brønsted- and Lewis-acid zeolites

2.4.1. Brønsted acid catalysis

Improved accessibility of active sites in extra-large pore zeolites and decreasing diffusion path length for reacting molecules in nanocrystalline, layered, and mesoporous zeolites was shown to enhance their catalytic activity and stability in a number of reactions.

Direct correlations have been demonstrated between the concentration of acid sites at the external surface and the conversion achieved over nanolayered aluminosilicate MFI in decalin cracking catalyzed even by weak acid sites.[175] Independently on the layer thickness, nanosheet MFI catalysts were found more active, selective and stable than commercial ZSM-5 zeolite in the methanol-to-propylene (MTP) reaction.[105] However, a decrease in the crystal size enhancing the diffusivity of molecules was shown to increase the coke tolerance of nanosheet MFI in the MTP reaction.[176] Similarly, the catalytic activity and selectivity to *para*-xylene was found increasing with decreasing the MFI nanosheet thickness from 7.5 to 2.5 nm in Diels-Alder cycloaddition and dehydration reaction of 2,5-dimethylfuran (DMF) with ethylene (Figure 8).[177]

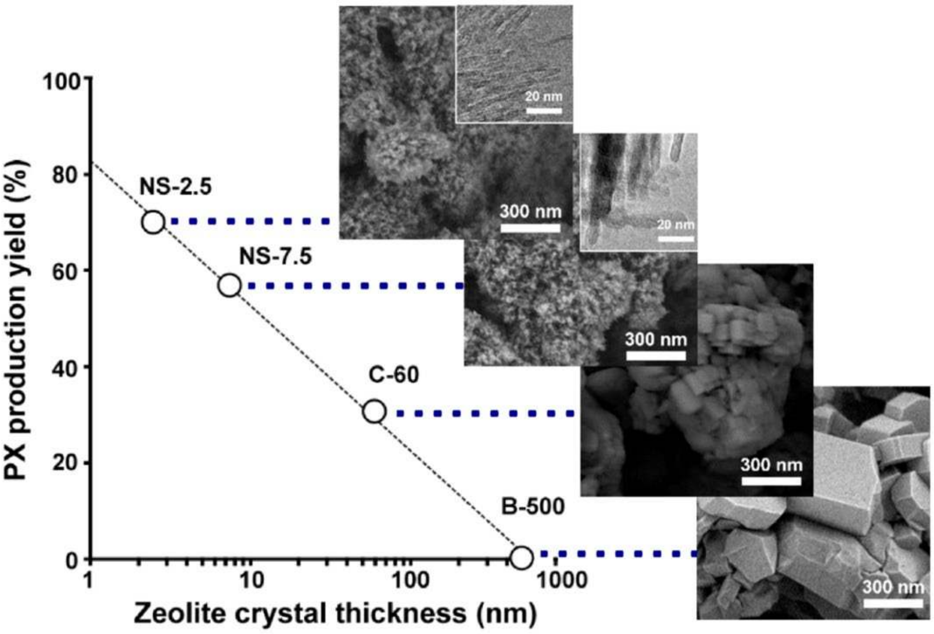

Figure 8. Increasing *para*-xylene production with decreasing thickness of zeolite MFI nanosheets in Diels-Alder cycloaddition of dimethylfuran and ethylene. [177]

The catalytic performance of aluminosilicate MFI nanosheets of different thickness (e.g. 1.7, 2.1, 2.7 nm) and mesostructure ordering was studied in the annulation of phenol (kinetic diameter = 0.66 nm), 1-naphthol (0.80 nm), and 2-naphthol (0.89 nm). A superior activity of nanosheet zeolites over conventional (3D) MFI was found for all substrates, being however more pronounced for the largest 2-naphtol (0% and 55% conversion for 3D and 2D MFI, respectively). At the same time, the activity of nanosheet MFI increased with decreasing the layer thickness, i.e. with enhancing the surface area of the studied materials.[178]

Activated sheet-like Fe-MFI was evidenced to have a higher fraction of isolated Fe^{2+} centres than bulk 3D Fe-MFI and hence showed lower activity in the catalytic decomposition of N_2O (catalyzed by oligomeric Fe), but displayed higher activity in the oxidation of benzene to phenol with N_2O (catalyzed by monomeric Fe). [179] Besides higher activity, nanosheet Fe-MFI showed longer lifetime in benzene oxidation vs. 3D Fe-MFI. The rate of deactivation for 2D Fe-MFI decreased with Fe content. Later on, it was shown that the amount of Fe and thickness of zeolite nanosheets had a decisive effect on the degree of Fe agglomeration, and hence on the catalyst performance in benzene oxidation. [180] Decreasing the Fe content in the catalyst strongly suppressed secondary reactions of phenol and increased the catalyst longevity. Fe-MFI synthesized using C_{22-6-3} SDA (domain size ~3 nm) and containing 0.24 wt% Fe was found to be a superior catalyst than the 3D counterpart and Fe-MFI nanosheets with 6 – 8 nm thickness synthesized using $C_{22-6-6-6-3}$ SDA.

MFI zeolite nanosponges with crystal thickness of 20 nm and 200 nm showed remarkably higher lifetime, toluene conversion and xylene yield in toluene methylation as compared to bulk MFI zeolite.[181] Higher activity of nanosponge vs. 3D MFI in glycerol etherification with *tert*-butyl alcohol [182] and Pechmann condensation of pyrogallol and resorcinol with ethyl acetoacetate[183] was attributed to the acid sites located on the external surfaces accessible for the reaction of bulky reactants. Zeolite *BEA nanosponge catalysts showed higher activity in the cycloaddition of DMF to ethylene,[184] Friedel-Crafts alkylation of benzene,[185] and tetrahydropyranylation of alcohols[186] as compared to catalysts reported previously.

Nanosized MFI zeolites with similar number of Brønsted acid sites (Si/Al = 23.6) synthesized in hydroxide and fluoride medium using seed-assisted crystallization have been compared as catalysts for the methanol-to-hydrocarbons (MTH) reaction.[187] A superior activity and resistance to deactivation of nano-MFI synthesized in fluoride-containing medium was related to the hydrophobic nature of its surface.

A decrease in the crystal size (from 1200 to 100 nm) of Al-MFI zeolite prepared via microemulsion method in a water/polyoxyethylene-(15)-oleyl ether/cyclohexane medium resulted in lower selectivity to undesired aromatic products in the acetone-to-*iso*-butylene conversion. Moreover, lowering the strength of acid sites in Fe- vs. Al-substituted MFI nanocrystals effectively inhibited the formation of aromatics and coke, leading to further increase in *iso*-butylene selectivity.[87]

The benefits of several extra-large pore zeolites have been demonstrated for some acid-catalyzed reactions. The presence of Brønsted acid sites accessible through the 18×10×10-ring pore system conditioned the high activity and selectivity to targeted cumene of ITT (ITQ-33) zeolite in the industrially relevant alkylation of benzene with propylene.[188] Moreover, the higher stability of extra-large pore ITT vs. large-pore *BEA in the alkylation reaction was explained by the easier diffusion of alkylated benzene in the pores of ITT. The use of ITT in catalytic cracking of vacuum gasoil allowed to concomitantly maximize the yields of valuable propylene and diesel (at the expense of gasoline) in comparison with commercial USY and *BEA zeolites[68] due to the unique structure of ITT containing interconnected extra-large 18-ring and medium 10-ring pores. While the 18-ring pores were claimed responsible for the easy diffusion of bulky diesel molecules, the 10-ring pores provided diffusion and cracking of gasoline-range hydrocarbons to produce C_3 and C_4 olefins.

A beneficial behaviour of Al-ITV with 30×30×30-ring pore system over commercial large pore *BEA zeolite of similar chemical composition and crystal size was shown in the acetalyzation of diphenylacetaldehyde with triethyl orthoformate. Al-ITV showed almost three times higher TOF (53 vs. 18 h^{-1}) and better selectivity to the targeted acetal (87 vs. 55%) than *BEA zeolite.[69]

The catalytic behaviour of Al-UTL possessing both extra-large and large pores in the same structure was compared to that of extra-large pore Al-DON zeolite with one-dimensional pore system in the dealkylation of tri-isopropylbenzene (TIPB) and di-isopropylbenzene (DIPB). [63] The reaction rates for Al-UTL (9.5 $g \cdot g^{-1}_{cat} \cdot s^{-1}$) and Al-DON (9.9 $g \cdot g^{-1}_{cat} \cdot s^{-1}$) were similar in the dealkylation of bulky TIPB, which is able to diffuse only through the 14-ring pores of both zeolites. However, a much higher dealkylation rate of smaller DIPB was reached over Al-UTL (8.8 $g \cdot g^{-1}_{cat} \cdot s^{-1}$) providing a 2D pore system relative to Al-DON (5.5 $g \cdot g^{-1}_{cat} \cdot s^{-1}$) possessing 1D 14-ring pores.[63] The extra-large pore Al-UTL appeared to be a more active and selective catalyst for the benzoylation of *para*-xylene than the large-pore aluminosilicate zeolite Al-*BEA owing to the higher accessibility of the active sites in the former. In contrast to the benzoylation of *para*-xylene, requiring a large space for the formation of the aromatic intermediate, the preferences of the larger size of UTL channels were not so obvious in the Beckmann rearrangement of quite small 1-indanone oxime molecules.[189]

Improved acidity and developed mesoporosity in post-synthetically prepared zeolites were naturally reflected in their catalytic behavior. In a model reaction of propanol tetrahydropyranylation, the enhanced concentration of strong Brønsted acid centres resulted in a remarkably high activity of aluminated ITH (40% yield), IWW (80% yield), and UTL (80% yield) zeolites in contrast with the inactive initial germanosilicates.[164] The development of mesopores during post-synthesis alumination of Ge-rich ITH zeolite resulted in a higher activity of the respective hierarchical micro-mesoporous catalyst in the tetrahydropyranylation of propanol in comparison with the directly synthesized microporous Al-containing zeolite with close chemical composition (40 vs. 20% yield).[168, 190] This trend became more prominent with increasing the kinetic diameter of substrates under investigation (methanol (3.6 Å) < 1-propanol (4.7 Å) < 1-hexanol (6.2 Å)).

Enhancing the accessibility of active sites resulted in an increased activity and stability of zeolite catalysts, while tailoring the nature of acid sites enabled further improvement of their catalytic performance if the rates of targeted and side reactions are controlled by the intrinsic strength of an acidic site. In this way, a comparison of the catalytic performance of Al- and mixed Al,Fe-substituted nanosized MTW zeolites in the conversion of methanol to propylene revealed the higher yields of propylene and butenes over Al,Fe-MTW catalyst. The result was related to the lower acid strength of Al,Fe-MTW vs. Al-MTW inhibiting consecutive reactions leading to aromatic formation[191]. It was recently demonstrated that the strength of Brønsted acid sites in MFI zeolite can be optimized by simultaneous incorporation of Al^{3+} and Fe^{3+} into the framework for the maximization of propylene selectivity in the MTH reaction.[192] Later on, nano-Fe-MFI catalyst prepared by an emulsion method was shown to suppress consecutive reactions leading to aromatics and coke in the methanol-to-olefins (MTO) reaction in comparison with nano-Al-MFI, although the weaker acid sites of nano-Fe-MFI did not catalyze higher alkene cracking. Employing the nanosized MFI ferroaluminosilicate during the MTP reaction gave the best propylene selectivity (44 and 33 mol% for (Fe, Al)- and Al-MFI, respectively) in conjunction with a high propylene/ethylene (P/E) ratio (11.5 and 4.2 for (Fe, Al)- and Al-MFI, respectively), at 450 °C.[193]

Incorporation of boron was shown to significantly increase the lifetime of MFI zeolites in MTH processes. [194, 195] While showing the same activity and selectivity, boron-modified nanocrystalline MFI zeolite prepared by a facile salt-aided seed-induced route demonstrated much higher lifetime (725 h) in the MTH process in comparison with either aluminosilicate nanocrystalline (120 h) or microcrystalline (80 h) zeolites. The advantageous stability of B,Al-MFI catalyst was attributed to the cooperative effect of its hierarchical structure and modified acidity.[194] In agreement with ref.[194], incorporation of boron to MFI nanocrystals resulted in a lower rate of coke formation, and consequently in an improved long-term stability, which was related to the decreased density of strong Brønsted acid sites in B,Al-MFI vs. Al-MFI.[195]

The effect of the crystal size and acid strength on gas-phase glycerol dehydration for Ga- and Al-substituted MFI zeolites was studied in ref.[86] (Figure 9). While Al-substituted MFI zeolites showed higher selectivity to targeted acrolein, Ga-containing MFI with weaker Brønsted acid sites demonstrated longer catalytic stability. In addition to differences in the strength of the Brønsted acid sites, the size of zeolite crystals affected the nature of the coke molecules deposited on the catalysts. Thus, while polyglycol molecules were preferentially formed at the external surfaces of small zeolite particles (1.5 μm), polyaromatic compounds were mainly detected inside the micropores of large MFI crystals (10 – 12 μm), especially in Al-substituted samples having a higher number of strong Brønsted acid sites (Figure 9).

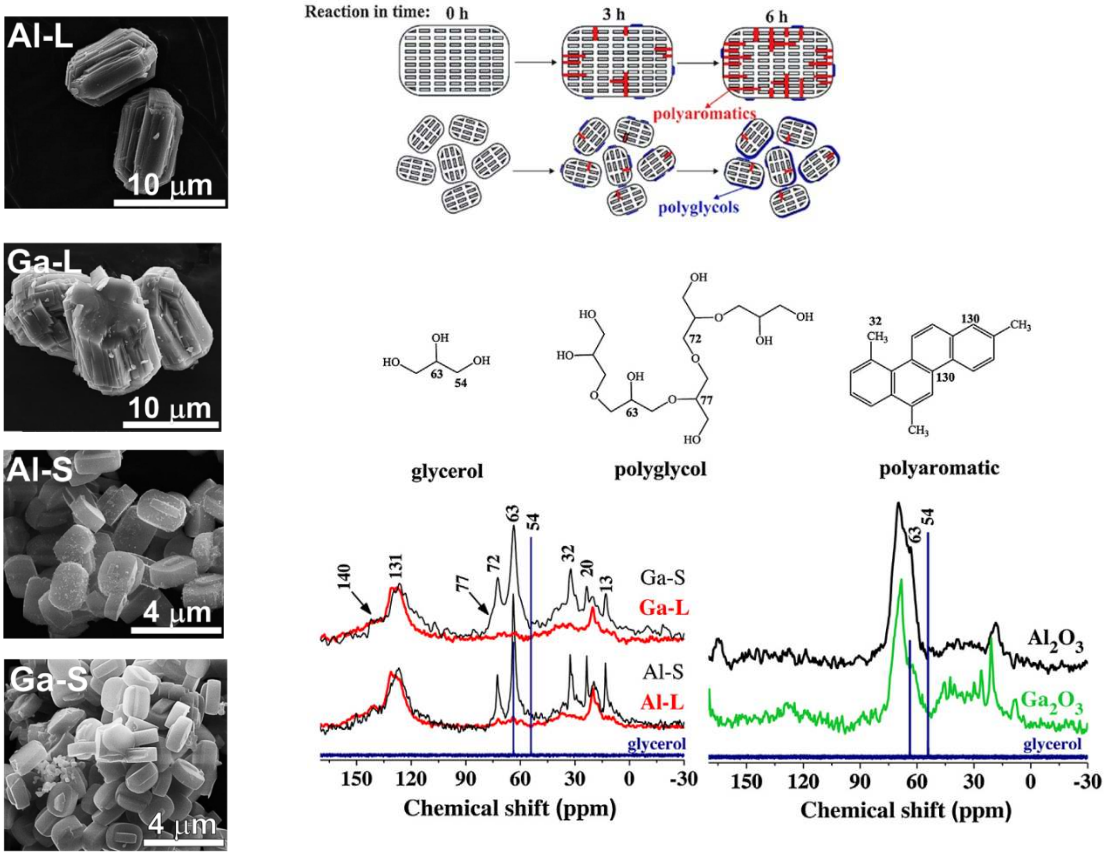

Figure 9. SEM images of Al- and Ga-substituted MFI zeolites of different crystal size (L: large crystals; S: small crystals) (left). Schematic representation of the domains of coke deposition and location in the zeolite pores during glycerol dehydration on the MFI zeolites. ^{13}C NMR spectra for spent Al- and Ga-substituted MFI zeolites showing preferential formation of polyaromatic compounds in bulky zeolite crystals (Ga-L, Al-L) and of polyglycol molecules over small zeolite crystals (Ga-S and Al-S) and aluminium and gallium oxides (bottom). [86]

Incorporation of Ga into nanosized MFI zeolite using seed-induced hydrothermal synthesis increased the concentration of weak Brønsted and strong Lewis acid sites resulting in a higher aromatic yield during the aromatization of 1-hexane compared with Al-containing MFI nanocrystals (Figure 10).[196]

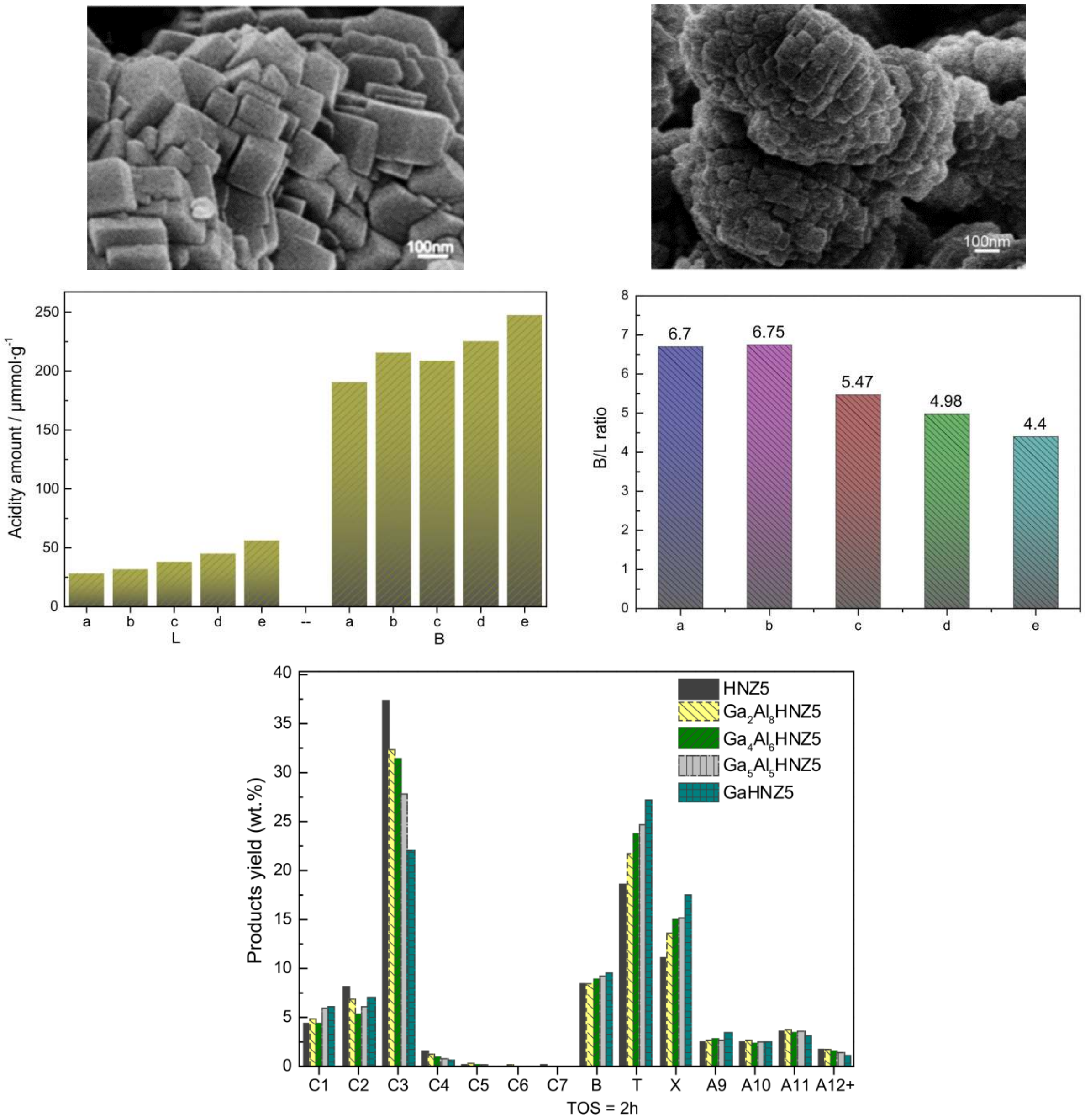

Figure 10. SEM images of nanosized Al- (top left) and Al, Ga-substituted (top right) MFI zeolites. Distribution of acid sites showing increasing fraction of strong Lewis centres with increasing the ratio between Ga and Al atoms (from a to e) (middle). The products distribution of 1-hexene aromatization over nanosized MFI zeolites showing increasing yield of aromatic BTX fraction with increasing the ratio between Ga and Al atoms (bottom). [196]

Nanosheet MFI zeolites with tailored strength of acid sites obtained by hydrothermal crystallization of Al-, Ga-, Fe-, and B-containing silica gels using C_{22-6-6} SDA were tested in the MTH reaction. Due to the shorter residence time of aromatic coke precursors in the micropores, Al-substituted nanosheet MFI showed longer lifetime vs. its 3D analogue. While the bulk Ga-MFI showed better catalytic performance than bulk Al-MFI, the nanosheet Ga-MFI sample was found to be nearly inactive, which was related to the much lower degree of T^{3+} elements incorporation noted for 2D vs. 3D MFI. Both 3D and 2D Fe- and B-substituted MFI were inactive in the MTH reaction because of the low strength of the respective T^{3+}-associated acid sites.[197]

Fe-, Ga-, and Al-substituted MFI nanosheets were applied in the catalytic cracking of *n*-dodecane under the pressure of 4 MPa.[198] Higher activity for cracking of *n*-dodecane and lower deactivation by carbon deposition was observed when using ultrathin MFI lamellas as catalyst. Higher amount of light alkenes and heat sink were reached over isomorphously substituted MFI nanosheet zeolites when compared with bulk MFI (Figure 11, left). The heat sink (at T = 600 °C) increased in the following sequence of 2D T^{3+}-MFI zeolites (Figure 11, right): Al- (3124 kJ/kg) < Fe- (3221 kJ/kg) < Ga- (3384 kJ/kg), indicating that the acid strength of MFI nanosheet zeolites has a remarkable effect on the catalytic cracking of *n*-dodecane.

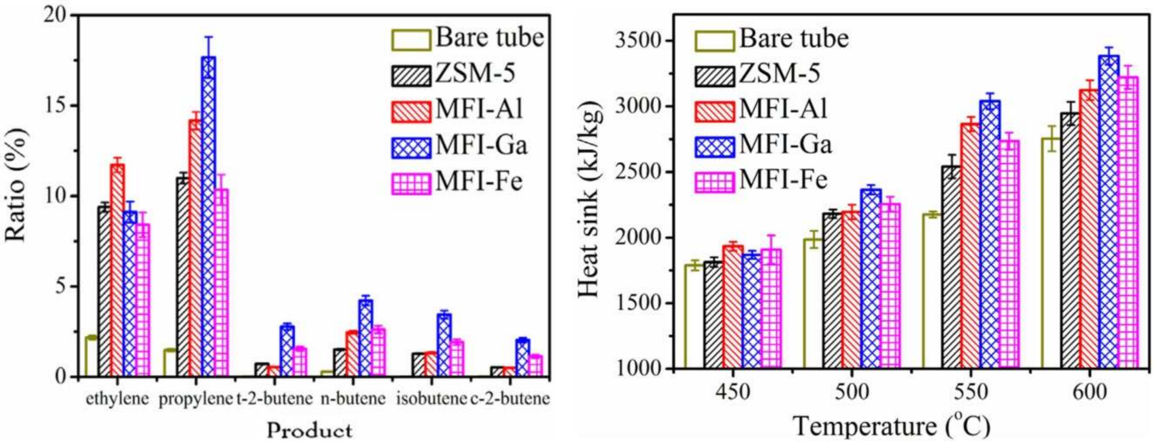

Figure 11. Selectivity to light olefins (left) and heat sinks at different temperatures (right) of *n*-dodecane cracking over isomorphously substituted MFI nanosheet zeolites vs. commercial ZSM-5. [198]

A correlation between the yield of targeted cumenes and the strength of the acid sites was reported for the alkylation of toluene with isopropyl alcohol over B-, Al-, Ga-, and Fe-containing extra-large pore UTL zeolites. A higher percentage of cumenes vs. side xylenes is observed at sites of lower acid strength, while the competing disproportionation reaction considerably lowered the selectivity over the most acidic Al-UTL.[199] Ga-UTL containing Brønsted acid sites of medium strength exhibited the highest activity and selectivity in the benzoylation of *para*-xylene while poorer performance was found for weakly acidic B- and strongly acidic Al-UTL. [189] The result was accounted for by the competition of two tendencies: i) the increase in the formation rate of the Wheland type aromatic intermediate with the increase in the amount of strong Brønsted acid sites (B < Ga < Al), and ii) the decrease in the desorption rate of the target 2,5-dimethylbenzophenone from the active sites with the increase in their strength (B > Ga > Al).

2.4.2. Lewis acid catalysis

While the benefits of recently synthesized Sn-substituted zeolites were demonstrated in reactions involving the activation of C-O bonds (e.g. isomerization of sugars, BV oxidation of cyclic ketones and aromatic aldehydes), Ti-containing zeolites are efficient catalysts for the epoxidation of alkenes with aqueous H_2O_2.

Ref. [173] is a rare example reporting on the catalytic performance of Sn-substituted extra-large pore zeolite. It was shown that both nanocrystalline Sn-*BEA and extra-large pore Sn-UTL zeolites display higher activity in the BV oxidation of cyclohexanone with H_2O_2 in comparison with microcrystalline Sn-*BEA zeolite (Figure 12, left). At the same time, Sn-UTL possessing larger pores showed the highest conversion of ketone among the investigated catalysts when bulkier 2-adamantanone and TBHP were used as substrate and oxidant (Figure 12, right), respectively. The preferential behaviour of Sn-UTL was explained by a favoured diffusion of the bulky substrate in the extra-large pores.

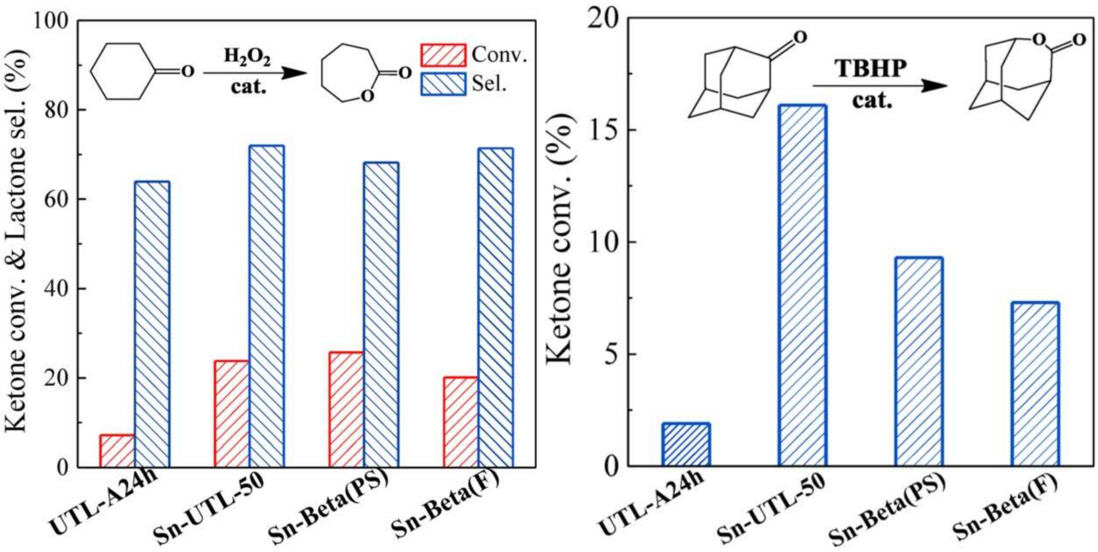

Figure 12. BV oxidation of cyclohexanone with H_2O_2 (left) and TBHP (right) over Sn-substituted extra-large pore UTL and large pore *BEA zeolites. Sn-UTL-50 refers to post-synthesized Sn-containing UTL zeolite, Sn-Beta(PS) – post-synthesized Sn-*BEA zeolite, Sn-Beta(F) – *BEA zeolite synthesized directly in F-containing gel. Adapted from ref. [173]

The activity of Ti-substituted extra-large pore UTL zeolite (TOF = 29.3 h^{-1}) in the epoxidation of cyclohexene with bulky TBHP was higher than that exhibited by large pore Ti-MWW (11.8 h^{-1}), Ti-*BEA (12.4 h^{-1}), Ti-MOR (2.2 h^{-1}) and especially medium-pore Ti-MFI (0.2 h^{-1}) zeolites with similar chemical composition.[174] In contrast, when using small H_2O_2 as oxidant, Ti-UTL (Si/Ti = 139) and Ti-*BEA (Si/Ti = 116) catalysts performed similarly in the epoxidation of bulky olefins (e.g. linalool, cyclooctene, norbornene).[82]

Among recently synthesized T^{4+}-substituted zeolite-based catalysts, the ones containing hierarchical pore systems earn a special attention. 3DOm-imprinted mesoporous Sn-MFI offered significant improvements for the isomerization of xylose (18 times higher TOF vs. conventional Sn-MFI) and glucose (14 times higher TOF vs. conventional Sn-MFI) compared to conventional Sn-MFI (crystal size 60 μm × 15 μm × 3 μm) due to the enhanced molecular transport in the hierarchical zeolite (Figure 13). [101]

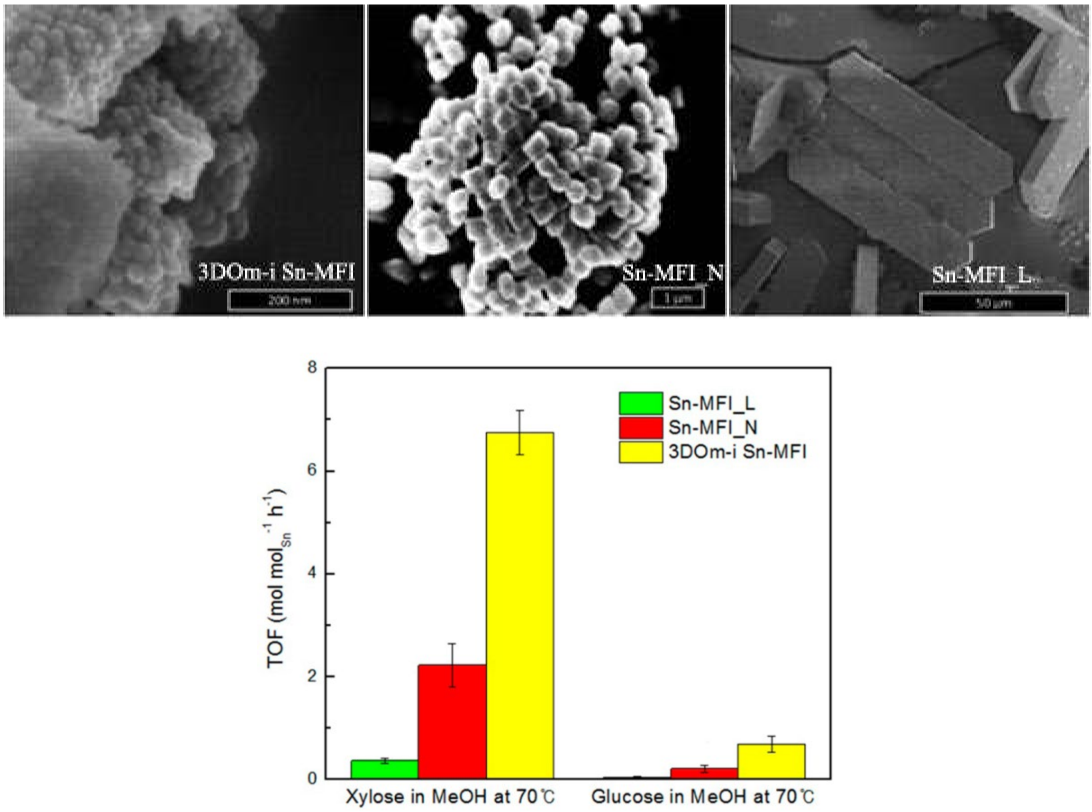

Figure 13. SEM images of Sn-MFI zeolites synthesized using 3DOm-i (top left), conventional hydrothermal OH^-- (top middle) and F^-- assisted (top right) synthesis. Initial catalytic activities of Sn-MFI catalysts for isomerization of xylose and glucose (bottom). [101]

While the activity of mesoporous Ti-MFI microspheres prepared via F127 triblock copolymer-assisted synthesis was similar to conventional microporous TS-1 in 1-hexene epoxidation with H_2O_2, it exhibited a higher conversion in the oxidation of bulky 3-picoline (44.0 vs. 29.9%) and cyclohexene (20.5 vs. 9.5%) due to the presence of mesopores.[97] Despite the catalytic activity of external Ti-associated sites in nanolayered MFI zeolites was found lower than that of internal ones for epoxidation of 1-hexene, 2D Ti-MFI was superior to its 3D analogue for epoxidation of highly reactive, though bulkier cycloalkenes (8.5 vs. 0.6% yield of cyclooctene oxide over 3D and 2D Ti-MFI, respectively).[110] The treatment of nanosheet Ti-MFI with an aqueous solution of NH_4F improved both the activity of external Ti sites (14.5% yield of cyclooctene oxide) and the selectivity to epoxide (95 vs. 91%) due to the reduced amount of silanol groups. [110]

Self-pillared Sn-MFI layers possessing both micro- and mesopores showed unprecedented activity and selectivity in lactose-to-lactulose isomerization (97%

selectivity at 31% of lactose conversion) relative to Sn-*BEA and Sn-MCM-41 as well as to earlier reported catalysts (Figure 14).

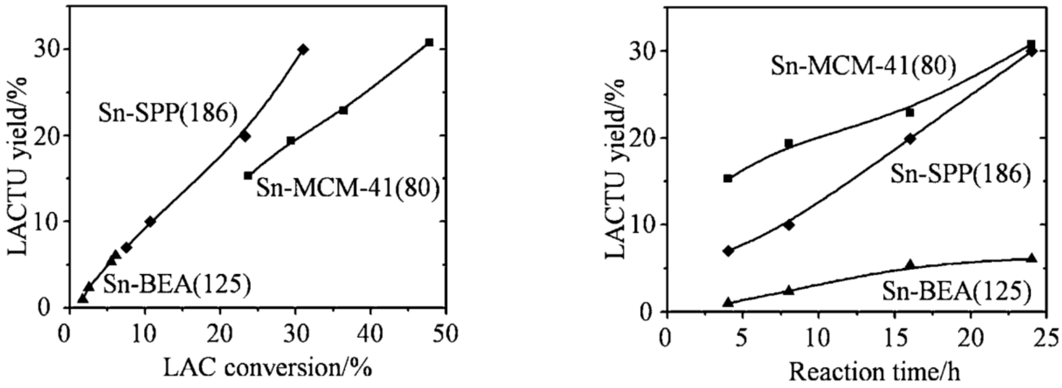

Figure 14. Lactulose (LACTU) yield versus lactose (LAC) conversion (left) and LACTU yield versus LAC isomerization reaction time (right) over different catalysts: Sn-substituted MCM-41 molecular sieve (Si/Sn = 80), Sn-*BEA (Si / Sn = 125) zeolite prepared via F^- -assisted hydrothermal synthesis and self-pillared MFI/MEL intergrowth. [119]

Nanosheet 2D Sn-MFI, prepared via a surfactant-assisted approach, showed higher activity for the BV oxidation of 2-adamantanone with H_2O_2 than bulk 3D Sn-MFI (TON (at 16 h) = 122 vs. 17, TOF (h^{-1}) = 38 vs. 5 for 2D and 3D Sn-MFI, respectively), while exhibiting a superior thermal and hydrothermal stability relative to Sn-MCM-41. [111]

The catalytic performance of nanocrystalline T^{4+}-substituted zeolites produced usually via a two-step demetallation-metallation approach was also shown to be superior to that of hydrothermally synthesised microcrystalline catalysts. The activity of post-synthesized Ti-MOR nanocrystalline catalysts in the hydroxylation of toluene (TON = 20 vs. 1 mol·(Ti-mol)$^{-1}$ at initial 1 h) and the ammoximation of cyclohexanone (initial reaction rate 344.4 vs. 40.0 mmol·g^{-1}·h^{-1}) was shown to decrease with increasing crystal size. [142] Post-synthesized Sn-*BEA (0.65 wt% Sn) showed 10% higher conversion of ketone in the BV oxidation of 2-adamantanone with H_2O_2 than conventional Sn-*BEA-F (0.72 wt% Sn) hydrothermally synthesized in F-containing medium and lacking silanol surface groups. Thus, it was concluded that “the diffusion issue may dominate the reaction over the hydrophobic nature of the catalyst”.[134] Hierarchical Sn-*BEA zeolite recently prepared by mixing dealuminated *BEA with $SnCl_4$ followed by TEAOH-assisted hydrothermal treatment showed higher activity in the conversion of fructose to methyl lactate (41 vs 22% yield) than hydrothermally-synthesized Sn-*BEA with the same crystal size and concentration of acid sites. Better performance of post-synthesized Sn-*BEA was attributed to the presence of mesopores enhancing the diffusion of reagents.[200] Similarly, hierarchical Sn-*BEA produced by sequential desilication/dealumination treatment followed by solid-state metallation showed superior activity and stability in MPV reduction of bulky cyclododecanone (kinetic diameter 8.4 Å) in comparison with purely microporous Sn-*BEA and mesoporous Sn-MCM-41. The rate of reaction achieved over hierarchical Sn-*BEA was over one order of magnitude higher than that obtained for microporous and mesoporous catalysts. Moreover, only a limited loss of activity (<20%) was observed after 700 h on stream when using hierarchical Sn-*BEA, while microporous Sn-*BEA lost about 70% activity after only 200 h on stream.[152]

The concentration of framework and extra-framework $T^{4+}O_x$ species formed upon post-synthesis preparation of T^{4+}-substituted zeolites strongly influenced their catalytic behaviour. Post-synthesized Sn-*BEA with low Sn loading (0.03 $mol_{Sn}/g_{zeolite}$) possessing exclusively tetrahedrally coordinated Sn atoms in framework positions showed higher TOF than directly synthesized Sn-*BEA in the isomerisation of glucose (511 vs. 305 h^{-1}). At the same time, increasing Sn loading resulted in the formation of condensed SnO_x species that significantly diminished the catalyst activity (TOF = 511, 84, and 46 h^{-1} for 0.03, 0.23, and 0.38 $mol_{Sn}/g_{zeolite}$, respectively).[201] Similarly, the increase in Sn loading decreased the productivity of the catalyst in the isomerization of glucose and the MPV reduction of cyclohexanone, as extra-framework Sn species are not active in these reactions.[136] Conversely, increasing Sn loading positively affected the productivity of post-synthesized Sn-*BEA in the BV oxidation of cyclohexanone, a reaction catalyzed by both framework and extra-framework Sn species.

The control over the concentration and nature of active sites in post-synthesized T^{4+}-substituted zeolites is also an important variable for their catalytic application. A comparison of the catalytic performance of hierarchical T^{4+}-substituted *BEA zeolites produced via post-synthesis demetallation-metallation in the aminolysis of styrene oxide with aniline revealed the highest activity of Zr-*BEA vs. Sn- and Ti-substituted zeolites (TON = 936, 660, and 476 a.u. for Zr-, Ti-, and Sn-*BEA, respectively) due to an optimal strength of the Zr-associated Lewis acid sites.

[153] The concentration of Lewis acid sites in post-synthesized Sn-*BEA correlated linearly with the Sn content, while the activity per Sn-site (TOF) in 1,3-dihydroxyacetone-to-methyl lactate conversion decreased with increasing Sn concentration. The result was rationalized by considering differences in the ratio between Sn-associated "closed" and "open" Lewis acid sites and the higher activity of the latter ones, as supported by DFT calculations.[138] Post-synthesized Zr-*BEA enriched with "open" Zr Lewis acid sites showed extremely high catalytic performance in ethanol-to-butadiene conversion in comparison with directly synthesized Zr-*BEA zeolite. [141]

2.4.3. Cascade reactions over multifunctional zeolites

In a pioneering work, Corma et al. reported the one-pot synthesis of phenols by cascade BV oxidation of aromatic aldehydes with subsequent ether hydrolysis using bifunctional Sn,Al-*BEA zeolite (Scheme 5).[202]

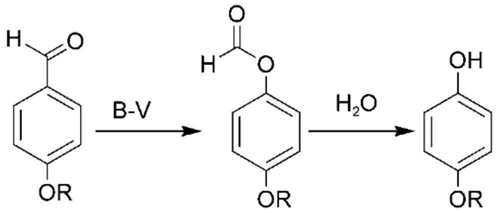

Scheme 5. Cascade BV oxidation of aromatic aldehydes with subsequent ether hydrolysis for one-pot synthesis of phenols. [202]

Testing of a set of directly synthesized Sn,Al-*BEA zeolites with close amounts of Sn (2.0 – 2.6 wt%) and variable Al content (Si/Al = 28 – ∞) in the BV oxidation of *para*-anisaldehyde with H_2O_2 showed the enhancing yield of phenol with increasing the concentration of framework aluminium due to the acceleration of the hydrolysis step by Brønsted acid sites. Besides the significant improvement in selectivity to phenol (46 vs. 89% for Sn-*BEA and Al,Sn-*BEA (Si/Al = 28), respectively), the growth in *para*-anisaldehyde conversion was also observed with increasing the number of Brønsted acid sites in the zeolite, indicating that bridging hydroxyls are active sites for the BV oxidation of aldehydes.

Later on, the unprecedented productivity of post-synthesized Sn,Al-*BEA (2113 $g_{EL}\cdot kg_{catalyst}^{-1}\cdot h^{-1}$) vs. Sn-*BEA (1131 $g_{EL}\cdot kg_{catalyst}^{-1}\cdot h^{-1}$) in the conversion of 1,3-dihydroxyacetone (DHA) to ethyl lactate (EL) was reported.[145] The reaction involves two steps (Scheme 6): 1) rate-determining dehydration of DHA to pyruvic aldehyde (PA) more efficiently catalyzed by Brønsted acid sites, and 2) hydride shift converting PA (as well as ethyl hemiacetal (PAEH) reversibly formed from PA in EtOH) to EL over Lewis acid sites.

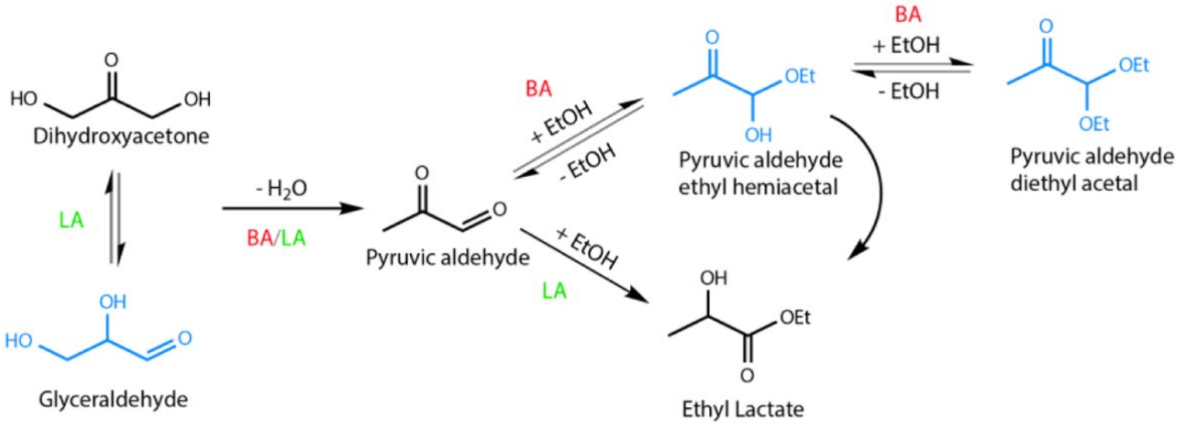

Scheme 6. Different reaction pathways in conversion of 1,3-dihydroxyacetone into ethyl lactate. The main reaction of dihydroxyacetone to ethyl lactate is pictured in black, and products of the side reaction are displayed in blue. The catalytic site needed for each reaction is displayed: Brønsted acid (BA) is shown in red, Lewis acid (LA) is shown in green. [145]

Despite accelerating the dehydration step and enhancing the productivity, an excess of Brønsted acid sites in the bifunctional catalyst may promote the irreversible transformation of PAEH to pyruvic aldehyde diethyl acetal (PADA), decreasing the selectivity towards EL. Thus, a proper balance between the two types of active sites is typically required to design highly productive and selective catalysts. The post-synthesis approach based on partial dealumination of *BEA zeolite followed by grafting with $SnCl_4·5H_2O$ in dry isopropanol allowed to tune the ratio between Brønsted and Lewis acid sites by adjusting the duration of the dealumination step and the $SnCl_4·5H_2O$-to-zeolite ratio during metallation. The optimal Sn/Al ratio providing fast and selective DHA-to-EL conversion was found to be 2. Sn,Al-*BEA showed the highest productivity (2113 $g_{EL}·kg_{catalyst}^{-1}·h^{-1}$) at 3.6 wt% Sn loading, while higher Sn content lead to additional formation of inactive SnO_2. The proximity of both Brønsted and Lewis acid sites in one framework was proven to be responsible for the beneficial catalytic effect, as a physical mixture of Sn-*BEA and Al-*BEA showed 1.4-fold lower productivity vs. bifunctional Sn,Al-*BEA catalyst.

The use of bifunctional Sn,Al-*BEA zeolite was also reported to enable the one-pot production of furylglycolic acid from cortalcerone.[146] Cortalcerone is firstly dehydrated over Brønsted acid sites to form furylglyoxal hydrate, which is then upgraded to furylglycolic acid through an intramolecular MPV hydride shift catalyzed by Sn-associated Lewis acid sites (Scheme 7).[146]

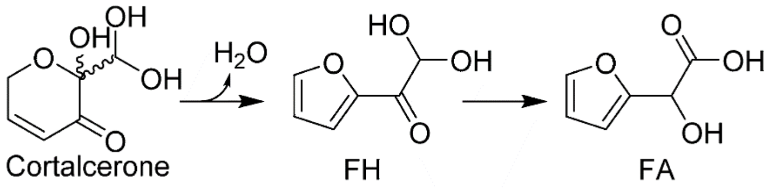

Scheme 7. Conversion of cortalcerone to furylglycolic acid. Dehydration of cortalcerone to furylglyoxal hydrate (FH) proceeds over Brønsted acid sites, while isomerization of FH to furylglycolic acid (FA) takes place over Lewis acid centres.

A balanced ratio between the different types of acid sites was again required in order to achieve both the highest conversion of cortalcerone and selectivity to FA. Thus, the highest yield of FA (22%) was reached when using Sn,Al-*BEA with Si/Al = Si/Sn = 200. Increasing the concentration of Brønsted acid sites (i.e. drop in Si/Al ratio) resulted in increased FH degradation and deposition of carbonaceous residues deactivating the catalyst, while decreasing the number of Lewis acid sites (i.e. growth in Si/Sn ratio) decreased the selectivity to FA.

Conversion of the biomass-derived furfural into γ-valerolactone (GVL) is another important multistep process involving Lewis acid-catalyzed MPV reductions (e.g. furfural-to-furfuryl alcohol, alkyl levulinate-to-GVL) and Brønsted acid-catalyzed hydration steps (e.g. furfuryl ether-to-alkyl levulinate) (Scheme 8).

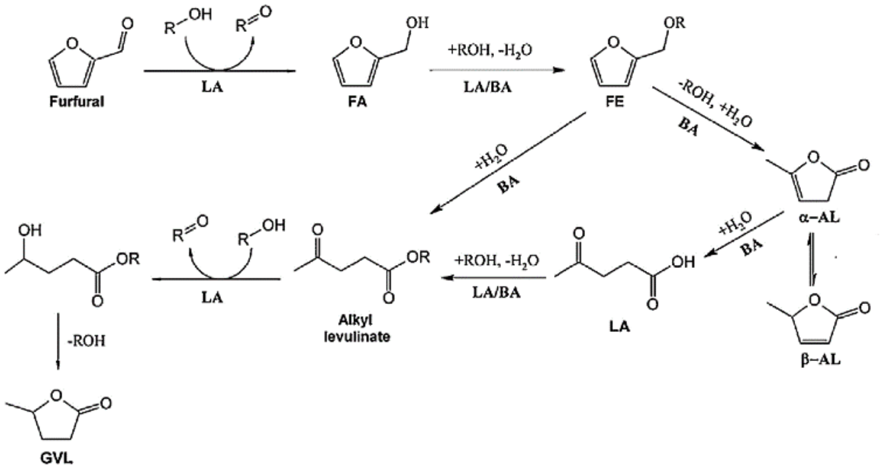

Scheme 8. Reaction pathways for the one-pot conversion of furfural to GVL (BA: Brønsted acid, LA: Lewis acid, FA: furfuryl alcohol, FE: furfuryl ether, α- or β-AL: α- or β-angelica lactones). [147]

The optimization of acid properties of bifunctional Sn,Al-*BEA catalysts was carried out to increase their efficiency in the one-pot furfural-to-GVL conversion.[147] Sn,Al-*BEA zeolites with different Si/Al ratios and Sn loadings were prepared via post-synthesis dealumination-metallation. Due to the more efficient incorporation of Sn into the framework, Sn,Al-*BEA prepared by solid-state ion exchange with dimethyltin dichloride was more efficient in converting furfural to GVL than catalysts prepared by solid-state ion exchange with tin(II) acetate or by isopropyl alcohol-assisted grafting with $SnCl_4 \cdot 5H_2O$. A higher level of dealumination was shown to create more active framework Sn sites in the catalyst than a lower one, enhancing GVL yield despite the reduced concentration of Brønsted acid sites. Sn,Al-*BEA with atomic ratios Si/Sn=72 and Si/Al= 473 demonstrated the highest GVL yield (60 % at 180 °C in 2-butanol after 24 h) due to the moderate Brønsted acidity and appropriate concentration of Lewis acid sites associated to framework Sn species.

Highly selective conversion of furfural to GVL (95% yield at 120 °C for 24 h) was found when using a mesoporous Zr,Al-*BEA zeolite prepared by a multiple-step post-synthesis strategy comprising controlled dealumination, desilication, and metal incorporation via dry impregnation of Cp_2ZrCl_2.[148] The key feature of the best performing catalyst was shown to be an optimized ratio between Brønsted and Lewis acid sites (Si/Al = 100, Si/Zr = 77).

The development of highly selective tandem transfer hydrogenation/etherification of furfural-to-(butoxymethyl) furan (BMF) over bifunctional Sn,Al-*BEA catalyst enabled the continuous production of bio-renewable furanic ethers having potential as fuel additives (Scheme 9).[149]

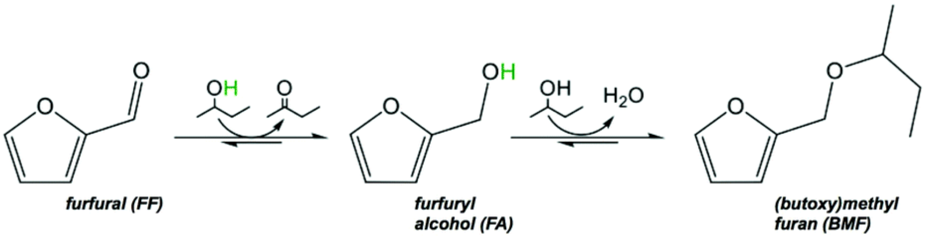

Scheme 9. Catalytic conversion of furfural to (butoxy)methyl furan.[149]

Bifunctional Sn,Al-*BEA catalysts produced via partial dealumination-metallation displayed improved selectivity to BMF (75%), but lower activity (TOF = 0.08 min^{-1}) in comparison with isolated Lewis Sn-*BEA catalyst (35%, 0.17 min^{-1}) or a physical mixture of Sn-*BEA and Al-*BEA (35%, 0.19 min^{-1}). The lower activity of Sn,Al-*BEA vs. Sn-*BEA was rationalized by the presence of non-active SnO_x species in the bifunctional catalyst, shown to be formed due to the obstructing incorporation of Sn atoms into partially dealuminated *BEA framework containing residual Brønsted acid sites. On the other hand, the improved selectivity of Sn,Al-*BEA vs. a physical mixture of Brønsted and Lewis acid solids can be understood considering the more facile conversion of the intermediate FA to BMF over Sn- and Al-associated active sites hosting in the same framework. In contrast to Sn,Al-*BEA, polymerization of FA occurred throughout time-resolved diffusion of FA out of the crystallites of Sn-*BEA and subsequently into the crystallites of Al-*BEA in the physical mixture. Noticeably, full dealumination of *BEA zeolite followed by simultaneous incorporation of Sn and Al atoms via solid-state ion exchange produced a bifunctional Sn,Al-*BEA catalyst containing exclusively tetrahedrally coordinated metal sites. As a result, Sn,Al-*BEA showed not only high selectivity to BMF (75%), but also superior activity (TOF = 0.18 min^{-1}).[149]

Recently, bifunctional *BEA zeolites containing both Al-associated Brønsted acid sites and Lewis acid centres of different nature were intensively investigated as catalysts for the integrated one-pot reduction and acid-catalyzed non-selective conversion of furfural to useful bio-products.[203-205]

The incorporation of metal species in neutral (i.e. all-silica) or acidic (i.e. isomorphously substituted) zeolites enables to significantly expand the set of reactions that can be efficiently catalyzed by zeolite-based catalysts. Besides the acidic and porous characteristics of zeolites discussed beforehand, the nature, size, and location of the metal species as well as possible synergic effects that may develop due to the presence of both metal and acid sites in close proximity are key factors determining the catalytic performance of metal-zeolite composite materials. The recent advances for tailoring active sites in metal-zeolite catalysts and their main features in industrially relevant and emerging catalytic applications are discussed in the next sections.

3. Tailoring active sites in metal-zeolite composites

Heterogeneous catalysts based on supported metal species are widely employed in a large number of industrial chemical processes including refining, petrochemistry, organic synthesis, pollution control and abatement, and energy production. Supported metal catalysts may present metal species of different size, increasing from single metal atoms to clusters (ensembles of atoms with sizes below 1 – 2 nm) and to nanoparticles (1 – 100 nm). The size of the metal species in supported metal catalysts is, in fact, one of the most critical factors determining their ultimate performance in catalysis. Generally, a reduction in size of metal species entails an increase in their intrinsic reactivity owing, among other factors, to the higher unsaturation of the metal sites in smaller metal entities. Moreover, due to quantum size effects, subtle changes in the number of atoms or in their specific atomic configuration can reset the energy scale of the small metal clusters leading to significant changes in their physicochemical properties (e.g. electron affinity) and, consequently, in their chemical reactivity. This has been nicely demonstrated for gold, a relatively inert element, whose catalytic activity drastically increases when decreasing the size of the gold species to the subnanometer range.[206, 207] However, since the surface free energy of the metal species increases with decreasing their size, smaller metal entities (i.e. single atoms and small metal clusters) exhibit a higher tendency to agglomerate during thermal activation and/or catalysis, impairing their overall catalytic performance. Therefore, a major current challenge in catalysis by supported metals engendering extensive research is the preparation and stabilization of single metal atoms and small metal clusters through threir confinement inside the channels and cages of zeolites. On the other hand, at high metal loadings, metal nanoparticles (with sizes typically exceeding the diameter of micropores) are generally poorly dispersed on conventional (mostly microporous) 3D zeolites exhibiting low external surface areas. In this respect, the use of 2D (i.e. layered), nanocrystalline, and mesoporous (hierarchical) zeolites appear more suitable for dispersing metal nanoparticles on their large and accessible surfaces, especially when applying traditional impregnation or precipitation-deposition methods. Nonetheless, recent advances in the synthesis of nanomaterials have enabled the successful preparation of metal-zeolite composites in where metal nanoparticles are efficiently encapsulated within a zeolite shell in core-shell or yolk-shell structures leading to enhanced shape selectivity effects in specific reactions.

The main preparation strategies currently employed for dispersing/confining differently sized metal species in zeolites, with a special emphasis on recent synthetic approaches enabling the stabilization of single metal atoms and small metal clusters in zeolite voids, are first discussed in Section 3.1. Then, the dynamic behaviour of metal species under reactive environments is highlighted in Section 3.2, where the application of recently developed advanced spectroscopic and imaging methods with enhanced resolution, ideally under *operando* conditions, is certainly contributing to the establishment of more solid structure-performance correlations in *working* catalysts as an essential step towards the tailored design of more efficient catalytic materials. Finally, the catalytic performance of metal-zeolite composites in industrially important and emerging catalytic applications will be illustrated in Section 3.3 through representative examples. Future perspectives in this exciting field of research will be highlighted at the end of the review. We expect that the compiled information will help in stimulating further research that may facilitate the fundamental understanding and applicability of these outstanding catalytic materials.

3.1. Synthesis approaches for preparing metal-zeolite composites

3.1.1. Conventional methods for supporting metal nanoparticles in zeolites

Controlling the size and shape of the supported metal nanoparticles is of paramount importance for preparing catalysts with tailored active sites displaying improved activity, selectivity, and stability. This can be achieved to different extents depending on the particular methodology and conditions employed in their preparation.[208-210] The main approaches employed to support/confine metal species in zeolites are described in this section.

3.1.1.1. Impregnation

Impregnation followed by drying and thermal treatment (calcination, reduction) is a widely applied method for preparing industrial supported metal catalysts due to its simplicity, scalability, and low amount of wastes, particularly when using water as solvent. Therefore, it has also been extensively employed to disperse metal nanoparticles, especially at high loadings, in zeolites.

The nature of both metal precursor and solvent, the solution pH during impregnation, and the conditions of the subsequent thermal treatments (drying, calcination and, if required, reduction) are the most critical factors determining the ultimate metal dispersion in impregnated catalysts.[210] In general, improved metal dispersions are achieved upon adjustment of the pH during impregnation with aqueous solutions in order to promote the electrostatic interaction between the solvated metal ions and the anchoring surface -OH groups of the zeolite host. The calcination conditions and the heating rate are decisive parameters influencing the size and size distribution of the resulting metal oxide particles. Thus, better metal dispersions at high loadings can been attained by performing the calcination under a flow of NO diluted (0.1 – 2 vol%) in an inert gas (N_2, Ar, He) instead of air[210-212], and by using low heating rates. For instance, calcination of Pt/Y catalysts, prepared by impregnation with $Pt(NH_3)_4^+$ precursor, using a heating rate as low as 0.2 °C/min resulted in uniformly dispersed small Pt particles sizing less than 1.1 nm (i.e. comprised of 13 – 20 atoms according to EXAFS data), while the application of a commonly used heating rate of 1 °C/min lead to larger particles with a bimodal particle size distribution.[213] The need for using such extremely low heating rates is accounted for by the slow diffusion of water and ammonia from the micropores in combination with the stabilization of mobile Pt species by the zeolitic walls. Addition of multidentate chelating agents (i.e. citric acid, ethylenediaminetetraacetic acid, and nitrotriacetic acid) to the impregnating solution may also be applied to promote the homogeneous distribution and dispersion of the metal oxidic phase after calcination.[214] Even though generation of metal nanoparticles by impregnation offers poor control over the final particle size, generally leading to a broad particle size distribution with a large fraction of the nanoparticles located on the external zeolite surface, some small nanoparticles confined in the zeolite micropores may also be formed.

3.1.1.2. Deposition-precipitation

Deposition-precipitation involves the controlled precipitation (generally induced by a change of pH, temperature, or evaporation) of metal compounds (often metal hydroxides) onto the support from a solution containing the metal precursor.[210] The pH of the precursor solution during deposition is one of the most important factors influencing the size and amount of deposited metal nanoparticles as it largely determines the charge of the support surface and, hence, the metal precursor-support electrostatic interaction strength, as discussed before for impregnation. The precipitation-deposition approach has been widely applied, for instance, to prepare zeolite-supported gold catalysts with high dispersion. As it occurs for other support materials, the pH of the solution during the deposition of gold not only controls the zeolite surface charge but also the extent of hydrolysis of the $AuCl_4^-$ precursor and, consequently, the nature of the precursor-zeolite interaction. Behravesh et al.[215] performed a systematic investigation of the effect of the solution pH (adjusted by adding an NH_4OH solution as precipitating agent) on the final particle size and size distribution, and loading efficiency for Au deposited on HY zeolite (Si/Al ratio of 40) and their consequences on the activity for the gas phase oxidation of ethanol. In the investigated pH range of 6.5 – 10.5, the surface of the HY zeolite was found to be negatively charged, preventing an efficient electrostatic interaction of the $[AuCl_n(OH)_{4-n}]^-$ anions with the zeolite surface. Nonetheless, the average size of Au nanoparticles decreased from 13.2 to 5.8 nm upon raising the pH from 6.5 to 8.5 as, at the later pH, the zeolite displayed the lowest negatively charged surface. In another study, it was shown that the surface charge of HY zeolite (Si/Al ratio ~ 2.8) could be reversed from negative to positive by treating the zeolite with Na^+ solutions (to form H(Na)-Y) prior deposition of Au species from $HAuCl_3 \cdot 3H_2O$ precursor at constant pH of 6.[216] The so generated positive surface charge favoured the electrostatic interaction between the anionic Au species and the zeolite surface, resulting in ultrasmall gold nanoparticles of ~1 nm confined in the supercages of the

FAU-type zeolite that exhibited a much higher reactivity for CO oxidation compared to Au nanoparticles deposited on untreated HY.[216]

3.1.1.3. Colloidal methods

Compared to conventional impregnation and precipitation-deposition methods, the colloidal synthesis of metal nanoparticles enables a much better control over the size, shape, and composition of the supported metal phases at the atomic level.[217-219] Microemulsion systems, and particularly water-in-oil (w/o) or reverse microemulsions employing cationic (e.g. cetyltrimethyl ammonium bromide), anionic (e.g. Aerosol OT), or non-ionic (e.g. pentaethylenglycol dodecyl ether) surfactants, are among the most widely employed colloidal methods to synthesize size-controlled metal nanoparticles.[219-222] The inner core of the water droplets containing the metal precursor in w/o microemulsions can be considered as a nanoreactor where the synthesis of nanoparticles takes place. Once a suitable microemulsion containing the metal precursor is obtained, a precipitating agent (most often hydrazine, or sodium borohydride) is added, usually as a second microemulsion, to generate the metallic nanoparticles. Finally, the metal nanoparticles formed in the aqueous core of the micelles need to be efficiently transferred onto the support. This is usually accomplished by destabilizing the microemulsion, for instance by adding tetrahydrofuran or by increasing the temperature to the required extent (depending on microemulsion composition) to break the water droplets and, thus, to release the metal nanoparticles (thermo-destabilization).[223] However, during the transferring process inhomogeneous distributions of the nanoparticles on the support and particle agglomeration during the subsequent thermal treatments may occur with a negative impact on the final metal dispersion. This can be minimized by promoting a stronger electrostatic interaction between the nanoparticles and the support surface, which depends on the respective zeta potentials.[224]

An additional advantage of microemulsion methods against conventional impregnation and deposition-precipitation is that the size of the metal nanoparticles can be, in principle, varied independently of metal loading. For instance, Pt nanoparticles within the narrow size range of 4.8 – 5.9 nm were obtained upon deposition of Pt nanoparticles, previously synthesized using w/o microemulsions, onto a *BEA zeolite regardless the Pt loading (0.02 – 0.18 wt%). Conversely, the nanoparticle size gradually increased from 1.7 to 13.1 nm with increasing the loading from 0.01 to 0.2 wt% in equivalent impregnated Pt/*BEA catalysts.[225]

Nevertheless, owing to the large size of the micelles involved in colloidal syntheses, their deposition onto conventional 3D zeolites may limit the maximum amount of metal that can be efficiently dispersed without excessive aggregation. Much easier control over the size of the nanoparticles at high metal loadings may be achieved by depositing the micelle-derived nanoparticles on 2D zeolites (e.g. delaminated ITQ-2) presenting much higher external surface areas. By taking advantage of the unique textural characteristics of 2D zeolites and the control of nanoparticle size allowed by microemulsion methods, a series of Co/ITQ-2 samples (10 wt% Co) comprising cobalt nanoparticles with sizes ranging from 5 to 11 nm was prepared and used as model catalysts to address cobalt particle size effects in Fischer-Tropsch synthesis.[226, 227] The synthesis of the Co/ITQ-2 catalysts is schematically represented in Figure 15.[226] In short, size-controlled cobalt nanoparticles synthesized in reverse microemulsions are deposited on the surface of an all-silica ITQ-2 zeolite previously silylated to avoid the formation of hard-to-reduce mixed Co-Si compounds by reaction of the Co^{2+} ions in the nanoparticle precursors with the (abundant) OH groups present on the ITQ-2 surface.

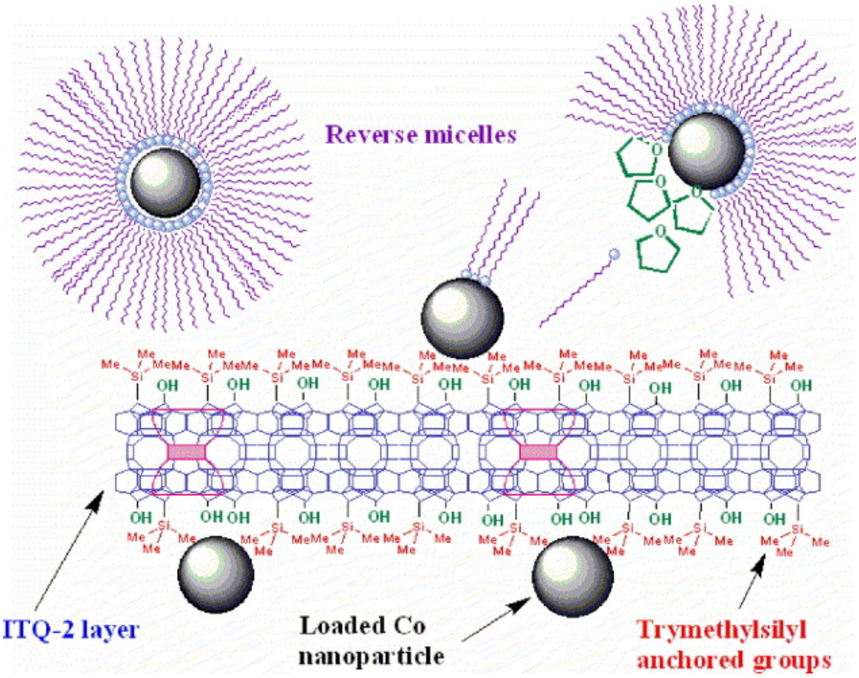

Figure 15. Schematic representation of the preparation of model Co/ITQ-2 catalysts comprising the deposition of size-controlled cobalt nanoparticles produced ex-situ by w/o microemulsion on an all-silica delaminated ITQ-2 zeolite whose external surface is previously silylated to avoid the formation of inactive Co silicate phases. Adapted from ref. [226]

3.1.2. Synthetic approaches for encapsulation of metal species in zeolites

Different preparation methodologies have been conceived to effectively encapsulate metal clusters and nanoparticles in zeolites. These methods can be divided into two broad groups: i) direct or one-pot synthesis methods, in which the metal species are formed in situ or added during zeolite crystallization, and ii) post-synthesis approaches, where the metal species are generated on a pre-existing zeolite. The most representative approaches within each group are described below.

3.1.2.1. Direct synthesis methods

Encapsulation of metal clusters and nanoparticles in the pores and cavities of zeolites can be achieved via direct hydrothermal synthesis by introducing the metal precursors during the zeolite crystallization process, where assembly of the zeolite building units occurs around the solvated metal complexes promoted by electrostatic or van der Waals interactions. This methodology has two main limitations: 1) the guest species has to survive the harsh conditions of the zeolite synthesis in terms of pH and temperature, and 2) the crystallization of the zeolite has to take place in the presence of the metal guest. In order to prevent decomposition or premature precipitation as colloidal hydroxides of the metal precursor species at the typical basic conditions of zeolite crystallization, the cationic metal precursors are usually stabilized by suitable ligands prior to their encapsulation during zeolite synthesis. For instance, Goel et al. used cationic precursors of noble metals (Pt, Pd, Ru, Rh) stabilized by ammonia or ethylene diamine ligands to encapsulate the respective metal clusters in small-pore zeolites.[228] On the other hand, the group of Iglesia reported a general approach for the encapsulation of metal clusters in zeolites during their hydrothermal crystallization using (3-mercaptopropyl)trimethoxysilane ligands.[229] The mercapto (-SH) groups of the bifunctional ligand stabilize the metal precursors while the alkoxysilane moieties undergo hydrolysis in alkaline media to form Si–O–Si or Si–O–Al covalent bonds with nucleating zeolite structures creating linkages that enforce the encapsulation. By using this approach, Pt, Pd, Ir, Rh, and Ag clusters of around 1 nm in diameter in the similarly sized (1.1 nm) α-cages of the small-pore (8-ring) zeolite NaA (LTA) were successfully encapsulated. The specific location of the metal clusters was proved by their substrate-size selectivity in the hydrogenation of alkenes and the oxidative dehydrogenation (ODH) of alkanols with different kinetic diameters.[229]

Zeolites generated from 2D layered precursors (e.g. MCM-22, Ferrierite, Sodalite, RUB-24, and RUB-36) are also well suited to the encapsulation of metal nanoparticles owing to the high accessibility of the zeolite framework upon expansion of the layers in the precursor materials. This has been recently shown in an inspiring work by Corma et al.[230] reporting the encapsulation of single metal Pt atoms and clusters with high stability in the supercages of an all-silica MCM-22 zeolite (ITQ-1) during the transformation of the 2D siliceous layered MWW-P zeolite precursor into the 3D MCM-22 zeolite (Figure 16). In this case, subnanometric Pt clusters were prepared from $Pt(acac)_2$ and dimethylformamide (DMF) acting as weak reductant and capping agent and added to an aqueous solution containing the layered MWW-P precursor, cetyltrimethylammonium hydroxide (50% exchanged Br^-/OH^-) as swelling agent, and TPAOH (30% exchanged Br^-/OH^-) and heated at 52 °C for 16 h. Then, calcination at 540 °C in N_2 for 4.5 h and subsequently in air for 4 h lead to Pt clusters encapsulated in the MCM-22 supercages. The formation of Pt clusters (with ~13 atoms in average) and isolated Pt atoms was confirmed by high-angle annular dark-field detector high-resolution scanning TEM imaging (HAADF-

HRTEM), photoluminescence spectroscopy, IR spectroscopy of CO adsorption, and EXAFS analysis. The Pt clusters exhibited exceptional high stability against reduction-oxidation treatments at temperatures of up to 650 °C, making this synthetic approach highly relevant for applying metal cluster catalysts in temperature-demanding reactions.

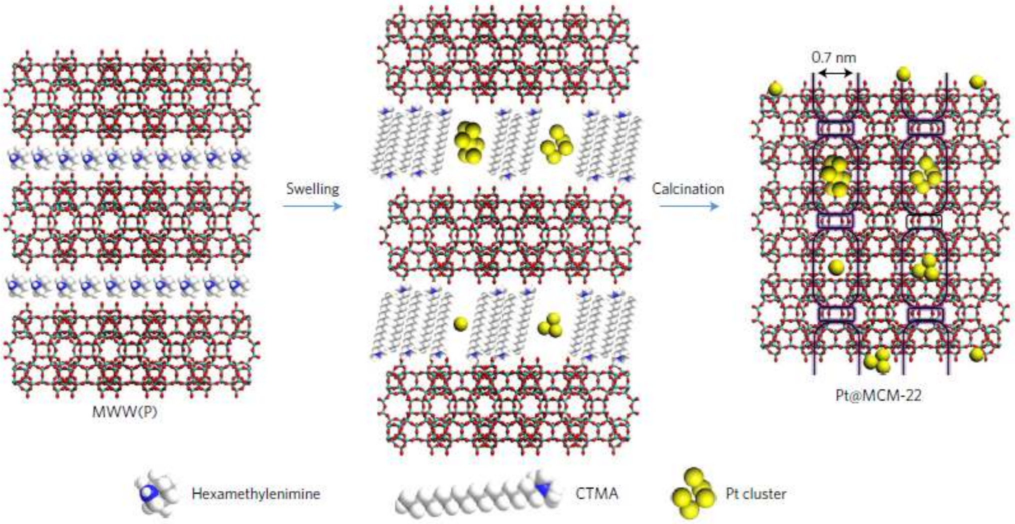

Figure 16. Illustration of the encapsulation of small Pt clusters in the large cages of zeolite MCM-22 during the transformation of the 2D MWW(P) layered precursor to the 3D MCM-22 zeolite. Adapted from ref. [230]

Using a similar approach, Zhao et al. reported a layer reassembling approach to encapsulate Pd nanoparticles (1.4 nm) in FER zeolite.[231] This strategy initially involves the swelling of the FER layers in RUB-36 zeolite with cetyltrimethylammonium cations (CTA^+) and subsequent exchange of CTA^+ with $Pd(en)_2^{2+}$ cations from diethylenediamine palladium(II) acetate precursor which, upon condensation of silanol groups between adjacent layers by calcination and final reduction, leads to metallic Pd nanoparticles embedded in the 3D FER zeolite. The so-prepared Pd@FER catalysts showed outstanding shape selectivity in the hydrogenation of C=C and C=O bonds in olefins and aromatic aldehydes/ketones, respectively.[231]

Encapsulation of metal nanoparticles in mesoporous and nanosized zeolites would combine the benefits of a high accessibility to the surface metal sites with the shape selectivity inherent to the still existing microporous network. Following this idea, Gu et al. developed a facile synthetic route to encapsulate metallic nanoparticles (exemplified for Pt) within mesoporous MFI crystals.[232] The synthetic strategy comprises, as the first step, the preparation of a hierarchical micro-mesoporous ZSM-5 zeolite by alkali treatment (alk-ZSM-5) and subsequent impregnation of alk-ZSM-5 with an aqueous solution containing the required amount of Pt precursor ($H_2PtCl_6 \cdot 6H_2O$) to achieve 2 wt% metal loading in the final catalyst. As the last step, the Pt/alk-ZSM-5 hybrid precursor is covered with a gel of composition similar to silicalite-1 and recrystallized via the dry gel conversion method to produce the Pt@MFI composite. The encapsulated Pt nanoparticles display high thermal stability and do not aggregate after their use as catalyst for CO oxidation at 600 °C. In a similar way, Cui et al. reported a relatively simple one-pot methodology for the simultaneous encapsulation of Pd nanoparticles and the generation of controlled mesopores in silicalite-1 nanocrystals starting from silica nanoparticles and chloropalladic acid (H_2PdCl_4) as metal precursor.[233] The silica nanoparticles were added to an aqueous solution containing the Pd precursor mixed with a small amount of polyvinylpyrrolidine (PVP), the pH was adjusted to 12 by adding the required amount of NaOH solution and the dispersion stirred, dried, and transferred to a Teflon-lined autoclave for zeolite crystallization at 120 °C for 48 h in the presence of TPAOH. After crystallization, the material is calcined in air at 550 °C and then reduced in H_2/Ar flow at 300 °C. The high accessibility of the mesopore-confined metal nanoparticles and the presence of inherent micropores endowed the produced Pd@meso-S-1 hybrids with shape selectivity in a variety of chemical transformations, including selective hydrogenation, oxidation, and carbon-carbon coupling reactions.[233] The synthesis of mesoporous Pd@S-1 composites was also achieved by first incorporating -NH_2 groups (the anchoring points for the Pd^{2+} cations in the metal precursor) on the surface of silicatite-1 via functionalization with 3-aminopropyltrimethoxysilane (APTMS), and then by submitting the composite to an etching process with TPAOH to create internal mesopores and to promote re-crystallization of dissolved silica species on the outer surface upon the hydrothermal treatment.[234] Finally, a sodium formate solution was utilized to reduce the Pd^{2+} ions to metallic Pd nanoparticles.

Encapsulation can also be accomplished by performing the zeolite crystallization in the presence of pre-synthesized metal nanoparticles. For instance, Laursen et al. reported a synthetic approach for embedding small metal nanoparticles in zeolites involving the following three steps: 1) synthesis of a colloidal suspension of metal nanoparticles with suitable anchor points for the generation of a silica shell, 2) encapsulation of the nanoparticles in an amorphous silica matrix, and 3) submitting the nanoparticle-silica precursor to hydrothermal conditions to promote zeolite crystallization.[235] Using this strategy, the authors successfully prepared materials comprising small (1 – 2 nm) gold nanoparticles embedded in silicalite-1 crystals that are only accessible through the zeolite micropores and which exhibit significant substrate-size selectivity in the aerobic oxidation of a mixture of benzaldehyde and bulkier 3,5-di-*tert*-butylbenzaldehyde.[235] On the other hand, Zhang et al. reported a seed-directed route to prepare Pd@*BEA catalysts with a core-shell structure, in which Pd nanoparticles larger than the pore diameter of the *BEA zeolite are first supported on zeolite crystals that function as seeds for growing the zeolite crystals during hydrothermal synthesis.[236] In another study, Wang et al. applied a solvent-free crystallization approach to prepare core-shell Pd@S-1 catalysts using PVP-stabilized Pd nanoparticles.[237] In this approach, the PVP-stabilized nanoparticles were mixed with TEOS, ethanol, and ammonium hydroxide at room temperature for 8 h under stirring resulting in the intermediate Pd@SiO_2 composite, where Pd is encapsulated within an amorphous SiO_2 shell. Then, the Pd@SiO_2 material is grinded with TPAOH at 25 °C for 10 min, heated at 70 °C for 10 min, and thermally treated in an autoclave at 180 °C for 3 h. The final Pd@S-1 catalyst is obtained upon calcination at 550 °C for 4 h.

3.1.2.2. Post-synthesis methods

Grafting

Grafting involves the reaction of organometallic precursors with the surface OH groups of the support and has been widely applied for covalent immobilization of organometallic complexes in the preparation of supported single-atom metal catalysts.[238, 239] One of the most representative example is the synthesis of Ti-containing mesoporous materials and zeolites by grafting a titanocene precursor on their surfaces. As an example, the synthesis of the 2D Ti-ITQ-2 zeolite containing isolated Ti sites upon grafting with the titanocene $Ti(Cp)_2Cl_2$ precursor is presented in Figure 17.[240] Characterization of the grafted material by UV-Vis and XANES spectroscopies confirmed the presence of monomeric Ti species in the calcined Ti/ITQ-2 material. Grafted Ti-ITQ-2 catalysts exhibited high activity and selectivity (typically above 95%) in the epoxidation of olefins under mild conditions (60 °C) using organic hydroperoxides (e.g. *tert*-butyl hydroperoxide) as oxidants.

Interestingly, the selectivity to the target epoxide product could be increased even further (≥ 99%) upon tuning the adsorption properties of the Ti/ITQ-2 catalysts by silylation, so that undesired opening of the epoxide ring to the corresponding polar diols (catalyzed even by weakly acidic silanols) is substantially suppressed on the more hydrophobic silylated surface.[240]

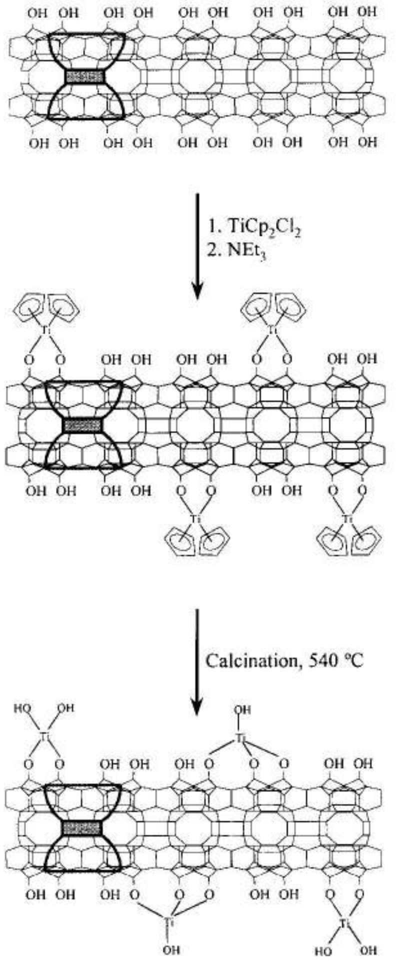

Figure 17. Schematic representation of the preparation of Ti/ITQ-2 catalysts by grafting using titanocene ($Ti(Cp)_2Cl_2$) as Ti precursor. Adapted from ref. [240]

Metal ion exchange followed by thermal treatment

Small metal clusters and nanoparticles can be encapsulated in zeolites containing T^{3+} framework heteroatoms (e.g. Al, B, Ga) by exchanging the charge-compensating cations with cationic metal precursors followed by a thermal treatment. The nature of the final metal species, however, depends on many variables, such as the nature and crystallographic position of the zeolite counter-cations, the presence of hydroxyl groups, residual water, and ammonium cations, etc., which makes this method of encapsulation not easily reproducible.

After the ion exchange process, the material is thermally treated under reducing or oxidizing atmospheres, depending on whether metallic or oxidic metal phases are targeted, at suitable temperatures, with higher temperatures promoting the aggregation of metal clusters into nanoparticles. In the case of noble metals, metallic clusters and nanoparticles may be generated by direct reduction of the corresponding ion-exchanged species with hydrogen. For instance, extremely small Pt clusters with an average Pt coordination number of 3.7 (i.e. ~ 5 – 6 atoms in the cluster) confined inside the pores of Ba-LTL zeolite were generated by direct reduction of Pt/Ba-LTL (1.2 wt% Pt) at 500 °C.[241] Nonetheless, formation of mobile metal species at such high temperatures and the presence of ammonia evolving from cationic metal precursors containing NH_3 ligands (e.g. $Pt(NH_3)_4^{2+}$) often promotes metal agglomeration during the direct reduction treatment with H_2. In contrast, markedly improved metal dispersions are achieved when the $Pt(NH_3)_4^{2+}$ precursor in the ion-exchanged zeolite is decomposed or calcined prior to reduction, where the calcination conditions (temperature, heating rate) are critical in determining the final dispersion.[213] In this respect, Pt clusters (comprising about 6 atoms) highly dispersed in the pores of HMOR were produced upon ion exchange with $Pt(NH_3)_4(OH)_2$ followed by calcination in air at 350 °C and subsequent reduction in H_2 at 350 °C.[242] In another study, very small (< 1 nm) Pt clusters encapsulated in zeolite K-LTL were obtained from $Pt(NH_3)_4(NO_3)_2$ by calcination at 260 °C and reduction in H_2 at 500 °C.[243] It should be noted that the reasons why different optimum post-treatment conditions are required to generate the metal clusters depending on the specific metal precursor and zeolite are yet to be clarified.

Ag-zeolites are promising catalysts for selective oxidation reactions with O_2 at low temperatures, such as the selective catalytic oxidation of ammonia (NH_3-SCO)[244] and light olefins (e.g. ethylene),[245] and in the selective reduction of NO with hydrocarbons (HC-SCR).[246-248] Therefore, much attention has been paid to the investigation of the reduction behaviour of silver cations and the chemistry of silver species in zeolites. It has been shown that small silver clusters ($Ag_n^{\delta+}$, $2<n<8$) can be easily synthesized within the zeolites pores by reduction of Ag-exchanged zeolites.[249] Thus, small Ag_4^{2+} clusters were identified in Ag-MFI zeolite after H_2-assisted reduction at 300 °C by *in situ* EXAFS, UV-Vis, and IR spectroscopies. Reduction at higher temperatures resulted in the aggregation of the Ag_4^{2+} cluster and consequent formation of larger Ag clusters and nanoparticles.[249] Notably, a dynamic reversible behaviour of the silver species, by which Ag clusters re-dispersed to Ag^+ ions under oxidizing conditions, was observed in Ag-MFI zeolite using time-resolved *in situ* UV-Vis and Quick XAS spectroscopies.[249] The extent of cluster-ion interconversion exhibited a sharp dependence on the type of oxidant (e.g. NO, O_2, NO+O_2) and temperature,[249] making it possible to tune the relative concentration of each type of metal species (and, thus, the catalytic performance) in a given zeolite by simply adjusting the conditions of the post-treatment. The dynamic behaviour of metal species in metal-zeolite catalysts will be specifically addressed in Section 3.2.

Metal oxo clusters can also be stabilized in zeolites by calcination of ion-exchanged metal-zeolites. Based on this, several studies focused their interest on the formation of mono-μ-oxo-dinuclear or tri-nuclear metal complexes of different metals like Cu,[250-252] Ni,[253] Fe,[254-256] Ga,[257] and Zn[258] that mimic the active sites of enzymes.[259, 260.] The nature of the formed metal oxo clusters is influenced by several parameters, including the zeolite topology, the number and position of framework aluminum atoms, the nature of the metal precursor and solution pH, and the final calcination conditions (temperature, gas flow, heating rate, and type of oxidant).[252] Thus, single site tri-nuclear copper oxygen clusters $[Cu_3(\mu\text{-}O)_3]^{2+}$ were successfully formed in MOR after ion exchange with a Cu-acetate precursor and calcination in flowing O_2 at 450 °C. The DFT-predicted structure and location of the Cu oxo cluster in MOR zeolite is shown in Figure 18. As seen there, the specific framework topology of MOR allows the preferential ion exchange of the sites located in the more constrained side pockets where the $[Cu_3(\mu\text{-}O)_3]^{2+}$ cluster is stabilized upon migration of the exchanged Cu ions during the calcination treatment.[251]

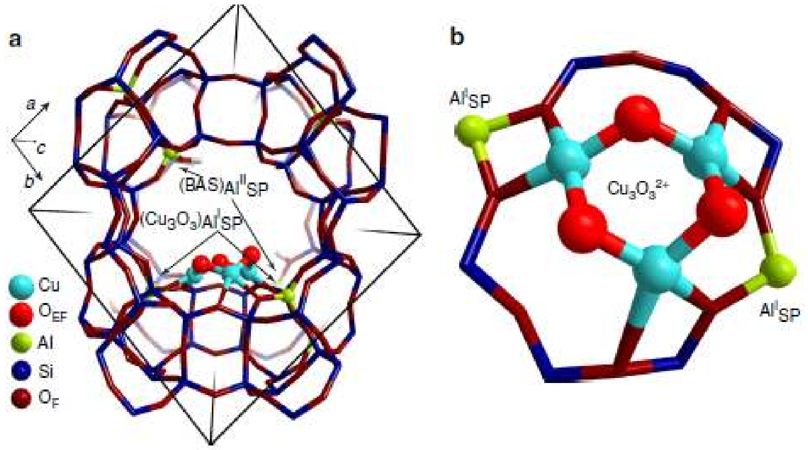

Figure 18. Structure and location of the $[Cu_3(\mu\text{-}O)_3]^{2+}$ cluster in MOR zeolite as predicted by DFT calculations. Adapted from ref. [251]

Metal nanoparticles can also be produced by thermal treatment of ion-exchanged T^{3+}-zeolites at temperatures higher than those applied to generate metal clusters. In this case, the maximum amount of metal that can be introduced by this method is limited by the concentration of framework T^{3+} atoms in the starting zeolite and, hence, Al-rich FAU-type zeolites (NaX, NaY) are more suitable to introduce relatively higher amounts of metal species.

Ship-in-bottle synthesis

This method involves the *in situ* formation of metal species inside the zeolite micropores by adsorbing suitable metal precursors that react and transform into the final metal guest species in the confined space provided by the intrazeolitic voids acting as nanoreactors.[261, 262]

A common ship-in-bottle approach for encapsulation of metal clusters in zeolites comprise successive carbonylation reactions[263-265] (with $CO+H_2$ or $CO+H_2O$) starting from: i) mononuclear metal complexes acting as building blocks, ii) metal ions introduced by ion-exchange, or iii) volatile subcarbonyls incorporated into the zeolite pores by a solid-state reaction. As an example, $Rh_6(CO)_{16}$ metal clusters encapsulated in the cages of zeolite NaY were prepared by submitting the ion exchanged zeolite to successive carbonylation with $CO+H_2$ at 20 – 200 °C to form the mononuclear dicarbonyl $Rh(CO)_2(\text{-O-})_2$ species that migrate through the zeolite channels and are converted into $Rh_4(CO)_{12}$ and $Rh_6(CO)_{16}$ clusters after subsequent cluster-oligomerization.[266] Spectroscopic characterization of the final material by IR and EXAFS confirmed the stoichiometry of the formed clusters.

Compared to the relatively voluminous metal-carbonyl complexes, smaller metal complex precursors involving ligands like C_2H_4 prepared by ship-in-bottle can better accommodate within the channels and cavities of most 3D zeolites. Irrespective of the ligand, the bare metal cluster is generated upon ligand removal by thermal treatment of the metal guest complex under mild reducing and/or oxidizing conditions. In some cases, however, this procedure may yield unpredictable results as the stoichiometry and structure of the formed cluster often depends on the nature of the metal, the metal ligands, and the support host. For example, $Ir(C_2H_4)_2$ complexes are converted into Ir_4 clusters in H_2 at 80 °C on HY zeolite,[267] while the use of $Rh(C_2H_4)_2$ leads to a mixture of small Rh_{2-4} clusters on HY[268] but neatly generates Rh_2 clusters on MgO.[269] Interestingly, it was possible to stabilize either the mononuclear $Ir(C_2H_4)_2$ and $Rh(C_2H_4)_2$ complexes or the metal Ir_4 and Rh_2 clusters in the supercages of HY by simply tuning the H_2/C_2H_4 ratio in the reactive gas mixture (see further discussion in Section 3.2).[267, 268, 270]

Other methods

Atomic layer deposition (ALD) is a vapor phase method widely applied to deposit thin films of inorganic materials on substrates with a precise control of film thickness in the subnanometer range. ALD involves the self-limiting reaction between two or more gaseous precursors taking place sequentially in a cyclic manner. A typical ALD cycle consists of alternate pulses of gaseous precursors with intermediate purge or pump steps so that the precursors react individually with the surface functional groups of the substrate avoiding undesired gas phase reactions. Due to the fine thickness control and uniformity of the deposited films, ALD has emerged as a powerful technique to synthesize atomically designed nanocatalysts with improved catalytic performance in different chemical transformations.[271-273] An additional advantage of the ALD technique with respect to the most commonly employed liquid phase methods (e.g. impregnation) is the absence of solvents and wastewaters. More recently, ALD has also been applied to confine metal species in porous materials, including zeolites.[274] However, the limitations to the diffusion of reactants imposed by the zeolite micropores makes the uniform deposition of metal species into the zeolite pores by ALD a challenging task. Nonetheless, in a recent work Xu et al. successfully deposited Pt nanoclusters of controlled size (0.8 nm) inside the pores of zeolite KL by the ALD method using methylcyclopentadienyl trimethylplatinum ($MeCpPtMe_3$) as metal precursor.[275] Characterization of the material by N_2 physisorption and IR-CO spectroscopy in combination with DFT calculations indicated that most of Pt was confined inside the zeolite channels in a highly dispersed state, and only a small fraction of the deposited Pt species resided at the pore openings or on the external surface. Due to the confinement effect, the Pt nanoclusters were electron-enriched and did not aggregate into larger species. The ALD-derived Pt/KL catalyst displayed high selectivity to toluene (67.3%), low methane selectivity (0.9%), and high stability in the *n*-heptane reforming reaction.

Another interesting approach is the electrochemical synthesis of metal nanoparticles and/or clusters. The electrochemical generation of metal clusters is based on the reduction of metal cations, originating from the anodic dissolution of an electrode of the same metal, on the surface of the cathode. The electrolyte acts as solvent and, in the case of using ammonium salts (e.g. $R_4N^+Y^-$), as a cluster stabilizer. An advantageous aspect of the electrochemical synthesis against most chemical syntheses routes is the possibility to control the size (i.e. atomicity) of the cluster by adjusting the current density.[276, 277] Moreover, the formed clusters (which precipitate out of the solution) can be easily isolated and re-dispersed in a suitable solvent (e.g. water, acetonitrile) where they can remain stable up to several months. As a major drawback, the yields achieved are low and further optimization of the methodology is required for practical applications. Although originally developed for the synthesis of metal nanoparticles of different shapes and sizes and more recently extended by Quintela et al.[277] for synthesizing size-controlled small clusters of different metals such as copper (Cu_n, $2< n < 20$, e.g. Cu_5, Cu_{13}, Cu_{20})[277, 278], silver (Ag_5 and Ag_6),[279] and gold (Au_3, Au_{5-7}, Au_{7-10})[280], no studies reporting the encapsulation of metal clusters in zeolites by this method have been reported up to date. Nonetheless, we believe this methodology might represent a promising approach to confine metal clusters with tailored atomicity in zeolites if the synthesis yields are significantly improved.

3.2. Dynamic behaviour of metal species in *working* metal-zeolite catalysts

An important aspect deserving special mention here is the dynamic evolution that metal species can experience under certain reactive environments. In that respect, Moliner et al.[281] described the oxidative fragmentation of small Pt nanoparticles of ~1 nm into single atoms in Pt-[Al]CHA (Si/Al= 8.5, 0.2 wt% Pt) zeolite employing *operando* XAS spectroscopy and aberration-corrected HAADF-STEM imaging. Temperature-resolved EXAFS studies at increasing temperatures up to 500 °C under diluted (20%) O_2 flow showed a gradual decrease in the Pt-Pt coordination number from ~7 to ~5, ~4, and ~0 at 100 °C, 200 °C, and 500 °C, respectively. This was accompanied by a progressive increase of the Pt-O coordination number from ~0 to ~1.1 (at 100 °C), ~1.6 (at 200 °C), and ~3 (at 500 °C), the later corresponding to a single Pt atom (Figure 19a). The re-dispersion of Pt nanoparticles in O_2 at 500 °C was confirmed by HAADF-STEM (Figure 19b), which additionally showed that the smallest Pt nanoparticles (0.8 – 1 nm) re-dispersed easier than the largest ones (1 – 1.5 nm). The formed isolated Pt atoms transformed again into Pt nanoparticles (remaining stable even at 650 °C) upon subsequent reduction of the sample in H_2 at 400 °C, as demonstrated by both EXAFS and STEM.

a)

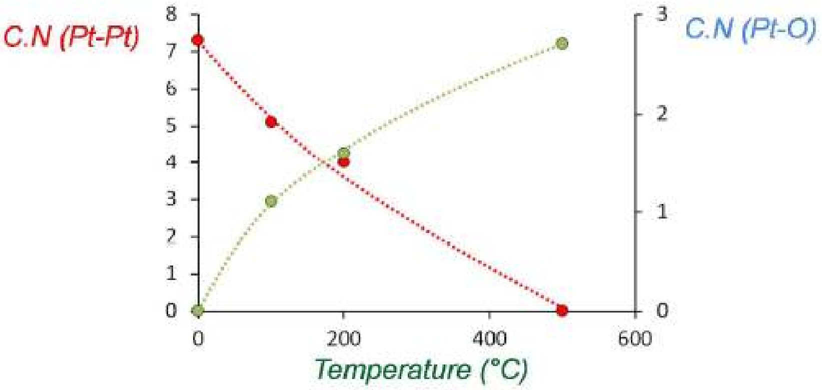

b)

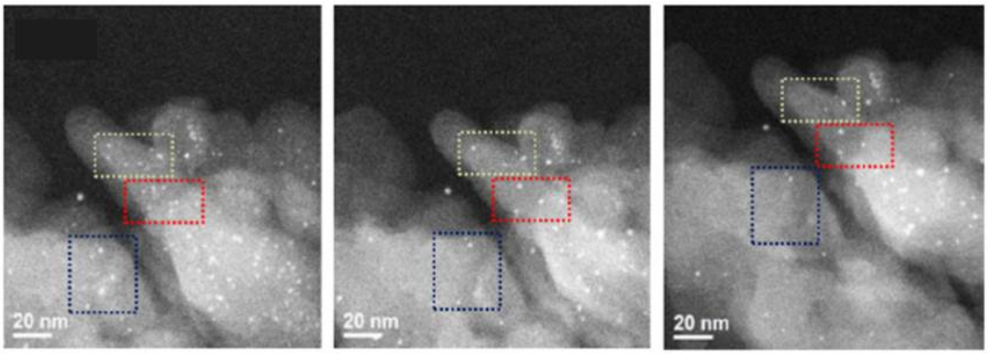

Figure 19. a) Evolution of the EXAFS-derived Pt-Pt and Pt-O coordination numbers (CN) upon treating Pt-CHA in flowing O_2 at increasing temperatures up to 500°C. b) Aberration-corrected HAADF-STEM images after submitting the H_2-reduced Pt-CHA sample to O_2 treatment at 500°C for 0 min (left), 10 min (middle), and 20 min (right). Adapted from ref. [281]

The reversible transformation of metal nanoparticles into clusters and/or single atoms was reported to occur also in Al-free zeolites lacking acid sites. Thus, by using aberration-corrected HRSTEM, Corma et al.[282] evidenced how Pt clusters in an all-silica MCM-22 zeolite disintegrate into atomically dispersed Pt atoms in O_2 under mild conditions, while they rearrange again into clusters in the presence of H_2. The fact that this process takes place even in absence of acid sites was ascribed to the stabilization effect induced by the large MCM-22 cages. It was also shown that Pt nanoparticles located on the external surface of the MCM-22 zeolite require treatments at higher temperatures to achieve re-dispersion. Going a step forward, these authors observed a general trend by which subnanometric Pt clusters disintegrate into atomically dispersed Pt atoms under flowing $NO+H_2$ or NO+CO gas mixtures at low temperatures (200 – 400 °C), while at high temperatures (600 – 800 °C) the highly dispersed Pt species agglomerate again into Pt clusters or nanoparticles (sizing 1 – 2 nm) that remain stable even at 800 °C (Figure 20a). Conversely, atomically dispersed Pt species agglomerated into Pt clusters under $CO+O_2$ and $CO+H_2O$ gas atmospheres at low temperatures (100 – 300 °C), while the reverse effect occurred at higher temperatures (Figure 20b).

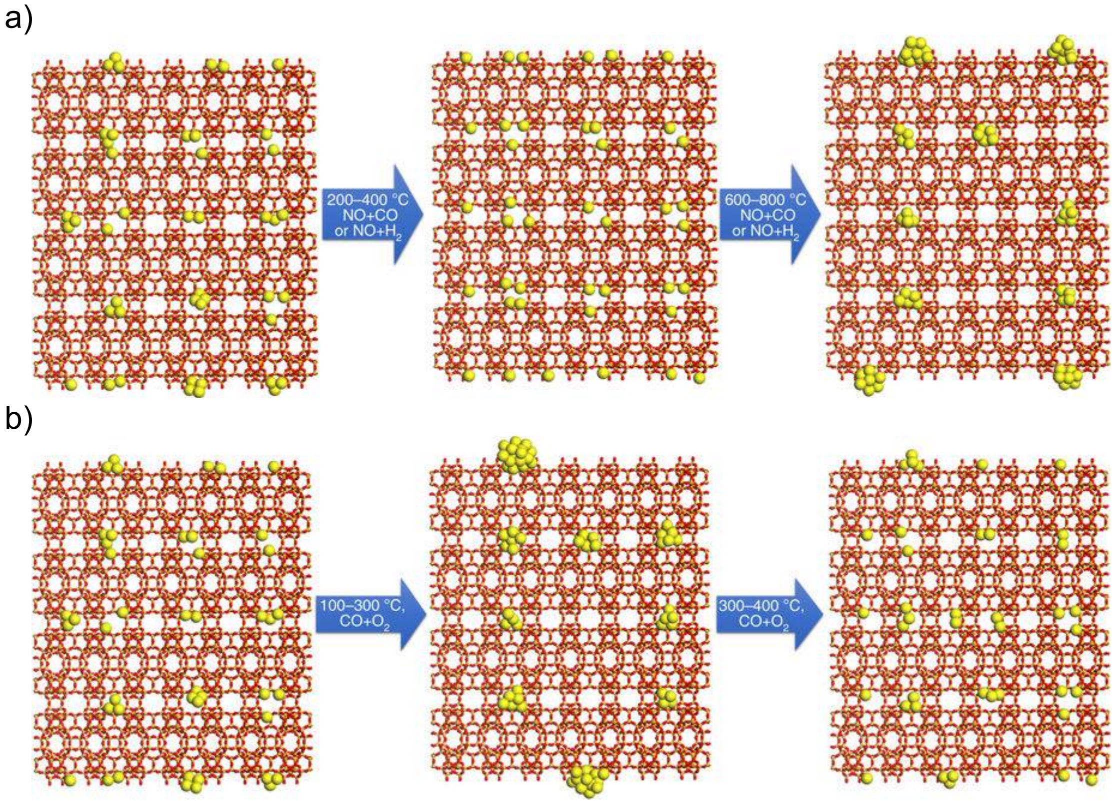

Figure 20. Schematic illustration of the structural evolution of Pt species in Pt@MCM-22 (0.17 wt% Pt) under CO+NO and NO+H_2 (a) and CO+O_2 (b) environments at increasing temperatures. Adapted from ref. [281]

The dynamic structural modifications experienced by zeolite-confined small metal clusters under certain reaction conditions may have a dramatic impact on their ultimate catalytic behaviour. As an example, the dynamic interconversion between mononuclear Rh species and di-nuclear Rh_2 clusters in HY zeolite depending on feed composition (ethylene + H_2) determined the product selectivity in the hydrogenation of ethylene.[268] Thus, under ethylene-rich conditions, the mononuclear Rh complex is stabilized in the HY pores and ethylene dimerization preferentially occurs leading to butene as the major product. Conversely, small Rh_2 clusters stabilized under H_2-rich conditions selectively catalyze the hydrogenation of ethylene to ethane, as shown in the cyclic experiments presented in Figure 21.[264,268] This dynamic interconversion of the Rh species was monitored by *in situ* EXAFS, as shown in the bottom panel of Figure 21.

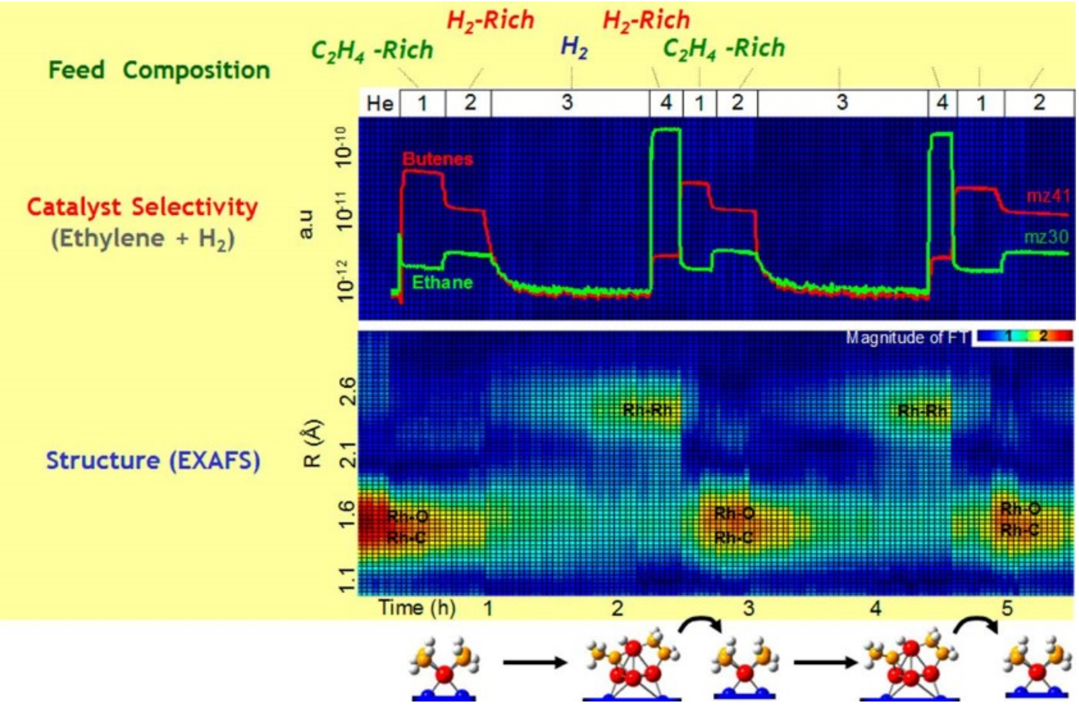

Figure 21. Changes in the selectivity and in the structure of the active sites (analysed by EXAFS) by changing the feed composition (ethylene + H_2) cyclically on a catalyst containing initially the mononuclear $Rh(C_2H_4)_2$ complex stabilized in HY zeolite. In the bottom panel, the Rh-backscatterer distance is shown as a function of time.[264,268]

Copper-containing small pore molecular sieves with chabazite (CHA) topology (i.e. Cu-SSZ-13 and Cu-SAPO-34) have been shown promising catalysts for the elimination of hazardous nitrogen oxides via SCR of NO_x with NH_3.[283, 284] Kinetic studies combined with UV-Vis-NIR analysis,[285] *in situ* XAS studies,[286] and synchrotron *in situ* time-resolved X-ray diffraction measurements[287] indicated that the active species for the NH_3-SCR reaction in these Cu-zeolites are isolated mononuclear copper ions located in the 6-ring pores of the CHA framework, where both Cu^{2+} and Cu^{+} oxidation states coexist and are interconverted through a redox mechanism. However, recent studies combining reaction kinetics with DFT revealed that, under low temperature SCR conditions, copper cations solvated by NH_3 and H_2O migrate from their initial position in the 6-ring units to the 8-ring pores of the CHA structure forming a dimeric $[Cu^{+}(NH_3)_2]$ complex which, in the presence of O_2, leads to the active $[Cu^{2+}(NH_3)_2]$ -OO-$[Cu^{2+}(NH_3)_2]$ complex (Figure 22).[288-290] In opposite, at higher reaction temperatures, the Cu dimers dissociate regenerating the isolated Cu^{2+} species that move back to their initial position in the 6-ring CHA units and act as the active sites in the high temperature NH_3-SCR-NO_x reaction.

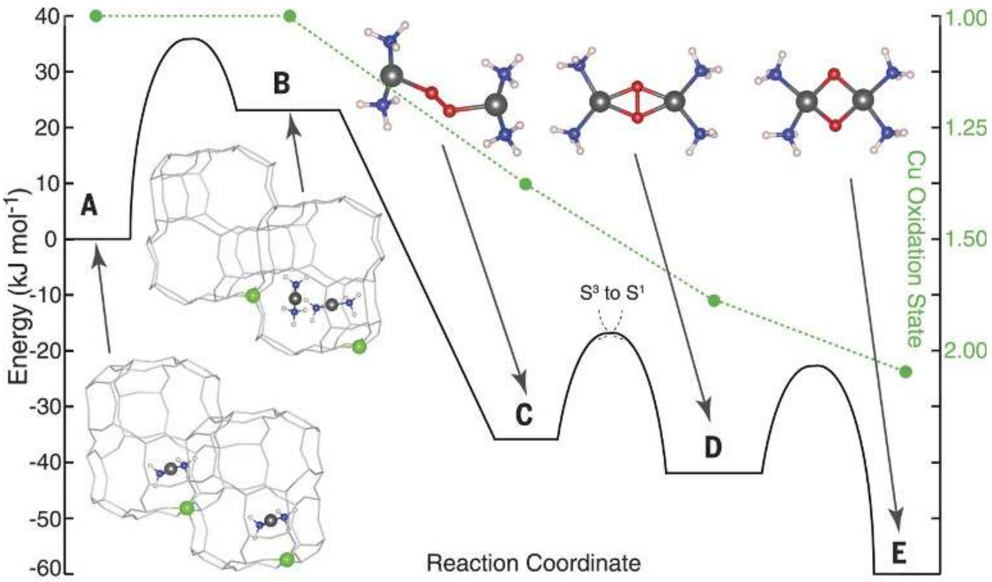

Figure 22. DFT energy scale for the diffusion of $Cu^+(NH_3)_2$ through an 8-ring CHA window into an adjacent cage and subsequent bimolecular reaction with O_2. Gray Cu, green Al, Red O, blue N, white H. Adapted from ref. [289]

In addition to Cu-CHA, Fe-MFI[291] and Ag-MFI[246] zeolites are also active catalysts for the selective reduction of NO with hydrocarbons (HC-SCR). In the case of Ag-MFI, the HC-SCR activity significantly raised with the addition of small amounts of H_2 to the feed which, based on *in situ* UV-Vis and EXAFS characterization, was attributed to the formation of Ag_4^{2+} clusters.[247] It has been shown that zeolites possessing acid sites of moderate strength are more effective in stabilizing the active Ag_4^{2+} species. Moreover, the nature of the Ag species changed with the composition of the feed. Hence, while Ag^+ and Ag^0 species prevail under oxidizing (i.e. NO- and O_2-rich) and reducing (i.e. H_2- and HC-rich) conditions, respectively, Ag_4^{2+} clusters are stabilized under intermediate reaction conditions.[248] This is a very nice example where both the zeolite acidity and the reaction atmosphere control the nature of the active metal species in the *working* catalyst and, in consequence, the catalytic activity.

The above studies clearly evidenced that the evolution of metal species under reaction conditions is a critical issue that has to be taken into consideration, and highlighted the need for performing *in situ* spectroscopic characterization, in combination with transient studies and DFT calculations, to elucidate the true nature of the active metal species in the *working* catalyst. Furthermore, the dynamic interconversion of metal species in response to changes in the reactive atmosphere can be exploited to develop new methodologies (e.g. by using different pretreatment conditions) for preparing catalysts with tailored metal sites.

3.3. Catalysis by metal-zeolites

The combination of catalytically active metal sites with the intrinsic shape selectivity of zeolites enables the design of metal-zeolite composite catalysts with improved activity and selectivity in a variety of relevant chemical transformations. Moreover, by introducing additional active sites (i.e. Brønsted and/or Lewis acid sites) in the zeolite host, multifunctional metal-zeolite catalysts displaying enhanced or new catalytic properties can be prepared as well. As, in some cases, metal-zeolite catalysts comprising different types of active sites (from monofunctional metal to multifunctional metal+acid) may be applied in a given catalytic applications, this section is organized according to the type of catalyzed reactions instead of by the nature of the active sites, as it was done in the first part of the review. Thus, the benefits of combinining metal species and zeolites with tailored active sites and porosity will be illustrated through selected examples covering a broad range of catalytic applications from the industrially-relevant hydroisomerization of *n*-alkanes to the synthesis of fine chemicals through selective hydrogenation and green oxidation reactions. Finally, the potential of tailored metal-zeolite catalysts in emerging sustainable processes, such as the valorization of natural gas (methane), CO_2, and biomass-derived compounds to fuels and chemicals will also be addressed. We put a special focus on most recent achievements highlighting how the special features offered by novel 2D, nanosized, and hierarchical (mesoporous) zeolites, such as a higher accessibility to the active sites and enhanced mass transport of reactants and products through the porous network can be exploited to design more active, selective, and stable metal-zeolite catalysts. For a wider view of the catalytic performance of supported single metal atoms, clusters, and nanoparticles we refer the reader to the excellent and exhaustive review recently published by Liu and Corma.[292]

3.3.1. Hydroisomerization of n-alkanes on bifunctional Pt/H-zeolites

The hydroisomerization of *n*-alkanes with different chain lengths using bifunctional Pt/H-zeolite catalysts is of high industrial relevance to the production of high-quality liquid fuels and lubricating oils.[293] For instance, Pt/H-MOR is commercially employed to increase the octane number of poor gasoline fractions like the LSR (*light straight run*) naphta cut through the skeletal isomerization of its main *n*-pentane and *n*-hexane components. On the other hand, Pt dispersed on 1D 10-ring zeolites like ZSM-22 (TON) and the silicoaluminophosphate SAPO-11 (MEL) are better suited to the selective hydroisomerization of long-chain *n*-alkanes (e.g. C_{10}-C_{20}) into their monobranched isomers to improve the cold flow properties of middle distillate fractions (diesel, kerosene) and lube oils.

The presence of metal (Pt) and zeolite Brønsted acid sites (H^+) in these bifunctional catalysts and hydrogen in the reaction mixture is essential to achieve high activity and isomer selectivity as well as to ensure long catalyst lifetime by suppressing coking reactions. However, the way Pt, H_2, and H^+ interact to form the active sites responsible for the activation of H_2 and *n*-alkanes and how these promote hydroisomerization reactions on bifunctional Pt/H-zeolite catalysts still remain controversial and several models have been brought forward to account for the experimental obervations. These aspects will be discussed first in sub-section 3.3.1.1. Then, in sub-section 3.3.1.2, we will overview the recent advances in the development of more efficient Pt/H-zeolite hydroisomerization catalysts, with a special attention to the benefits offered by non-conventional zeolites exhibiting enhanced mass transport and accessibility to the active sites.

3.3.1.1. Interplay between hydrogen, metal, and acid sites in Pt/H-zeolite catalysts

Traditionally, the hydroisomerization (and hydrocracking) performance of Pt/H-zeolite catalysts has been explained by the so-called *classical* bifunctional mechanism involving the following main steps: i) dehydrogenation of the *n*-alkane reactant on a metal site, ii) gas phase diffusion and protonation of the produced *n*-alkene on a zeolite Brønsted acid site to form an adsorbed secondary carbenium ion, iii) rapid rearrangement of the secondary carbenium ion into a more stable tertiary carbocation, and iv) desorption of the alkylcarbenium ion as an *iso*-alkene that diffuses (via gas phase) to a metal site where it is hydrogenated yielding the final *iso*-

alkane product. It is the possibility that the alkylcarbenium ion formed in step iii) undergo cracking via β-scission leaving a smaller adsorbed carbenium ion and an alkene in the gase phase. While this latter pathway is targeted in hydrocracking, it should be minimized in hydroisomerization in order to achieve high isomer yields. It is generally consented that a proper balance between metal and acid sites is essential to maximize the activity, selectivity, and stability of the bifunctional catalyst.[294]

The *classical* mechanism, however, does not provide a satisfactory explanation for the singular behaviour of hybrid catalysts comprising physical mixtures of Pt/SiO_2 (or Pt/Al_2O_3) and H-zeolites. Therefore, an alternative bifunctional pathway involving the concept of hydrogen spillover was introduced by Fujimoto and co-workers (Figure 23)[295, 296], according to which hydrogen activated on the noble metal migrates, presumably as protons (H^+) and hydride (H^-) species, via spillover (a surface diffusion phenomenon) to an acid site in the zeolite. The H^+ species assist the zeolite in activating the *n*-alkane via direct protonation (protolytic dehydrogenation) or hydride abstraction forming the corresponding carbenium ion, while H^- stabilizes the alkylcarbocation intermediates promoting the desorption of the *iso*-alkane product. The zeolite Brønsted acid sites are finally regenerated by spilt-over H^+ species.

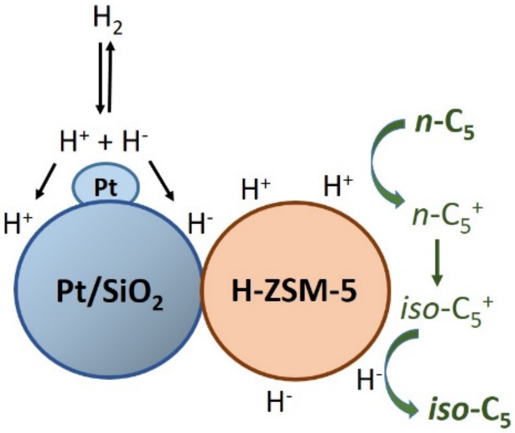

Figure 23. Hydrogen spillover model proposed by Fujimoto and co-workers for *n*-pentane isomerization on bifunctional hybrid Pt/SiO_2+H-ZSM-5 catalysts. Adapted from ref. [296]

Later on, Roessner et al.[297, 298] postulated a mechanism in which the spilt-over hydrogen species were assumed to be H radicals (initially formed by homolytic dissociation of H_2 on the metal), rather than the (unlikely) H^+/H^- species, acting as electron donors and establishing a dynamic equilibrium with protons on the zeolite surface.[298] As shown in Scheme 10, a spilt-over hydrogen radical (H^*_{spill}) abstracts a H atom from the reactant *n*-alkane leading to a surface hydrocarbon radical and H_2 (reaction 1); the hydrocarbon radical then reacts with a zeolite Brønsted acid site (represented by H^+OZ^-) and transforms into a secondary carbenium ion (reaction 2) that quickly isomerizes into a tertiary carbocation (reaction 3). Finally, the *iso*-alkane product is formed and desorbed with the participation of hydrogen spilt-over species (i.e. neutral radicals, H^*_{spill}, and protons, H^+_{spill}) through reactions 4 to 6.

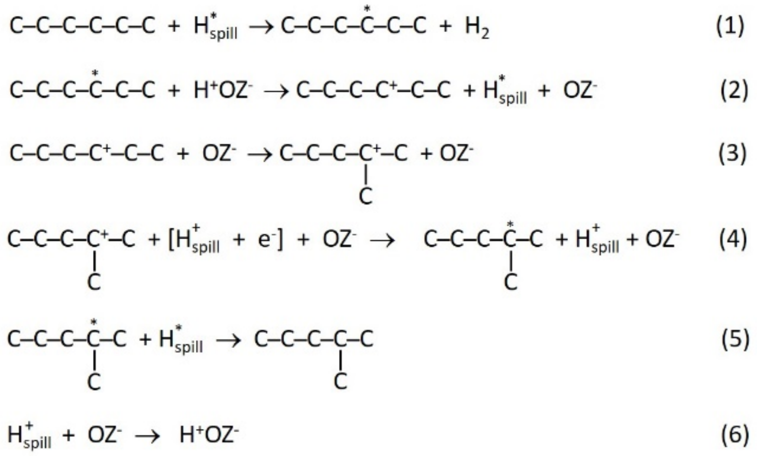

Scheme 10. Bifunctional *n*-hexane isomerization mechanism according to the hydrogen spillover model postulated by Roessner et al. (adapted from ref. [298]).

The hydrogen spillover model of bifunctional catalysis simplifies the *classical* mechanism by avoiding the gas phase travelling of alkenes from metal to acid sites (and *viceversa*) and the necessity of multiple adsorption-desorption steps, as the hydrocarbon conversion exclusively occurs on the zeolite acid sites assisted by nearby spilt-over hydrogen continuously supplied from the metal centres. Nonetheless, the possible participation of metal sites in the initial activation of alkanes via dehydrogenation following the *classical* pathway is not excluded. Poor fundamental understanding of the hydrogen spillover phenomena and the precise nature of the involved surface species, however, lead Lunsford and co-workers to propose an alternate, less speculative mechanism by which isomerization of the starting *n*-alkane occurs mainly on the zeolite acid sites via a chain mechanism involving acid-catalyzed methyl shifts and hydrogen transfer steps. [299] The final *iso*-

alkane is formed upon hydrogenation of the adsorbed alkylcarbenium ion (termination step), and the main role of Pt is proposed to be the rapid hydrogenation of alkenes, so as to keep their steady-state concentration sufficiently low to prevent detrimetral secondary reactions.

A somewhat different mechanistic picture for the hydroisomerization of *n*-alkanes on Pt/H-zeolite catalysts was suggested by Lónyi et al.[300]. In this model, the active sites, generated in situ upon heterolytic dissociation of both H_2 and *n*-alkane (R_1) on cationic Pt species, are suggested to be neutral Pt hydride/Brønsted acid site pairs [Pt^0-*n*H + *n*ZO^-H^+] and Pt hydride/carbenium ion pairs [Pt^0-*n*H + *n*$ZO^-R_1^+$] in dynamic equilibrium with the gas phase reactants (Scheme 11). The linear carbenium ions (R_1^+) isomerize to branched carbenium ions (R_2^+) forming [Pt^0-*n*H + *n*$ZO^-R_2^+$] pairs that are continuosly exchanged for linear carbenium ions or protons via rapid hydride transfer maintaining the catalyst surface-gas phase equilibrium. The relative rate of exchange by linear carbenium ions (propagation) and protons (termination) determines the overall isomerization rate. In addition to the proposed active sites, large Pt^0 particles displaying high hydrogenating activity were claimed necessary to rapidly hydrogenate alkenes eventually formed by cracking ensuring, thus, a high and stable isomerization activity.

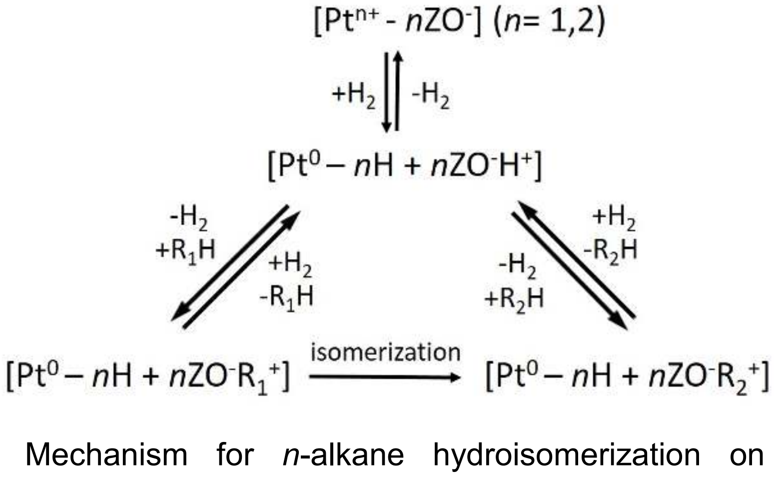

Scheme 11. Mechanism for *n*-alkane hydroisomerization on Pt/H-zeolites according to the model proposed by Lónyi et al. (adapted from ref. [300]). R_1H and R_2H stand for the *n*-alkane reactant and the corresponding *iso*-alkane, respectively, while ZO- represents a zeolite framework entity carrying a single negative charge.

3.3.1.2. Advanced Pt/H-zeolite catalysts for *n*-alkane hydroisomerization

Regardless of the mechanism operating in the hydroconversion of hydrocarbons over bifunctional Pt/H-zeolites, it is accepted that the overall reaction is controlled by the acid-catalyzed steps occurring on the zeolite Brønsted acid sites. However, slow diffusion of reactants and/or products and poor accessibility to the active sites within the micropores of conventional 3D zeolites may impair the activity and selectivity of the bifunctional Pt/H-zeolite catalysts. Obviously, this effect is more prominent for bulkier reactants and for zeolites with smaller pore sizes. To alleviate diffusional and accessibility issues, nanosized, nanosheet, and hierarchical (micro-mesoporous) zeolites with enhanced accessibility to the acid sites and shorther diffusion paths have been intensively investigated in the past years as acid components of bifunctional Pt/H-zeolite catalysts in hydroconversion reactions. In the case of hydroisomerization of relative small short-chain (C_5-C_6) *n*-alkanes, for which Pt/H-MOR is the benchmark zeolite-based catalyst employed in commercial units, mass transfer limitations and restricted access to the Brønsted acid sites, especially to those located in the 8-ring side pockets exhibiting higher TOF[301], negatively impact the catalyst performance. In a recent work, the introduction of secondary mesoporosity while preserving a large amount of acid sites in H-MOR through alkaline-acid, acid-alkaline, and flurination-alkaline post-synthesis treatments largely improved the efficiency of Pt/H-MOR for *n*-hexane hydroisomerization, resulting not only in a higher activity but also in a higher selectivity to the desired high-octane dibranched isomers in comparison with a conventional Pt/H-MOR catalyst (Figure 24).[302]

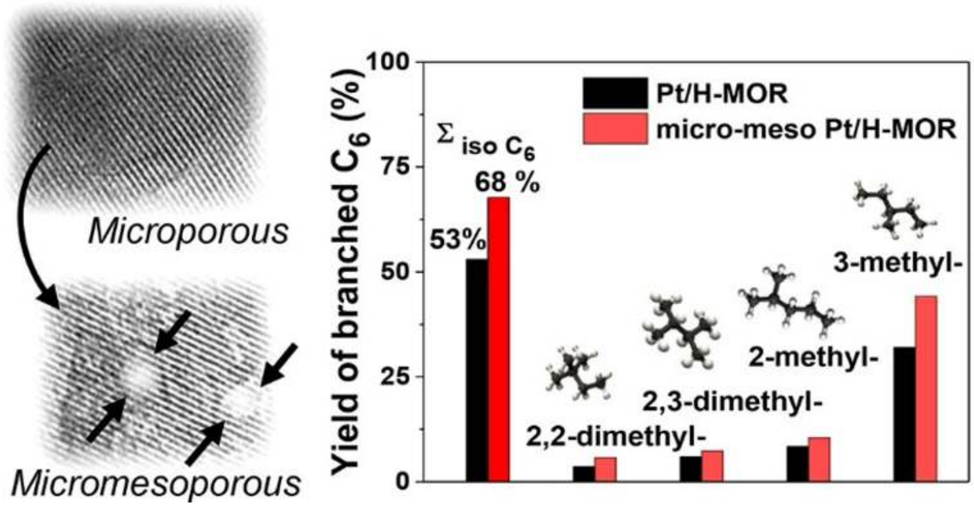

Figure 24. Improved catalytic performance for *n*-hexane hydroisomerization of Pt/H-MOR catalysts upon introduction of mesopores in the zeolite crystals. Adapted from ref. [302]

Outstanding isomer yields of up to 79% in the hydroisomerization of *n*-heptane have been reported for a hierarchical macro-meso-microporous Pt/H-SAPO-11 (AEL, 1D, 10-ring) obtained through an oriented assembly strategy using prefabricated nanocrystallites as a precursor[303], and for a nanocrystalline Pt/H-SAPO-31 (ATO, 1D, 12-ring) spheroids produced by a phase-transfer synthetic strategy.[304] Decreasing the diffusion path length through reduction of the zeolite crystal thickness to nanosheets in Pt/H-ZSM-5 catalysts has also been shown to significantly enhance the selectivity to branched products in *n*-heptane hydroisomerization by minimizing consecutive cracking reactions.[305] Very interestingly, by using a series of micro- and micromesoporous MFI, MOR, *BEA, and FAU zeolites, Sazama et al. have recently demonstrated that the presence of mesopores does not alter the shape selectivity inherent to each zeolite structure during the hydroisomerization of *n*-hexane, as the reaction was shown to be uniquely driven by the simultaneous interaction of the reactant molecules with the confined Brønsted acid sites and the inner zeolite walls.[306] This conclusion implies that, in principle, the advantages of using mesoporous zeolites could be fully exploited to design more efficient catalysts while preserving the shape selectivity of the zeolite.

Selective hydroisomerization of long-chain (e.g. C_{10}-C_{24}) *n*-alkanes is of high industrial relevance to produce high-quality lubricating oils and middle distillate fuels with appropriate burning and cold flow characteristics.[307] To this purpose, high selectivity to monobranched isomers with limited product losses by cracking is desired. Bifunctional catalysts based on Pt loaded on 10-ring zeolites with unidirectional tubular channels like ZSM-22 and SAPO-11 display unique features for this reaction that were explained by the so-called pore mouth catalysis in pore openings of the zeolite[308, 309] or by shape selectivity inside their 1D pores[310]. Nonetheless, since the presence of strong Brønsted acid sites in [Al]-zeolites tend to promote side cracking reactions in detriment of target isomers[311], tailoring of the acid sites is required to improve selectivity. In this regard, a much higher isomer selectivity in the hydroisomerization of *n*-dodecane has been reported for Pt/[Al,Fe]-ZSM-22 in comparison with Pt/[Al]-ZSM-22 due to both a reduction in the average acid strength and in crystallite size upon partial isomorphous substitution of framework Al^{3+} with Fe^{3+} atoms.[312] More recently, increased selectivity to monobranched isomers in *n*-dodecane hydroisomerization has been reported for a highly siliceous (i.e. low acidic) ZSM-22 zeolite, obtained by hydrothermal synthesis with the aid of ZSM-22 seeds, loaded with low amount of Pt (0.2 wt%) to keep a proper metal-acid balance.[313]

Moreover, reduced accessibility and increased mass-transport restrictions in the 1D 10-ring tubular pores limit the activity and make these zeolites more prone to deactivate during the hydroisomerization of long-chain *n*-alkanes. In this respect, mesoporous ZSM-22 produced by desilication followed by acid treatment to remove extra-framework Al species and liberate the micropores improved the yield to monobranched isomers in *n*-octane hydroisomerization compared to its purely microporous analogue.[314] Exceptional high yields of up to 92% to the target isomers have been reported in the hydroisomerization of *n*-nonadecane over a hierarchical Pt/H-ZSM-22 catalyst obtained by a similar sequential desilication+acid treatment.[315] In a late study, the acidity of a ZSM-22 zeolite with low Si/Al ratio (< 20) was tailored by simply adjusting the concentration of NaOH during the alkaline desilication treatment as some of the acid sites were blocked by generated extra-framework Al species, producing Pt/ZSM-22 catalysts with enhanced isomerization selectivity in the conversion of *n*-dodecane, in spite of the minor increase in mesoporosity.[316] The generation of secondary mesoporosity in 1D 10-ring zeolites generally increases the amount of unconstrained external acid sites on which undesired multiple branching and cracking reactions are favored. For hierarchical Pt/H-SAPO-11, it has been shown that generation of mesopores using carbon black as mesoporogen lead to the preferential location of acid sites inside the channels and, consequently, to improved isomer yields (up to 84%) in the hydroisomerization of *n*-dodecane.[317] In a later work, Tao et al. reported a facile synthetic approach to prepare hierarchical SAPO-11 comprising microspheres with uniform intercrystalline mesopores sizing ca. 4.3 nm based on the dry-gel conversion of a silicoaluminophosphate-organosilane composite, as illustrated in Figure 25a.[318] Interestingly, adjusting the water content in the synthesis enabled to finely tune the acidity of the produced hierarchical SAPO-11 material, probably by changing the distribution of framework Si atoms. The Pt/hierarchical SAPO-11 catalysts displayed higher selectivity to isomers than conventional Pt/SAPO-11 in the hydroisomerization of *n*-hexadecane (Figure 25b). Moreover, Pt/SAPO-11 catalysts comprising stable nanosheets of 10-20 nm thickness and with acid sites in the micropores partly blocked by extra-framework amorphous alumina species exhibited higher isomer selectivity in the hydroisomerization of *n*-dodecane than Pt/SAPO-11 with bulk crystals.[319]

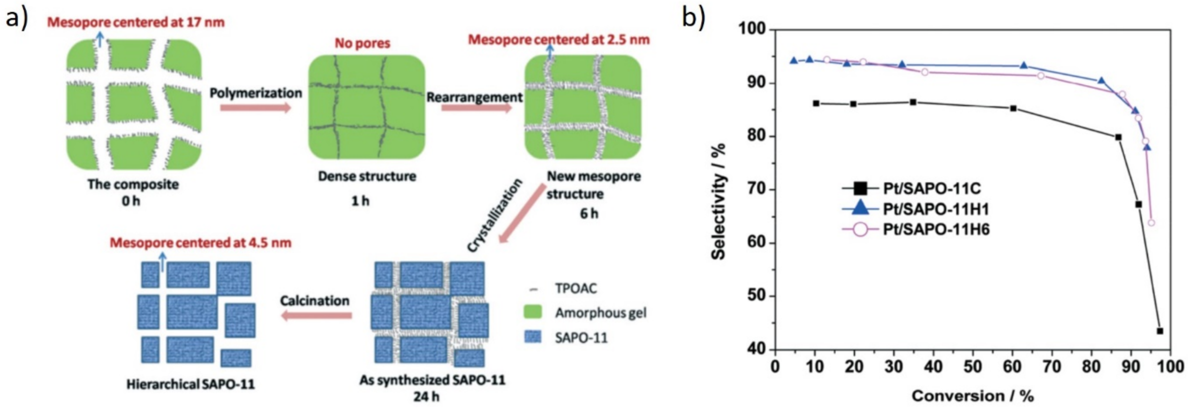

Figure 25. a) Schematic representation of the synthesis of hierarchical SAPO-11 by dry-gel conversion of a silicoaluminophosphate-organosilane composite. b) Selectivity to isomers as a function of *n*-hexadecane conversion on hierarchical (H1 and H6 samples) and conventional (C sample) Pt/SAPO-11 catalysts (WSHV= 2.0 h^{-1}, H_2/*n*-C_{16} (mol)= 15, P= 8.0 MPa). Adapted from ref. [318]

Besides site accessibility and acidity of the zeolite, the location of the Pt species and the degree of intimacy between metal and Brønsted acid sites has also a significant impact on the hydroisomerization performance of Pt/H-zeolites.[320-322] Moreover, the size and orientation of Pt crystallites has been found to heavily influence the *n*-alkane hydroisomerization behaviour of bifunctional Pt/H-zeolites. Thus, by combining HRTEM with CO-IR spectroscopy, it has been shown that Pt/H-ZSM-22 catalysts prepared from Pt^{4+} precursors exhibit smaller Pt^0 particles preferentially exposing more active Pt{111} corner sites and higher activity and selectivity in the hydroisomerization of *n*-hexadecane than those obtained from Pt^{2+} precursors leading to larger metal particles with more Pt{100} facets.[323]

The above examples provide clues to the rational design of more efficient bifunctional Pt/H-zeolite catalysts for the hydroisomerization of *n*-alkanes of different chain length. Thus, the use of nanocrystalline, nanosheet, and mesoporous zeolites with enhanced accessibility to active sites and shorther diffusion paths, in combination with a fine tuning of the amount and location of both metal and Brønsted acid sites and their degree of intimacy, should enable the preparation of Pt/H-zeolite catalysts with improved activity and selectivity to the targeted isomers.

3.3.2. Sulfur-resistant noble metal-zeolite catalysts

The development of sulfur-resistant catalysts based on noble metals (e.g. Pt) displaying high hydrogenation activity is of industrial relevance for the production of high-quality transport fuels in refineries. Several strategies have been devised to enhance the sulfur resistance of supported noble metal catalysts, most of them relying on increasing the electron deficiency of the metal through alloying (as in bimetallic Pt-Pd catalysts) and/or though interaction with acid sites in Al-containing zeolites. Another interesting approach is based on incorporating the noble metal in zeolites containing pores of different sizes, such as in MOR, so that the access of organosulfur compounds to the metal nanoparticles located in the small 8-ring pockets is avoided by size exclusion.[324] The protected Pt nanoparticles were thus still active for activation of H_2 allowing self-regeneration of the readily poisoned Pt nanoparticles in the 12-ring channels. However, poisoning of the Pt sites in the 8-ring side pockets by small (3.6 Å) H_2S molecules formed during hydrotreating was finally inevitable. In this direction, a very interesting approach that eliminates the possibility of contact between Pt and H_2S while still allowing the activation of the smaller H_2 molecules (2.89 Å) has been proposed in where the metal is effectively encapsulated in the small pores of zeolite KA whose pore openings were further reduced by chemical vapor deposition (CVD) of silicon alkoxides (e.g. TEOS) (Figure 26).[325] An hybrid catalyst was then prepared by mixing the Pt@KA catalyst with zeolite HY in where H_2 is activated on the encapsulated Pt sites and diffuses via spillover to the neighboring HY zeolite enabling the catalyst to retain a relatively high activity for the hydrogenation of bulky aromatics (e.g. naphthalene) in the presence of H_2S (3 vol% in H_2).

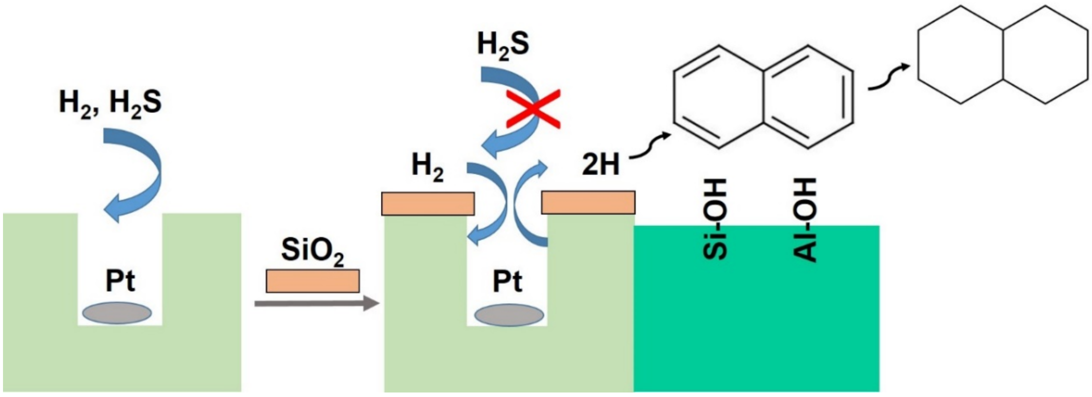

Figure 26. Scheme of the concept of thioresistance of the TEOS-Pt/NaA zeolite. Adapted from ref.[325]

3.3.3. Chemoselective hydrogenations

Metal-zeolite catalysts exhibit interesting chemoselectivity in the hydrogenation of α,β-unsaturated aldehydes to unsaturated alcohols (intermediates in the production of fragances and pharmaceuticals), where steric constraints imposed by micropores determine the preferential adsorption of the aldehyde through the terminal C=O group (end-on adsorption) vs. the C=C group. Besides geometrical effects, electronic effects by which metal nanoparticles confined within zeolites pores are electron-enriched may also promote high selectivity to the unsaturated alcohols, as it has been shown for Ru/KL catalysts displaying high activity and selectivity to citronellal in the hydrogenation of citral.[326, 327] High selectivity toward the hydrogenation of the C=O group of citral has also been achieved on a bifunctional Pt/Sn-*BEA catalyst by coupling the confinement effects with the rational design of active sites comprised of isolated Lewis acid sites (associated to framework Sn^{4+} species) and nearby small alloyed Pt-Sn clusters (< 1 nm) located inside the zeolite pores.[328] In this catalyst, the close proximity between Pt and Sn in the bimetallic clusters and framework Sn^{4+} sites favors the interaction of the C=O group in a *tilt* configuration (Pt–C=O···Sn^{4+}) where C=O interacts with Pt via $C\sigma$ bonding and π^*CO antibonding, and the oxygen interacts with the adjacent Sn^{4+} Lewis acid sites weakening the C=O bond and promoting its selective hydrogenation. The Pt/Sn-*BEA catalyst attained 80% yield of the unsaturated crotyl alcohol (UA) at 92% citral conversion with a productivity of 0.281 $\mu mol_{UA}/g_{cat}$ after 4 h. This productivity is notably higher than that reported for a benchmark Pt-Sn/Al_2O_3 catalyst (0.097 $\mu mol_{UA}/g_{cat}$).[329]

The selective hydrogenation of substituted nitroaromatics with multiple reducible groups to the corresponding substituted anilines is another important process for the production of pharmaceuticals and pesticides. Recent studies demonstrate how by controlling the micro and mesoporosity in core-shell metal-zeolite catalysts it is possible to achieve high substrate-size selectivity in the hydrogenation of nitroaromatic compounds of different molecular sizes. For instance, selective hydrogenation of nitrobenzene vs. bulkier 1-nitronaphtalene was accomplished with a mesoporous core-shell 1.7wt% Pd@mnc-S1 catalyst.[233] The presence of mesopores in the silicalite-1 shell provided enhanced diffusion rates of reactants and increased, accordingly, the reaction rate (Figure 27).

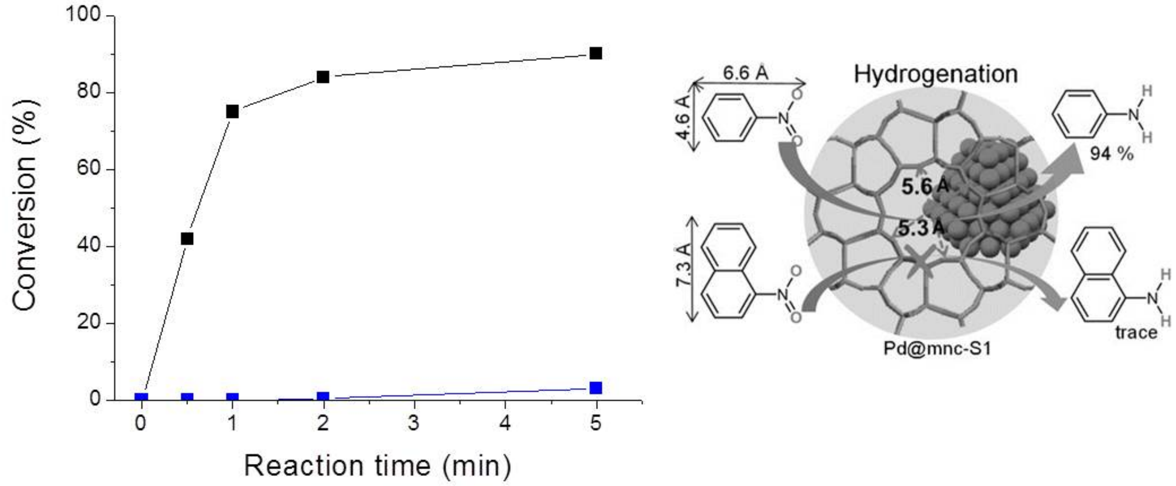

Figure 27. Conversion of nitrobenzene (black) and 1-nitronaphtalene (blue) on 1.7 wt% Pd@mnc-S1 mesoporous core-shell catalysts. Reaction conditions: 0.1 mmol nitrobenzene or 1-nitronaphtalene, 20 mg of catalyst, 0.2 mmol $NaBH_4$, 5 ml H_2O, 25 °C. Adapted from ref. [233]

On the other hand, modulation of the diffusion of reactants by tuning the zeolite pore size was performed to control the adsorption mode of nitroaromatic molecules on confined metal sites in a specific conformation that favors the selective hydrogenation of the nitro group. This has been demonstrated for a core-shell Pd@*BEA (Si/Al = 13) zeolite displaying an exceptional high product selectivity (> 99%) at 100% conversion in the hydrogenation of 4-nitrochlorobenzene (Figure 28), outperforming both conventional zeolite-supported Pd nanoparticles and a commercial Pd/C catalyst.[236] The synergy achieved by combining the high activity of metal nanoparticles with the selective reactant adsorption in zeolite micropores was further extended to other core-shell metal@zeolite catalysts (e.g. Pd@MOR, Ru@*BEA, and Pt@*BEA) showing excellent performance in the chemoselective hydrogenation of various nitroarenes.[236]

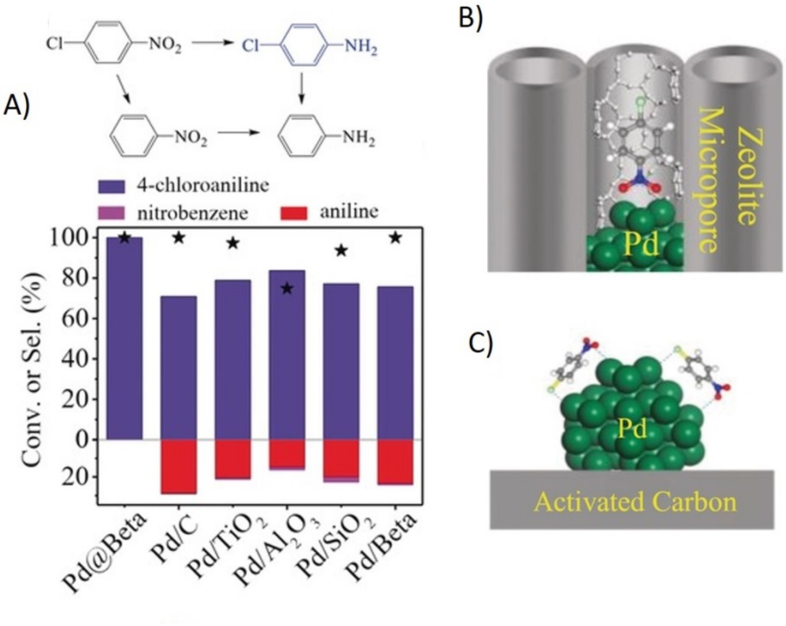

Figure 28. A) Conversion (*) and selectivities to the different products (coloured columns) in the hydrogenation of 4-nitrochlorobenzene on various catalysts. Reaction conditions: 1 mmol 4-nitrochlorobenzene, 0.2 mol% Pd catalyst, 10 ml toluene, 1 MPa H_2, 110 °C, 45 min. Model of 4-nitrochlorobenzene adsorption on B) Pd@Beta and C) Pd/C (C: grey, Cl: light green, H: white, N: blue, O: red, Pd: dark green). Adapted from ref. [236]

In another interesting example, the cooperation between metal sites and zeolite Brønsted acid sites was advantageously exploited to afford the one-pot synthesis of *para*-aminophenol from nitrobenzene using a mesoporous core-shell Pt@H-ZSM-5 catalyst.[330] As seen in Figure 29, the hydrogenation of nitrobenzene (NB) proceeds through the intermediate product N-phenylhydroxylamine (PHA) that can be further hydrogenated to aniline (AN) on the metal sites (route1) or alternatively converted to *para*-aminophenol (PAP) on the zeolite acid sites (route 2). In the case of Pt@H-ZSM-5, the close proximity between Pt and acid sites favors route 2 vs. route 1 enabling the one-pot synthesis of PAP with 60% selectivity at 100% NB conversion. A comparatively much lower selectivity (11% at 100%

conversion) was attained on an equivalent Pt/H-ZSM-5 catalyst prepared by impregnation comprising mostly metal nanoparticles outside the zeolite pores, highlighting the need to rationally tailor the different active sites in bifunctional metal-zeolite catalysts to achieve the desired catalytic performance.

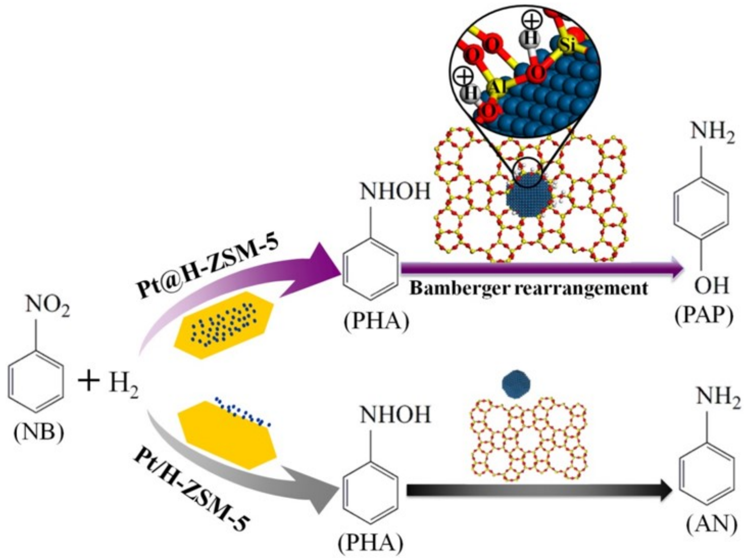

Figure 29. Scheme of the hydrogenation of nitrobenzene to p-aminophenol on a core-shell Pt@H-ZSM-5 zeolite and on an impregnated Pt/H-ZSM-5 sample. Adapted from ref. [330]

3.3.4. Epoxidation of propylene

Previous studies based on both theoretical calculations and catalytic experiments clearly showed that the nature of activated oxygen species is crucial in directing the selectivity in oxidation reactions. Adsorption and dissociation of molecular O_2 on metals may lead, depending on the electronic properties and structural configuration of the metal surface sites, to different oxygen species (i.e. peroxo, superoxo, atomic O, O adatoms, etc.)[331, 332] exhibiting dissimilar reactivity.

A challenging oxidation process is the epoxidation of propylene with molecular O_2 using heterogeneous catalysts. Propylene oxide (PO) is an important intermediate in the fabrication of polyurethanes, polyesters, and solvents whose production at industrial scale takes place through a multistep process using homogeneous catalysts and organic peroxides (e.g. TBHP) as oxidants. Extensive research has been conducted in the past years to develop efficient and environmentally friendly routes for the synthesis of PO, among which the direct epoxidation of propylene with molecular O_2 or hydrogen peroxide generated *in situ* from H_2 and O_2 on heterogeneous catalysts are worth mentioning. In this respect, an encouraging selectivity to PO of up to ca. 89% at 2% conversion has been reported for Au/TS-1 catalysts prepared by deposition-precipitation.[333] As evidenced by means of *in situ* EPR, UV-Vis, and XANES spectroscopies, highly dispersed gold nanoparticles are responsible for the *in situ* generation of H_2O_2 from H_2 and O_2 while propylene epoxidation takes place on Ti-hydroperoxo species (Ti^{4+}–OOH) formed in TS-1 acting as true intermediates in the reaction, acoording to the reaction mechanism illustrated in Scheme 12.[333, 334]

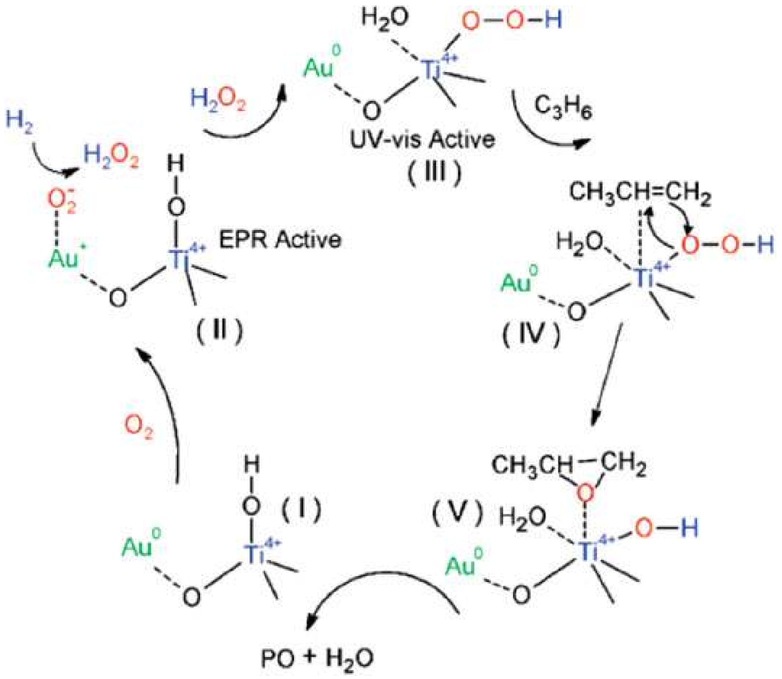

Scheme 12. Reaction steps in the propene epoxidation with O_2 and H_2 over Au/Ti-silicalites. Adapted from ref. [334]

More recently, an even higher selectivity to PO of 93.2 – 96.4% (at a propene conversion of ~2%) was achieved with an Au/TS-1@mesoporous silica core-shell catalyst, in which small (2 nm) gold nanoparticles are stabilized in the mesoporous silica shell.[335] The separation of gold sites from Ti sites in the composite catalyst was essential to achieve such a high selectivity by preventing further hydrogenation of PO (Figure 30). Moreover, the Au/TS-1@mesoporous silica catalyst showed high stability during the epoxidation reaction in tests lasting 54 h. Nonetheless, the yields achieved up to now are too low for practical application, and further investigations are advised to make these processes more industrially attractive.

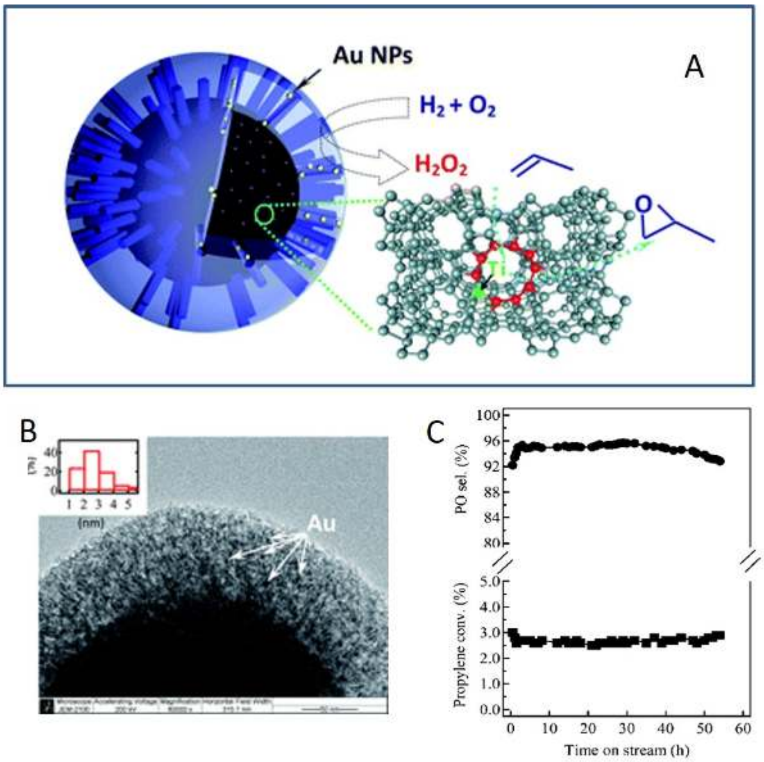

Figure 30. A) Epoxidation of propene on Au/TS-1@meso-SiO_2 catalyst. B) HRTEM image of the catalyst showing the distribution of Au nanoparticles in the mesoporous TS-1 shell and the size distribution of the Au particles (inset). C) Propene conversion and selectivity to PO. Reaction conditions: 0.3 g_{cat}, $C_3H_6/H_2/O_2/N_2$= 2/2/2/14 $cm^3 \cdot min^{-1}$, space velocity 4000 $cm^3 \cdot g_{cat}^{-1} \cdot h^{-1}$, 150 °C, 1 bar. Adapted from ref. [335]

3.3.5. Direct conversion of methane

High stability of the C–H bonds of methane (the main component of natural gas) makes its direct conversion to fuels and value-added chemicals challenging. Activation of methane in the presence of O_2, as in the oxidative coupling to ethylene and partial oxidation to methanol and formaldehyde, is thermodynamically favored although it suffers from low product yields due to the overoxidation of the reaction products to carbon oxides at increasing conversions.

Inspired by nature, scientists have expended significant efforts trying to develop artificial catalysts that mimic the active sites present in methane monooxygenase enzyme to drive the direct oxidation of methane to methanol at ambient temperature. Following this idea, heterogeneous catalysts containing binuclear[250, 336, 337] or even trinuclear copper,[251, 338] iron,[254, 339, 340] and nickel[253] species stabilized in zeolites (ZSM-5,[253, 254, 336] MOR, [250, 338] SSZ-13,[252] SSZ-16, [252] SSZ-39[252]) have been shown active for the direct oxidation of methane to methanol at low temperatures (150 – 200 °C). The reaction, however, takes place in a non-catalytic manner and, once formed, methanol needs to be extracted from the zeolite pores with steam at temperatures of 200 °C[252] or 400 °C. [250] *In situ* UV-Vis and resonance Raman spectroscopic measurements combined with $^{18}O_2$ isotopic labeling experiments and DFT calculations identified bent mono-(μ-oxo) dicupric species (i.e. $[Cu(\mu\text{-}O)Cu]^{2+}$) in Cu-ZSM-5 and trimeric ($[Cu_3(\mu\text{-}O)_3]^{2+}$) species stabilized in the 8-ring side pockets of Cu-MOR as the active sites for the low-temperature activation of methane.[250, 251, 338, 341] In spite of the different nature of the active sites in Cu-ZSM-5 and Cu-MOR, the DFT calculations indicated a similar low activation barrier for C–H bond activation on binuclear (~ 78 $KJ \cdot mol^{-1}$) and trinuclear (~ 74 $KJ \cdot mol^{-1}$) copper species. However, the reported copper site yields in these catalysts are relatively low (0.03 – 0.09 $mol_{MeOH} \cdot mol_{Cu}^{-1}$), suggesting that only a minor fraction of the Cu present in the zeolite is involved in the formation of methanol. Once the reaction cycle is completed, reactivation of the Cu sites is performed by flowing dry oxygen at 400 °C. [250] In a different approach, a mixture of CH_4, H_2O, and O_2 is flowed over the Cu-ZSM-5 catalyst at a temperature of 210 °C, where water in the feed hydrolyses the Cu-bound methoxy species enabling the continuous production of methanol with a total yield of 491 $\mu mol_{MeOH}/g_{cat}$ after 288 h of reaction without apparent deactivation.[342] Interestingly, combined spectroscopic and kinetic studies evidenced that the active Cu sites in this case are ultrasmall Cu oxide clusters generated *in situ* rather than the mono-μ-oxo-dicuppric $[Cu(\mu\text{-}O)Cu]^{2+}$ species proposed for the stoichiometric oxidation. Methanol formation rates in Cu-zeolites varied with the Cu content, Brønsted acidity of the zeolite, and zeolite topology. Thus, Cu/Al atomic ratios above 0.3 increased the steady state specific activity (per mass of catalyst) but decreased the site time yield (i.e., the methanol formed per Cu site), while the presence of Brønsted acid sites increased both parameters. Regarding the zeolite topology, zeolites possessing small pores or cage-like structures such as Cu-SSZ-13 and Cu-SAPO-34 afforded higher site time yields than Cu-ZSM-5, while large pore *BEA and FAU zeolites displayed poorer catalytic performance.[342]

Direct oxidation of methane to acetic acid can also been accomplished using bifunctional Cu-H-MOR zeolites through a tandem oxidation-carbonylation reaction sequence. While oxidation of methane takes place on Cu sites, carbonylation of the formed methoxy species preferentially occurs on specific Brønsted acid sites (those located in T3-O33 positions) in the 8-ring pockets of the MOR structure.[343] With the support of DFT calculations, the specificity of the zeolite protons in this particular location for the carbonylation reaction was proposed to arise from their ability to stabilize the involved acetyl-like transition states within the restricted space of the narrow 8-ring pockets.

Besides, a Rh-ZSM-5 catalyst (0.5 wt% Rh), prepared by successive impregnation and washing steps followed by reduction in H_2 at 550 °C, has also been shown active for the direct oxidation of methane to methanol and acetic acid at 150 °C in the presence of O_2 and CO in a batch reactor using water as solvent.[344] Isolated Rh^+ ions, evidenced by HRTEM, IR-CO, and EXAFS were proposed as active sites for the activation of methane through the formation of $Rh\text{-}CH_3$ species, which can be then converted either to methanol (via a $Rh\text{-}OCH_3$ intermediate) or to acetic acid (via a $Rh\text{-}COCH_3$ intermediate) depending on the zeolite acidity. More acidic zeolites promoted the formation of acetic acid vs. methanol, which enables to drive the reaction selectivity towards a specific product by tailoring the acidity of the ZSM-5 zeolite. For instance, acetic acid preferentially formed after reaction at 150 °C for 3 h on acidic Rh/H-ZSM-5 while methanol was predominantly produced on Rh/Na-ZSM-5 (lacking Brønsted acid sites) under analogous conditions (Figure 31). Nonetheless, a relative oxygenate yield loss of ca. 25% due to aggregation of Rh species under reaction conditions was observed after the second regeneration cycle, which calls for further optimization studies in view of a practical implementation.

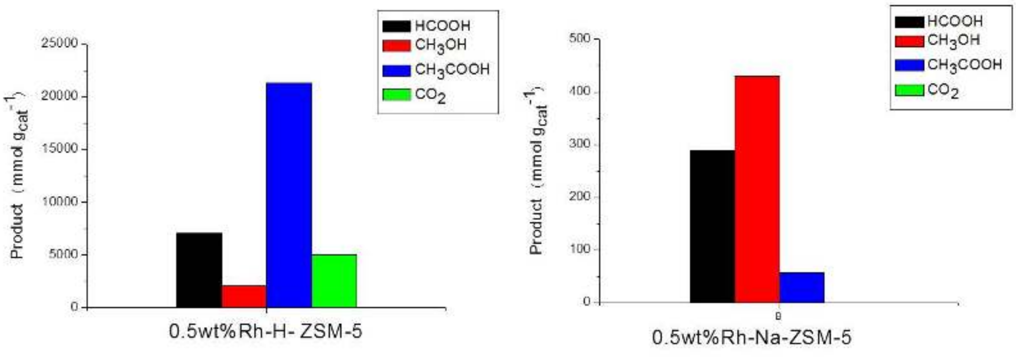

Figure 31. Catalytic performance of Rh-H-ZSM-5 (left) and Rh-Na-ZSM-5 (right) catalysts in the oxidation of methane. Reaction conditions: 20 mg catalyst, 150 °C, 2 bar O_2, 5 bar CO, 20 bar CH_4, 20 ml H_2O, and 3 h of reaction. Adapted from ref. [344]

Methane can be directly converted to valued raw petrochemicals (e.g. ethylene and benzene) in the absence of O_2 at relatively high temperatures (600 – 700 °C) using Mo-containing zeolites as catalysts. For instance, methane can be converted to mainly benzene (with co-production of H_2) through the so-called non-oxidative methane dehydroaromatization (MDA) reaction on bifunctional Mo/H-ZSM-5 and Mo/H-ZSM-22 at temperatures of ~700 °C.[345] In this reaction, most studies support that methane activation and formation of C_2 (mainly ethylene) intermediates occurs on carburized Mo sites, while oligomerization and cyclization of ethylene to benzene takes place on the zeolite Brønsted acid sites. According to X-ray adsorption (XANES/EXAFS) and Ultrahigh Field ^{95}Mo NMR spectroscopic measurements in combination with isotopic kinetic studies, the active sites for the activation of C–H bonds in methane and initial formation of C_2 intermediates in *working* Mo/zeolite catalysts were suggested to be MoC_x clusters highly dispersed in the zeolite pores.[346, 347] The active molybdenum carbide clusters are originated from cationic Mo oxo species (e.g. dimeric $Mo_2O_5^{2+}$ cations) exchanging zeolite protons in the pre-reacted (calcined) catalyst that are carburized upon contact with CH_4 at MDA conditions in the initial reaction stages. However, in a very recent and stimulating work, Kosinov et al. performed pulse MDA reactions at 700 ºC coupled to mass spectrometry, *operando* XANES, EPR, and XPS spectroscopies, pulse isotopic $^{12}CH_4$ /$^{13}CH_4$ exchange experiments, and high-resolution HAADF-STEM microscopy to shed more light on the nature of active Mo species and MDA mechanism on a benchmark Mo/H-ZSM-5 catalyst.[348] Based on their experimental results, the authors proposed that the active centres in the *working* Mo/H-ZSM-5 catalyst are partially reduced single-atom Mo sites (formed by reduction of ion-exchanged Mo^{6+} species during the initial activation and induction periods) stabilized by the zeolite framework (Figure 32a). In contrast to the general belief, molybdenum carbide species were concluded to be mere spectators on the external catalyst surface. The single-atom Mo sites are proposed to activate methane at MDA conditions producing reactive radicals (detected by EPR) or C_2H_x fragments that react with a pool of polyaromatic species (e.g. acenes) confined in the zeolite pores leading to benzene (and H_2), probably through hydrogenolysis reactions (Figure 32b).[348] This recent result may stimulate further research to elucidate the exact role of the hydrocarbon pool intermediates as an starting point to develop more efficient MDA catalysts.

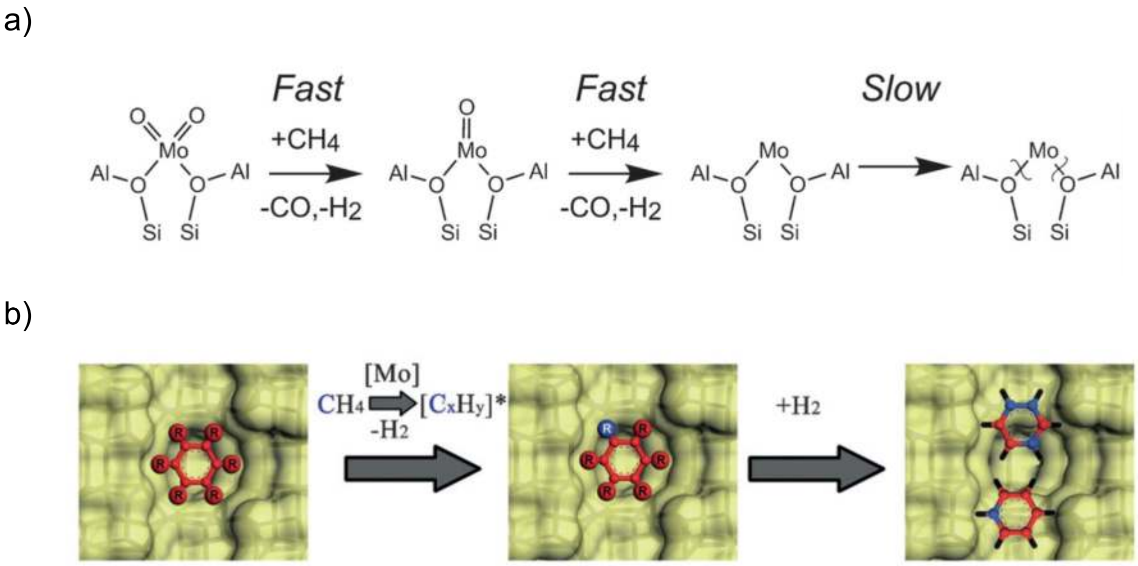

Figure 32. a) Proposed evolution of the active Mo phase during the activation and induction period of the MDA reaction. b) MDA mechanism leading to benzene from confined aromatic-type carbon species (R substituents are aromatic rings; ^{13}C and ^{12}C atoms are shown in red and blue, respectively). Adapted from ref. [348]

Interestingly, dispersing Mo_2C on a low-acidic [B]-ZSM-5 zeolite instead of [Al]-ZSM-5 was seen to shift the product selectivity from benzene to ethylene (91% selectivity) at temperatures close to those applied in MDA (650 °C) while significantly decreasing the catalyst deactivation rate, a major drawback in MDA preventing its industrial deployment. A high and stable selectivity to C_2 hydrocarbons (> 90% at ~2% conversion) in the non-oxidative methane coupling at moderate temperatures (600 – 700 °C) has also been achieved using ZSM-5 (Si/Al = 40) supported bimetallic Pt-Bi catalysts.[349]

3.3.6. Valorization of CO_2

Development of new technologies that utilize CO_2 as a renewable C_1 feedstock for the production of fuels and value-added chemicals has attracted great attention in the last years as a way to store renewable energy in chemical bonds while reducing net CO_2 emissions.[350, 351] Many studies were undertaken focusing in the hydrogenation of CO_2 to methanol, a valuable chemical and fuel. The design of efficient heterogeneous catalysts for CO_2 hydrogenation to methanol with reduced

RWGS activity (producing CO as side product) is thus a highly attractive and relevant research topic. In this line, interesting catalytic results have been obtained on a Cu-ZnO/H-ZSM-5 (Si/Al= 10.5) catalyst comprising small (~ 2.4 nm) CuO particles highly dispersed on H-ZSM-5 zeolite, as revealed by HRTEM.[352] A selectivity to methanol of 75% at 20% CO_2 conversion (productivity of 60 $g_{MeOH}\cdot g_{cat}^{-1}\cdot min^{-1}$) with almost no formation of CO was achieved with this catalyst at 22.5 bar and 250 °C.

From thermodynamic data, a reaction temperature in the range of 140 – 160 °C is required to achieve a CO_2 conversion of 30% at a pressure of 30 bar and a H_2/CO_2 molar ratio of 3.[353] Since known catalysts have relatively low methanol productivities under these conditions, the design of alternative catalysts with sufficient activity at such low temperatures is of high relevance. Preliminary DFT and surface science studies have positioned small metal clusters (e.g. Cu_5 and Ag_3) as highly promising catalysts for the low temperature CO_2 hydrogenation to methanol.[354-356] Moreover, DFT calculations indicated that the presence of Brønsted acid sites in the zeolite could modify the energetic reaction profile for CO_2 hydrogenation on isolated Ir_4 metal clusters located inside FAU cages.[357]

The inertness of CO_2 makes its direct hydrogenation to value-added higher (C_{2+}) hydrocarbons challenging. Bifunctional catalysts composed of reducible metal oxides (e.g. In_2O_3, ZnO, etc.) combined with acid zeolites can afford high selectivity to different types of C_{2+} hydrocarbons. On such tandem catalysts, defects on the surface of the reducible oxides catalyze the activation of CO_2 and H_2 while formation of the higher hydrocarbons occurs on the zeolite acid sites. As the C-C coupling reactions take place mainly in the confined space provided by the zeolite pores and cavities, the type of the formed hydrocarbons can be tailored by proper choice of the zeolite topology and acidity. For instance, while combining In_2O_3-ZrO_2 or ZnO-ZrO_2 with the small-pore weakly acidic H-SAPO-34 (CHA) enables the selective production of short-chain (C_2-C_4) olefins (selectivity > 80%),[358, 359] coupling In_2O_3 or Na-Fe_3O_4 with zeolite H-ZSM-5 having stronger acid sites yields gasoline-range hydrocarbons in selectivities approaching 80%.[360, 361]

3.3.7. Conversion of biomass-derived compounds

Great attention is currently paid to the valorization of biomass, a renewable and abundant carbon source, to fuels and chemicals as a feasible way to reduce CO_2 emissions. The conversion of biomass usually involves complex reaction networks that hamper the formation of specific products in high selectivity. In this respect, improved product selectivities may be attained using shape-selective metal-zeolite catalysts. For instance, the hydrogenation of furfural to furan was successfully accomplished at 250 °C with a furan selectivity of 98% at 91.3% furfural conversion on a core-shell Pd@silicalite-1 catalyst comprising ~6.9 nm Pd nanoparticles, where diffusional restrictions imposed by the microporous zeolite shell prevent the formation of bulkier products on the core Pd sites.[237] In a more recent work, these authors reported an outstanding furan selectivity of up to 99.9% at 100% conversion by increasing the hydrophilicity of the silicalite-1 zeolite through the incorporation of additional surface -OH groups during the synthesis of the core-shell catalyst (Pd@S-1-OH). [362] The higher hydrophilicity of the zeolite channels promoted the diffusion and desorption of furan and hindered that of the less polar furfural molecules, as corroborated by IR spectroscopy.

The production of 1,3-butadiene, an important industrial chemical used in the production of synthetic rubber, from bioethanol has attracted renewed interest as a sustainable alternative to the current oil refining route. Bicomponent Zn-Y clusters incorporated in the pores of silica materials are found active catalysts for the one-pot ethanol-to-butadiene conversion, where Zn^{2+} catalyzes the dehydrogenation of ethanol to acetaldehyde while Y^{3+} is active for the subsequent acetaldehyde condensation to 1,3-butadiene. In a recent work, it has been shown that, due to confinement effects, incorporation of the Zn-Y clusters inside de pores of a fully dealuminated *BEA zeolite improves the efficiency of the reaction, affording higher conversions and selectivities to 1,3-butadiene compared to analogous catalysts based on larger pore silicas (Figure 33).[363] Since most biomass-derived feedstocks contain significant amounts of water (e.g. crude bioethanol), the zeolite catalysts should also exhibit good water tolerance under reaction conditions. In this sense, a bimetallic zeolite catalyst comprising AuPd nanoparticles sizing ~3 nm encapsulated in a hydrophobic silicalite-1 shell (AuPd@S-1 core-shell catalyst) was shown to catalyze the conversion of bioethanol to acetic acid at 200 °C with 82% conversion and 94% selectivity in the presence of 90% of water.[364]

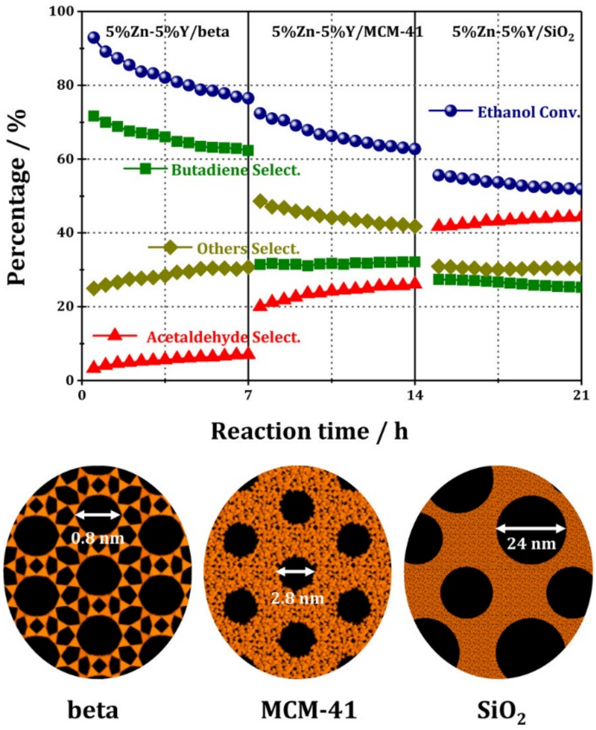

Figure 33. One-pot conversion of bioethanol to 1,3-butadiene catalyzed by Zn-Y clusters, showing the improvement achieved by confining the clusters in the smaller pores of *BEA zeolite compared to MCM-41 and SiO_2. Reaction conditions: T = 350 °C, WHSV = 1.3 h^{-1}. Adapted from ref. [363]

Much attention is also being paid to the valorization of glycerol formed in large amounts as by-product in the production of first-generation biodiesel. For instance, glycerol can be converted to allyl alcohol, a raw material in the production of plasticizers and other specialized products, by a multistep reaction involving its dehydration to 3-hydroxypropanal and then to acrolein on Brønsted acid sites followed by hydrogenation of acrolein to allyl alcohol on metal sites. The last step is challenging due to the preferential hydrogenation of C=C vs. C=O bonds on commonly used metal catalysts such as Pd, Pt, Ru and Rh. Silver and gold catalysts, in contrast, are much more efficient for the selective hydrogenation of C=O groups in the presence of C=C bonds. Therefore, an efficient catalyst for the conversion of glycerol to allyl alcohol has been recently reported on a multifunctional catalyst comprising Ag nanoparticles supported on an acidic hierarchical H-ZSM-5 zeolite, where the generation of mesopores in the zeolite by post-synthesis alkaline desilication endowed the catalyst with high stability by limiting coke formation.[365]

Additionally, removal of unselective Lewis acid sites associated to extra-framework Al species (formed during the desilication treatment) by acid washing improved the catalyst performance, achieving 20% selectivity to allylic alcohol at 80% glycerol conversion.

Finally, formation of H_2 via dehydrogenation of biomass-derived formic acid (FA) has been proposed as an attractive green alternative for H_2 storage applications. However, most of the heterogeneous catalysts so far investigated for this reaction suffer from poor recyclability and low thermal stability, making the development of efficient stable catalysts challenging. Notably, an stimulating H_2 formation rate of 696 $L_{H2}\cdot(g_{Pd}\cdot h)^{-1}$, corresponding to a theoretical power density of 940 $W\cdot(g_{Pd}\cdot h)^{-1}$, in the decomposition of FA has been recently reported for small (~1.5 nm) Pd nanoparticles stabilized in the channels of silicalite-1.[366] Moreover, the very low rate of CO formation (less 10 ppm within 2 min) makes this catalyst interesting for fuel cell applications. As shown by the authors in a more recent study, H_2 formation was remarkably improved by confining subnanometric hybrid Pd-$M(OH)_2$ (M= Ni, Co) clusters in the silicalite-1 pores (Figure 34a).[367] The location of such subnanometric bimetallic clusters inside the channels of the MFI zeolite was successfully proven by Cs-corrected HAADF-STEM images and energy-dispersive X-ray (EDX) spectral mapping (Figure 34b,c). Hydrogen formation rates as high as 1418 $L_{H2}\cdot(g_{Pd}\cdot h)^{-1}$, corresponding to a theoretical power density of 1915 $W\cdot(g_{Pd}\cdot h)^{-1}$, were attained on the bimetallic $0.8Pd0.2Ni(OH)_2$@S-1 catalyst, which is the highest H_2 formation rate so far reported for the heterogeneous decomposition of FA without additives. Moreover, the catalyst displayed excellent chemical stability up to 10 catalytic cycles. The high activity of the $0.8Pd0.2Ni(OH)_2$@S-1 catalyst was ascribed to a synergetic effect of different active sites in the Pd-$Ni(OH)_2$ interface of the bimetallic cluster that reduces the activation energy for FA decomposition, as suggested by DFT calculations, and to the presence of electron-rich Pd sites, evidenced by XAS, that promoted the C-H activation in the Pd-formate intermediate.

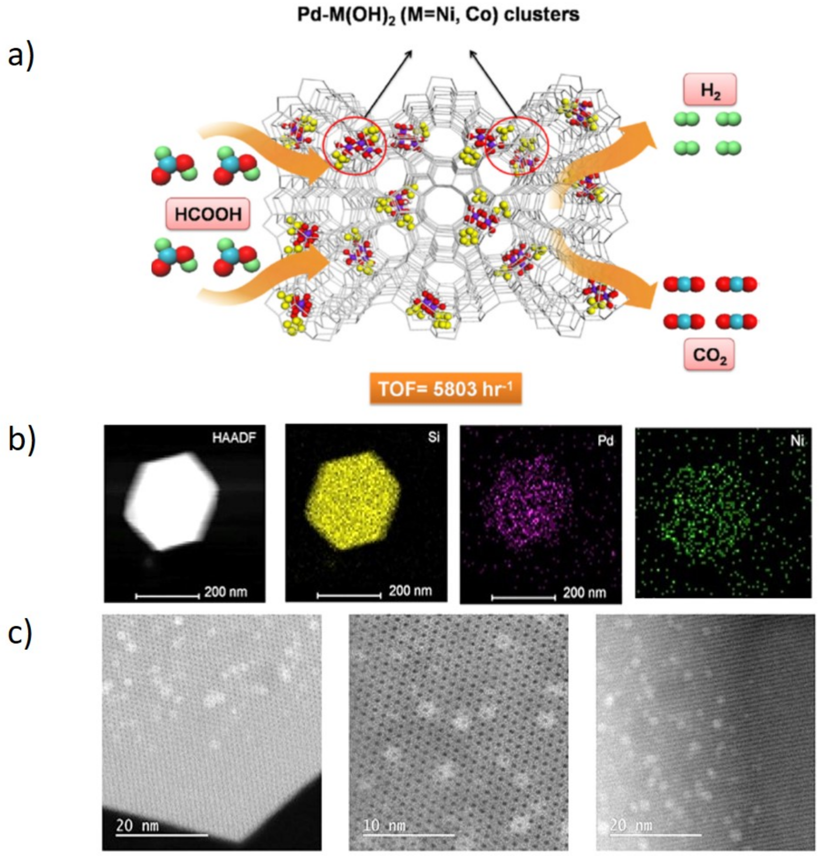

Figure 34. a) Representation of the dehydrogenation of FA on hybrid subnanometric bimetallic Pd-M$(OH)_2$ (M=Ni, Co) confined in MFI zeolite; b) HAADF-STEM image of the 0.8Pd0.2Ni$(OH)_2$@S-1 sample and the corresponding EDX mapping images for Si, Pd and Ni elements; c) Cs-corrected STEM images at different magnifications. Adapted from ref. [367]

4. Concluding remarks

The developments in the bottom-up (direct synthesis) and top-down (post-synthesis) approaches for isomorphous substitution in crystalline microporous materials resulted in a number of small-, medium- and large-pore zeolites possessing Al, B, Ga, Fe, Ti, Sn and other heteroelements at framework positions. Moreover, recent advances in the preparation of extra-large pore, layered (2D), nanocrystalline, and hierarchical micro-mesoporous zeolites with the potential for incorporating active sites of different nature allow expanding the application of these materials to catalytic processes involving bulky molecules. The main parameters of such active sites determining the catalytic performance (type, strength, concentration, and distribution among different crystallographic positions) can be relatively easily tuned by adjusting the conditions of either direct hydrothermal or multistep post-synthesis isomorphous substitution.

Depending on the zeolite topology and the nature of heteroatom and charge compensating cation (proton, metal, or organic), the local environment of the heteroelement incorporated into the framework can deviate from ideal tetrahedral coordination to distorted tetrahedral or 3-coordinated near-tetrahedral coordination, influencing the thermal stability, strength and, consequently, the catalytic performance of the associated active site. The location, distribution, and local surrounding of acid sites, including the defectiveness of zeolite frameworks, can be tuned by varying the conditions of the synthetic method used. Moreover, the nature of the isomorphously incorporated atom can determine the phase selectivity of zeolite formation as well as the crystal morphology. Recent achievements in understanding the structure-directing ability of some heteroelements (in particular, Ge) and the influence of the nature and concentration of heteroelements on the crystallization kinetics permit the rational design of new zeolites, i.e. extra-large pore and nanocrystalline ones.

Although direct hydrothermal synthesis is the most common way towards isomorphously substituted zeolites with adjusted nature and concentration of active sites, the maximum concentration of incorporated heteroatoms (e.g. Sn, Ti or even Al) is often limited to values not always suitable for particular catalytic applications. Alternative post-synthesis isomorphous substitution by gas-, liquid- or solid-state treatments can be employed to expand those concentration limits without altering the zeolite structure. Among post-synthesis methods, isomorphous substitution of Ge in extra-large pore zeolites is beneficial for the preparation of hydrolytically stable catalysts with pore entrances larger than 12 T-atoms, one of the most challenging issues during the last decade. However, a high efficiency in the subsequent recovery of the extracted Ge is still required for a successful potential application of extra-large pore germanosilicates, even in small-scale catalytic processes.

While a significant progress in tailoring the nature, accessibility, and local structure of acid sites by isomorphous substitution in zeolite frameworks has been reached, there are no doubts that more attention has to be paid to the application of these materials in relevant catalytic processes. In particular, the development of one-pot processes comprising cascade reactions catalyzed by zeolites possessing active centres of different nature, e.g. acid and base, or acid and redox sites, is of high importance, especially in the synthesis of fine chemicals and conversion of biomass-derived compounds involving, in many cases, multistep processes.

In the case of zeolite-supported metal catalysts, the size of the metal species is one of the most critical factors determining their catalytic performance. Controlling the size of supported metal species is particularly challenging for small clusters, for which a high surface free energy makes them more prone to aggregate into larger metal species (i.e. nanoparticles). Although the stability of metal clusters significantly improves through their encapsulation inside the voids of conventional 3D zeolites, the development of new synthetic strategies enabling the incorporation of metal species with well-defined size and structure in zeolites and their effective stabilization under reaction conditions is a challenging task deserving further research. Sintering of metal nanoparticles, with sizes typically exceeding the size of micropores, may also be prevented or minimized through their encapsulation in core-shell or yolk-shell structures where the metal sites in the core nanoparticles are only accessed through the pores in the zeolite shell. Tuning the size of micropores and the adsorption properties (e.g. hydrophilicity/hydrophobicity) of the zeolite shell can be applied to prepare tailored metal-zeolite catalysts exhibiting outstanding substrate-size selectivity in a variety of hydrogenation and oxidation reactions. Moreover, metal nanoparticles can also be confined in the mesopores of hierarchical or nanosized zeolites, thus combining the benefits of an enhanced accessibility to the active sites with the shape selectivity inherent to the native micropores.

Coupling metal sites in the supported/confined metal species with zeolite acid sites enables the design of efficient multifunctional catalysts for diverse reactions. Examples of industrial relevance are the selective hydroisomerization of *n*-alkanes over bifunctional Pt/H-zeolites (metal + Brønsted acid sites) and the selective hydrogenation of α,β-unsaturated aldehydes to their corresponding unsaturated alcohols on bifunctional Pt/Sn-*BEA catalysts (metal + Lewis acid sites).

An aspect deserving special attention is the dynamic behaviour of metal species under specific reactive atmospheres. For instance, while Pt nanoparticles in Pt-CHA zeolites can re-disperse into clusters and/or single atoms under oxidizing atmospheres, the small metal species transform again into nanoparticles under reducing conditions. As metal entities of different size typically display distinct reactivity, such interconversion of metal species in response to changing environments might be advantageously used to design metal-zeolite composites with tailored catalytic properties. At the same time, however, it makes the elucidation of the true nature and functioning of the active metal species in the *working* catalysts more intricate. The recent application of advanced *in situ* spectroscopies and imaging tools with enhanced resolution at different scales under *operando* conditions complemented with theoretical (DFT) studies has revealed very valuable in that respect, stressing the need to perform further studies in this line to shed more light on these fundamental issues.

Finally, the unique reactivity offered by zeolite-confined small metal clusters of defined size, structure, and composition may lead to new catalytic materials for emerging sustainable applications, such as the valorization of biomass and biomass-derived compounds and the soft conversion of relatively inert molecules like CH_4 and CO_2, two potent greenhouse gases, to added-value products. Nonetheless, further research efforts are needed in these areas to significantly improve the product yields and to demonstrate the viability of the processes under industrial conditions.

Conflicts of interest

There are no conflicts of interest to declare.

Acknowledgments

MS and MO acknowledge Primus Research Program of the Charles University project number PRIMUS/17/SCI/22 “Soluble zeolites” and OP VVV “Excellent Research Teams” project No.CZ.02.1.01/0.0/0.0/15_003/0000417– CUCAM. PC and AM acknowledge financial support by the Spanish government (MINECO) through the “Severo Ochoa Program” (SEV-2016-0683) and ENE2014-5761-R project.

References

1. J. M. Thomas and K. D. M. Harris, *Energy Environ. Sci.*, 2016, **9**, 687-708.
2. A. Navrotsky, *Structure and Bonding in crystals*, Elsevier, 2012.
3. N. N. Eremin, R. A. Talis and V. S. Urusov, *Crystallogr. Rep.*, 2008, **53**, 755-763.
4. J. Čejka, A. Corma and S. I. Zones, eds., *Zeolites and Catalysis: Synthesis, Reactions and Applications*, Wiley, 2010.
5. J. Čejka and R. E. Morris, *Zeolites in Catalysis: Properties and Applications*, Royal Society of Chemistry, 2017.
6. E. T. C. Vogt and B. M. Weckhuysen, *Chem. Soc. Rev.*, 2015, **44**, 7342-7370.
7. D. C. Koningsberger and J. T. Miller, *Catal. Lett.*, 1994, **29**, 77-90.
8. J. A. van Bokhoven and C. Lamberti, *Coord. Chem. Rev.*, 2014, **277**, 275-290.

9. B. Hu, N. M. Schweitzer, G. Zhang, S. J. Kraft, D. J. Childers, M. P. Lanci, J. T. Miller and A. S. Hock, *ACS Catal.*, 2015, **5**, 3494-3503.
10. K. A. Al-Majnouni, N. D. Hould, W. W. Lonergan, D. G. Vlachos and R. F. Lobo, *J. Phys. Chem. C*, 2010, **114**, 19395-19405.
11. L. Regli, C. Lamberti, C. Busco, A. Zecchina, C. Prestipino, K. P. Lillerud, S. I. Zones and S. Bordiga, in *Stud. Surf. Sci. Catal.*, eds. Z. G. J. C. Ruren Xu and Y. Wenfu, Elsevier, 2007, vol. 170, pp. 585-593.
12. H. Li, D. Zhou, D. Tian, C. Shi, U. Müller, M. Feyen, B. Yilmaz, H. Gies, F.-S. Xiao, D. De Vos, T. Yokoi, T. Tatsumi, X. Bao and W. Zhang, *ChemPhysChem*, 2014, **15**, 1700-1707.
13. Y. J. Fang, X. F. Su, X. F. Bai, W. Wu, G. L. Wang, L. F. Xiao and A. R. Yu, *J. Energ. Chem.*, 2017, **26**, 768-775.
14. A. G. Wang, D. Austin, A. Karmakar, G. M. Bernard, V. K. Michaelis, M. M. Yung, H. B. Zeng and H. Song, *ACS Catal.*, 2017, **7**, 3681-3692.
15. L. L. Li, Q. L. Meng, J. J. Wen, J. G. Wang, G. M. Tu, C. H. Xu, F. M. Zhang, Y. J. Zhong, W. D. Zhu and Q. Xiao, *Microporous Mesoporous Mater.*, 2016, **227**, 252-257.
16. F. Gao, Y. Zheng, R. K. Kukkadapu, Y. L. Wang, E. D. Walter, B. Schwenzer, J. Szanyi and C. H. F. Peden, *ACS Catal.*, 2016, **6**, 2939-2954.
17. P. F. Xie, Y. J. Luo, Z. Ma, C. Y. Huang, C. X. Miao, Y. H. Yue, W. M. Hua and Z. Gao, *J. Catal.*, 2015, **330**, 311-322.
18. J. Čejka and B. Wichterlova, *Catal. Rev. - Sci. Eng.*, 2002, **44**, 375-421.
19. M. V. Shamzhy, O. V. Shvets, M. V. Opanasenko, P. S. Yaremov, L. G. Sarkisyan, P. Chlubna, A. Zukal, V. R. Marthala, M. Hartmann and J. Čejka, *J. Mater. Chem.*, 2012, **22**, 15793-15803.
20. J. Meeprasert, S. Jungsuttiwong and S. Namuangruk, *Microporous Mesoporous Mater.*, 2013, **175**, 99-106.
21. S. Jungsuttiwong, J. Lomratsiri and J. Limtrakul, *Int. J. Quantum Chem.*, 2011, **111**, 2275-2282.
22. L. Kang, W. Deng, T. Zhang, Z. Liu and K.-L. Han, *Microporous Mesoporous Mater.*, 2008, **115**, 261-266.
23. A. J. Jones and E. Iglesia, *ACS Catal.*, 2015, **5**, 5741-5755.
24. M. Rybicki and J. Sauer, *Phys. Chem. Chem. Phys.*, 2015, **17**, 27873-27882.
25. J. Sauer, *Faraday Discuss.*, 2016, **188**, 227-234.
26. S. Bordiga, F. Bonino, A. Damin and C. Lamberti, *Phys. Chem. Chem. Phys.*, 2007, **9**, 4854-4878.
27. S. R. Bare, S. D. Kelly, W. Sinkler, J. J. Low, F. S. Modica, S. Valencia, A. Corma and L. T. Nemeth, *J. Am. Chem. Soc.*, 2005, **127**, 12924-12932.
28. J. To, A. A. Sokol, S. A. French and C. R. A. Catlow, *J. Phys. Chem. C*, 2007, **111**, 14720-14731.
29. V. L. Sushkevich, D. Palagin and I. I. Ivanova, *ACS Catal.*, 2015, **5**, 4833-4836.
30. M. Moliner, *Dalton Trans.*, 2014, **43**, 4197-4208.
31. G. Yang, L. Zhou and X. Han, *J. Mol. Catal. A: Chem.*, 2012, **363-364**, 371-379.
32. H. Li, J. Wang, D. Zhou, D. Tian, C. Shi, U. Müller, M. Feyen, H. Gies, F.-S. Xiao, D. De Vos, T. Yokoi, X. Bao and W. Zhang, *Microporous Mesoporous Mater.*, 2015, **218**, 160-166.
33. Y. G. Kolyagin, A. V. Yakimov, S. Tolborg, P. N. R. Vennestrøm and I. I. Ivanova, *J. Phys. Chem. Lett.*, 2016, **7**, 1249-1253.
34. J. D. Lewis, S. Van de Vyver, A. J. Crisci, W. R. Gunther, V. K. Michaelis, R. G. Griffin and Y. Román-Leshkov, *ChemSusChem*, 2014, **7**, 2255-2265.
35. J. Jiang, J. Yu and A. Corma, *Angew. Chem., Int. Ed.*, 2010, **49**, 3120-3145.
36. J. X. Jiang, J. L. Jorda, M. J. Diaz-Cabanas, J. H. Yu and A. Corma, *Angew. Chem., Int. Ed.*, 2010, **49**, 4986-4988.
37. S. Mintova, M. Jaber and V. Valtchev, *Chem. Soc. Rev.*, 2015, **44**, 7207-7233.
38. V. Valtchev and L. Tosheva, *Chem. Rev. (Washington, DC, U. S.)*, 2013, **113**, 6734-6760.
39. M. Choi, K. Na, J. Kim, Y. Sakamoto, O. Terasaki and R. Ryoo, *Nature*, 2009, **461**, 246-249.

40. P. Eliášová, M. Opanasenko, P. S. Wheatley, M. Shamzhy, M. Mazur, P. Nachtigall, W. J. Roth, R. E. Morris and J. Čejka, *Chem. Soc. Rev.*, 2015, **44**, 7177-7206.
41. N. Chu, J. Wang, Y. Zhang, J. Yang, J. Lu and D. Yin, *Chem. Mater.*, 2010, **22**, 2757-2763.
42. B. Li, Z. Hu, B. Kong, J. Wang, W. Li, Z. Sun, X. Qian, Y. Yang, W. Shen, H. Xu and D. Zhao, *Chem. Sci.*, 2014, **5**, 1565-1573.
43. A. G. Machoke, A. M. Beltrán, A. Inayat, B. Winter, T. Weissenberger, N. Kruse, R. Güttel, E. Spiecker and W. Schwieger, *Adv. Mater.*, 2015, **27**, 1066-1070.
44. M. Moliner, F. Rey and A. Corma, *Angew. Chem., Int. Ed.*, 2013, **52**, 13880-13889.
45. A. Aerts, C. E. A. Kirschhock and J. A. Martens, *Chem. Soc. Rev.*, 2010, **39**, 4626-4642.
46. J. D. Epping and B. F. Chmelka, *Curr. Opin. Colloid Interface Sci.*, 2006, **11**, 81-117.
47. B. B. Schaack, W. Schrader and F. Schüth, *Chem. Eur. J.*, 2009, **15**, 5920-5925.
48. B. B. Schaack, W. Schrader and F. Schüth, *Angew. Chem., Int. Ed.*, 2008, **47**, 9092-9095.
49. I. H. Lim, W. Schrader and F. Schüth, *Microporous Mesoporous Mater.*, 2013, **166**, 20-36.
50. C. S. Cundy and P. A. Cox, *Microporous Mesoporous Mater.*, 2005, **82**, 1-78.
51. R. E. Fletcher, S. L. Ling and B. Slater, *Chem. Sci.*, 2017, **8**, 7483-7491.
52. J. X. Jiang, Y. F. Yun, X. D. Zou, J. L. Jorda and A. Corma, *Chem. Sci.*, 2015, **6**, 480-485.
53. B. B. Schaack, W. Schrader, A. Corma and F. Schüth, *Chem. Mater.*, 2009, **21**, 4448-4453.
54. X. L. Liu, U. Ravon and A. Tuel, *Chem. Mater.*, 2011, **23**, 5052-5057.
55. P. S. Niphadkar, N. P. Tangale, P. N. Joshi and S. V. Awate, *Microporous Mesoporous Mater.*, 2013, **182**, 73-80.
56. S. V. Awate, P. N. Joshi, V. P. Shiralkar and A. N. Kotasthane, *J. Inclusion Phenom.*, 1992, **13**, 207-218.
57. M. Moliner and A. Corma, *Microporous Mesoporous Mater.*, 2014, **189**, 31-40.
58. C. C. Freyhardt, M. Tsapatsis, R. F. Lobo, K. J. Balkus Jr and M. E. Davis, *Nature*, 1996, **381**, 295.
59. P. Wagner, M. Yoshikawa, K. Tsuji, M. E. Davis, P. Wagner, M. Lovallo and M. Taspatsis, *Chem. Commun. (Cambridge, U. K.)*, 1997, 2179-2180.
60. S. I. Zones, *Microporous Mesoporous Mater.*, 2011, **144**, 1-8.
61. K. Qian, J. Y. Li, J. X. Jiang, Z. Q. Liang, J. H. Yu and R. R. Xu, *Microporous Mesoporous Mater.*, 2012, **164**, 88-92.
62. J. L. Paillaud, B. Harbuzaru, J. Patarin and N. Bats, *Science*, 2004, **304**, 990-992.
63. A. Corma, M. J. Diaz-Cabanas, F. Rey, S. Nicolopoulus and K. Boulahya, *Chem. Commun. (Cambridge, U. K.)*, 2004, 1356-1357.
64. O. V. Shvets, M. V. Shamzhy, P. S. Yaremov, Z. Musilová, D. Procházková and J. Čejka, *Chem. Mater.*, 2011, **23**, 2573-2585.
65. M. Shamzhy, O. V. Shvets, M. V. Opanasenko, D. Procházková, P. Nachtigall and J. Čejka, *Adv. Porous Mater*, 2013, **1**, 103-113.
66. A. Burton, S. Elomari, C.-Y. Chen, R. C. Medrud, I. Y. Chan, L. M. Bull, C. Kibby, T. V. Harris, S. I. Zones and E. S. Vittoratos, *Chem. Eur. J.*, 2003, **9**, 5737-5748.
67. K. G. Strohmaier and D. E. W. Vaughan, *J. Am. Chem. Soc.*, 2003, **125**, 16035-16039.
68. A. Corma, M. J. Díaz-Cabañas, J. L. Jordá, C. Martínez and M. Moliner, *Nature*, 2006, **443**, 842.
69. J. L. Sun, C. Bonneau, A. Cantin, A. Corma, M. J. Diaz-Cabanas, M. Moliner, D. L. Zhang, M. R. Li and X. D. Zou, *Nature*, 2009, **458**, 1154-1157.
70. A. Corma, M. J. Diaz-Cabanas, J. Jiang, M. Afeworki, D. L. Dorset, S. L. Soled and K. G. Strohmaier, *Proc. Natl. Acad. Sci. USA*, 2010, **107**, 13997-14002.
71. J. X. Jiang, J. L. Jorda, J. H. Yu, L. A. Baumes, E. Mugnaioli, M. J. Diaz-Cabanas, U. Kolb and A. Corma, *Science*, 2011, **333**, 1131-1134.
72. Y. Yun, M. Hernandez, W. Wan, X. Zou, J. L. Jorda, A. Cantin, F. Rey and A. Corma, *Chem. Commun. (Cambridge, U. K.)*, 2015, **51**, 7602-7605.
73. F.-J. Chen, Y. Xu and H.-B. Du, *Angew. Chem., Int. Ed.*, 2014, **53**, 9592-9596.

74. C. Jo, S. Lee, S. J. Cho and R. Ryoo, *Angew. Chem.*, 2015, **127**, 12996-12999.
75. B. W. Boal, M. W. Deem, D. Xie, J. H. Kang, M. E. Davis and S. I. Zones, *Chem. Mater.*, 2016, **28**, 2158-2164.
76. Z. H. Gao, F. J. Chen, L. Xu, L. Sun, Y. Xu and H. B. Du, *Chem. Eur. J.*, 2016, **22**, 14367-14372.
77. D. S. Firth, S. A. Morris, P. S. Wheatley, S. E. Russell, A. M. Z. Slawin, D. M. Dawson, A. Mayoral, M. Opanasenko, M. Položij, J. Čejka, P. Nachtigall and R. E. Morris, *Chem. Mater.*, 2017, **29**, 5605-5611.
78. K. Qian, Y. Wang, Z. Liang and J. Li, *RSC Adv.*, 2015, **5**, 63209-63214.
79. P. S. Petkov, H. A. Aleksandrov, V. Valtchev and G. N. Vayssilov, *Chem. Mater.*, 2012, **24**, 2509-2518.
80. K. J. Balkus, A. G. Gabrielov and S. I. Zones, in *Stud. Surf. Sci. Catal.*, eds. L. Bonneviot and S. Kaliaguine, Elsevier, 1995, vol. 97, pp. 519-525.
81. J. Přech, M. Kubů and J. Čejka, *Catal. Today*, 2014, **227**, 80-86.
82. J. Přech and J. Čejka, *Catal. Today*, 2016, **277**, 2-8.
83. N. L. Chauhan, J. Das, R. V. Jasra, P. A. Parikh and Z. V. P. Murthy, *Mater. Lett.*, 2012, **74**, 115-117.
84. N. Ren, J. Bronić, B. Subotić, Y.-M. Song, X.-C. Lv and Y. Tang, *Microporous Mesoporous Mater.*, 2012, **147**, 229-241.
85. A. Petushkov, S. Yoon and S. C. Larsen, *Microporous Mesoporous Mater.*, 2011, **137**, 92-100.
86. L. H. Vieira, K. T. G. Carvalho, E. A. Urquieta-González, S. H. Pulcinelli, C. V. Santilli and L. Martins, *J. Mol. Catal. A: Chem.*, 2016, **422**, 148-157.
87. T. Taniguchi, Y. Nakasaka, K. Yoneta, T. Tago and T. Masuda, *Microporous Mesoporous Mater.*, 2016, **224**, 68-74.
88. S. Tolborg, A. Katerinopoulou, D. D. Falcone, I. Sadaba, C. M. Osmundsen, R. J. Davis, E. Taarning, P. Fristrup and M. S. Holm, *J. Mater. Chem. A*, 2014, **2**, 20252-20262.
89. E. P. Ng, D. Chateigner, T. Bein, V. Valtchev and S. Mintova, *Science*, 2012, **335**, 70-73.
90. Y. Huang, K. Wang, D. Dong, D. Li, M. R. Hill, A. J. Hill and H. Wang, *Microporous Mesoporous Mater.*, 2010, **127**, 167-175.
91. G. Majano, A. Darwiche, S. Mintova and V. Valtchev, *Ind. Eng. Chem. Res.*, 2009, **48**, 7084-7091.
92. N. Ren, J. Bronić, B. Subotić, X.-C. Lv, Z.-J. Yang and Y. Tang, *Microporous Mesoporous Mater.*, 2011, **139**, 197-206.
93. G. Majano, L. Delmotte, V. Valtchev and S. Mintova, *Chem. Mater.*, 2009, **21**, 4184-4191.
94. G. R. Chen, Q. M. Sun and J. H. Yu, *Chem. Commun. (Cambridge, U. K.)*, 2017, **53**, 13328-13331.
95. H. Y. Chen, J. Wydra, X. Y. Zhang, P. S. Lee, Z. P. Wang, W. Fan and M. Tsapatsis, *J. Am. Chem. Soc.*, 2011, **133**, 12390-12393.
96. J. Kim, C. Jo, S. Lee and R. Ryoo, *J. Mater. Chem. A*, 2014, **2**, 11905-11912.
97. Z. Wang, L. Xu, J.-g. Jiang, Y. Liu, M. He and P. Wu, *Microporous Mesoporous Mater.*, 2012, **156**, 106-114.
98. D. Liu, A. Bhan, M. Tsapatsis and S. Al Hashimi, *ACS Catal.*, 2011, **1**, 7-17.
99. H. Chen, J. Wydra, X. Zhang, P.-S. Lee, Z. Wang, W. Fan and M. Tsapatsis, *J. Am. Chem. Soc.*, 2011, **133**, 12390-12393.
100. H. S. Cho and R. Ryoo, *Microporous Mesoporous Mat.*, 2012, **151**, 107-112.
101. H. J. Cho, P. Dornath and W. Fan, *ACS Catal.*, 2014, **4**, 2029-2037.
102. M. E. Leonowicz, J. A. Lawton, S. L. Lawton and M. K. Rubin, *Science*, 1994, **264**, 1910-1913.
103. W. J. Roth, P. Nachtigall, R. E. Morris and J. Čejka, *Chem. Rev. (Washington, DC, U. S.)*, 2014, **114**, 4807–4837.
104. K. Na, M. Choi, W. Park, Y. Sakamoto, O. Terasaki and R. Ryoo, *J. Am. Chem. Soc.*, 2010, **132**, 4169-4177.

105. Y. Kim, J.-C. Kim, C. Jo, T.-W. Kim, C.-U. Kim, S.-Y. Jeong and H.-J. Chae, *Microporous Mesoporous Mater.*, 2016, **222**, 1-8.
106. W. Park, D. Yu, K. Na, K. E. Jelfs, B. Slater, Y. Sakamoto and R. Ryoo, *Chem. Mater.*, 2011, **23**, 5131-5137.
107. Y. Kim, K. Kim and R. Ryoo, *Chem. Mater.*, 2017, **29**, 1752-1757.
108. K. Na, C. Jo, J. Kim, K. Cho, J. Jung, Y. Seo, R. J. Messinger, B. F. Chmelka and R. Ryoo, *Science*, 2011, **333**, 328-332.
109. C. Jo, K. Cho, J. Kim and R. Ryoo, *Chem. Commun. (Cambridge, U. K.)*, 2014, **50**, 4175-4177.
110. K. Na, C. Jo, J. Kim, W.-S. Ahn and R. Ryoo, *ACS Catal.*, 2011, **1**, 901-907.
111. H. Y. Luo, L. Bui, W. R. Gunther, E. Min and Y. Román-Leshkov, *ACS Catal.*, 2012, **2**, 2695-2699.
112. J. G. Wang, L. Xu, K. Zhang, H. G. Peng, H. H. Wu, J. G. Jiang, Y. M. Liu and P. Wu, *J. Catal.*, 2012, **288**, 16-23.
113. M. V. Opanasenko, W. J. Roth and J. Čejka, *Catal. Sci. Technol.*, 2016, **6**, 2467-2484.
114. A. Corma, V. Fornes, S. B. Pergher, T. L. M. Maesen and J. G. Buglass, *Nature*, 1998, **396**, 353.
115. A. Corma, U. Diaz, M. E. Domine and V. Fornés, *Angew. Chem. Int. Ed.*, 2000, **39**, 1499-1501.
116. A. Corma, V. Fornés and U. Díaz, *Chem. Commun. (Cambridge, U. K.)*, 2001, 2642-2643.
117. A. Corma, V. Fornés, J. Martínez-Triguero and S. B. Pergher, *J. Catal.*, 1999, **186**, 57-63.
118. X. Zhang, D. Liu, D. Xu, S. Asahina, K. A. Cychosz, K. V. Agrawal, Y. Al Wahedi, A. Bhan, S. Al Hashimi, O. Terasaki, M. Thommes and M. Tsapatsis, *Science*, 2012, **336**, 1684-1687.
119. L. Ren, Q. Guo, P. Kumar, M. Orazov, D. Xu, S. M. Alhassan, K. A. Mkhoyan, M. E. Davis and M. Tsapatsis, *Angew. Chem., Int. Ed.*, 2015, **54**, 10848-10851.
120. C. Jo, W. Park and R. Ryoo, *Microporous Mesoporous Mat.*, 2017, **239**, 19-27.
121. J.-B. Koo, N. Jiang, S. Saravanamurugan, M. Bejblová, Z. Musilová, J. Čejka and S.-E. Park, *J. Catal.*, 2010, **276**, 327-334.
122. X. Wei and P. G. Smirniotis, *Microporous Mesoporous Mat.*, 2006, **89**, 170-178.
123. K. Egeblad, M. Kustova, S. K. Klitgaard, K. Zhu and C. H. Christensen, *Microporous Mesoporous Mat.*, 2007, **101**, 214-223.
124. M. Y. Kustova, P. Hasselriis and C. H. Christensen, *Catal. Lett.*, 2004, **96**, 205-211.
125. C. Xue, T. Xu, J. Zheng, J. Wang, Z. Zhang, X. Hao, A. Abudula and G. Guan, *Mater. Lett.*, 2015, **154**, 55-59.
126. M. Choi, H. S. Cho, R. Srivastava, C. Venkatesan, D.-H. Choi and R. Ryoo, *Nat. Mater.*, 2006, **5**, 718.
127. D. P. Serrano, J. Aguado, J. M. Escola, J. M. Rodriguez and A. Peral, *J. Mater. Chem.*, 2008, **18**, 4210-4218.
128. R. R. Mukti, H. Hirahara, A. Sugawara, A. Shimojima and T. Okubo, *Langmuir*, 2010, **26**, 2731-2735.
129. V. Valtchev, G. Majano, S. Mintova and J. Pérez-Ramírez, *Chem. Soc. Rev.*, 2013, **42**, 263-290.
130. D. Verboekend and J. Perez-Ramirez, *Catal. Sci. Tech.*, 2011, **1**, 879-890.
131. E. Senderov, I. Halasz and D. H. Olson, *Microporous Mesoporous Mater.*, 2014, **186**, 94-100.
132. V. I. Kasneryk, M. V. Shamzhy, M. V. Opanasenko and J. Čejka, *J. Energ. Chem.*, 2016, **25**, 318-326.
133. T. Ennaert, J. Van Aelst, J. Dijkmans, R. De Clercq, W. Schutyser, M. Dusselier, D. Verboekend and B. F. Sels, *Chem. Soc. Rev.*, 2016, **45**, 584-611.
134. P. Li, G. Liu, H. Wu, Y. Liu, J.-g. Jiang and P. Wu, *J. Phys. Chem. C*, 2011, **115**, 3663-3670.
135. J. Jin, X. Ye, Y. Li, Y. Wang, L. Li, J. Gu, W. Zhao and J. Shi, *Dalton Trans.*, 2014, **43**, 8196-8204.
136. J. Dijkmans, J. Demol, K. Houthoofd, S. Huang, Y. Pontikes and B. Sels, *J. Catal.*, 2015, **330**, 545-557.
137. J. Dijkmans, M. Dusselier, W. Janssens, M. Trekels, A. Vantomme, E. Breynaert, C. Kirschhock and B. F. Sels, *ACS Catal.*, 2016, **6**, 31-46.

138. W. N. P. van der Graaff, G. Li, B. Mezari, E. A. Pidko and E. J. M. Hensen, *ChemCatChem*, 2015, **7**, 1152-1160.
139. F. F. Guan, T. T. Ma, X. Yuan, H. Y. Zeng and J. Wu, *Catal. Lett.*, 2018, **148**, 443-453.
140. J. Wang, K. Okumura, S. Jaenicke and G.-K. Chuah, *Appl. Catal. A, Gen.*, 2015, **493**, 112-120.
141. V. L. Sushkevich and Ivanova, II, *Chemsuschem*, 2016, **9**, 2216-2225.
142. Y. Yang, J. Ding, C. Xu, W. Zhu and P. Wu, *J. Catal.*, 2015, **325**, 101-110.
143. C. Hammond, S. Conrad and I. Hermans, *Angew. Chem., Int. Ed.*, 2012, **51**, 11736-11739.
144. P. Wolf, C. Hammond, S. Conrad and I. Hermans, *Dalton Trans.*, 2014, **43**, 4514-4519.
145. J. Dijkmans, M. Dusselier, D. Gabriëls, K. Houthoofd, P. C. M. M. Magusin, S. Huang, Y. Pontikes, M. Trekels, A. Vantomme, L. Giebeler, S. Oswald and B. F. Sels, *ACS Catal.*, 2015, **5**, 928-940.
146. T. J. Schwartz, S. M. Goodman, C. M. Osmundsen, E. Taarning, M. D. Mozuch, J. Gaskell, D. Cullen, P. J. Kersten and J. A. Dumesic, *ACS Catal.*, 2013, **3**, 2689-2693.
147. H. P. Winoto, B. S. Ahn and J. Jae, *J. Ind. Eng. Chem.*, 2016, **40**, 62-71.
148. S. Song, L. Di, G. Wu, W. Dai, N. Guan and L. Li, *Appl. Catal., B*, 2017, **205**, 393-403.
149. D. Padovan, A. Al-Nayili and C. Hammond, *Green Chem.*, 2017, **19**, 2846-2854.
150. P. Y. Dapsens, C. Mondelli and J. Perez-Ramirez, *New J. Chem.*, 2016, **40**, 4136-4139.
151. P. Y. Dapsens, C. Mondelli, J. Jagielski, R. Hauert and J. Perez-Ramirez, *Catal. Sci. Tech.*, 2014, **4**, 2302-2311.
152. A. Al-Nayili, K. Yakabi and C. Hammond, *J. Mater. Chem. A*, 2016, **4**, 1373-1382.
153. B. Tang, W. Dai, X. Sun, G. Wu, N. Guan, M. Hunger and L. Li, *Green Chem.*, 2015, **17**, 1744-1755.
154. S. I. Zones, A. Benin, S.-J. Hwang, D. Xie, S. Elomari and M.-F. Hsieh, *J. Am. Chem. Soc.*, 2014, **136**, 1462-1471.
155. S. I. Zones, C. Y. Chen, A. Benin and S. J. Hwang, *J. Catal.*, 2013, **308**, 213-225.
156. S. Smeets, L. B. McCusker, C. Baerlocher, D. Xie, C.-Y. Chen and S. I. Zones, *J. Am. Chem. Soc.*, 2015, **137**, 2015-2020.
157. C.-Y. Chen and S. I. Zones, in *Zeolites and Catalysis*, eds. J. Čejka, A. Corma and S. I. Zones, Wiley-VCH, Verlag, 2010, pp. 155-170.
158. H. T. T. Tong and H. Koller, *Microporous Mesoporous Mater.*, 2012, **148**, 80-87.
159. J. Přech, D. Vitvarová, L. Lupínková, M. Kubů and J. Čejka, *Microporous Mesoporous Mater.*, 2015, **212**, 28-34.
160. Q. Guo, F. T. Fan, E. A. Pidko, W. N. P. van der Graaff, Z. C. Feng, C. Li and E. J. M. Hensen, *Chemsuschem*, 2013, **6**, 1352-1356.
161. L. Burel, N. Kasian and A. Tuel, *Angew. Chem., Int. Ed.*, 2014, **53**, 1360-1363.
162. H. Xu, J. G. Jiang, B. T. Yang, L. Zhang, M. Y. He and P. Wu, *Angew. Chem., Int. Ed.*, 2014, **53**, 1355-1359.
163. F. Gao, M. Jaber, K. Bozhilov, A. Vicente, C. Fernandez and V. Valtchev, *J. Am. Chem. Soc.*, 2009, **131**, 16580-16586.
164. M. V. Shamzhy, P. Eliašová, D. Vitvarová, M. V. Opanasenko, D. S. Firth and R. E. Morris, *Chem. Eur. J.*, 2016, **22**, 17377-17386.
165. M. El-Roz, L. Lakiss, A. Vicente, K. N. Bozhilov, F. Thibault-Starzyk and V. Valtchev, *Chem. Sci.*, 2014, **5**, 68-80.
166. P. A. Kots, V. L. Sushkevich, O. A. Tyablikov and I. I. Ivanova, *Microporous Mesoporous Mater.*, 2017, **243**, 186-192.
167. M. Shamzhy, M. Opanasenko, Y. Tian, K. Konysheva, O. Shvets, R. E. Morris and J. Čejka, *Chem. Mater.*, 2014, **26**, 5789-5798.
168. M. V. Shamzhy, M. V. Opanasenko, F. S. D. Ramos, L. Brabec, M. Horacek, M. Navarro-Rojas, R. E. Morris, H. D. Pastore and J. Čejka, *Catal. Sci. Tech.*, 2015, **5**, 2973-2984.
169. P. Chlubná-Eliášová, Y. Tian, A. B. Pinar, M. Kubů, J. Čejka and R. E. Morris, *Angew. Chem., Int. Ed.*, 2014, **53**, 7042-7052.

170. V. Kasneryk, M. Shamzhy, M. Opanasenko, P. S. Wheatley, R. E. Morris and J. Čejka, *Dalton Trans.*, 2018, **47**, 3084-3092.
171. M. Shamzhy and F. S. D. Ramos, *Catal. Today*, 2015, **243**, 76-84.
172. V. Kasneryk, M. Opanasenko, M. Shamzhy, Z. Musilova, Y. S. Avadhut, M. Hartmann and J. Čejka, *J. Mater. Chem. A*, 2017, **5**, 22576-22587.
173. X. Liu, H. Xu, L. Zhang, L. Han, J. Jiang, P. Oleynikov, L. Chen and P. Wu, *ACS Catal.*, 2016, **6**, 8420-8431.
174. X. Liu, L. Zhang, H. Xu, J. Jiang, M. Peng and P. Wu, *Appl. Catal. A, Gen.*, 2018, **550**, 11-19.
175. Y. Seo, K. Cho, Y. Jung and R. Ryoo, *ACS Catal.*, 2013, **3**, 713-720.
176. S. Hu, J. Shan, Q. Zhang, Y. Wang, Y. Liu, Y. Gong, Z. Wu and T. Dou, *Appl. Catal. A, Gen.*, 2012, **445-446**, 215-220.
177. J.-C. Kim, T.-W. Kim, Y. Kim, R. Ryoo, S.-Y. Jeong and C.-U. Kim, *Appl. Catal., B*, 2017, **206**, 490-500.
178. M. V. Opanasenko, M. V. Shamzhy, C. Jo, R. Ryoo and J. Čejka, *ChemCatChem*, 2014, **6**, 1919-1927.
179. A. J. J. Koekkoek, W. Kim, V. Degirmenci, H. Xin, R. Ryoo and E. J. M. Hensen, *J. Catal.*, 2013, **299**, 81-89.
180. L. Q. Meng, X. C. Zhu and E. J. M. Hensen, *ACS Catal.*, 2017, **7**, 2709-2719.
181. C. Lee, S. Lee, W. Kim and R. Ryoo, *Catal. Today*, 2018, **303**, 143-149.
182. N. Simone, W. A. Carvalho, D. Mandelli and R. Ryoo, *J. Mol. Catal. A: Chem.*, 2016, **422**, 115-121.
183. J.-C. Kim, R. Ryoo, M. V. Opanasenko, M. V. Shamzhy and J. Čejka, *ACS Catal.*, 2015, **5**, 2596-2604.
184. T. W. Kim, S. Y. Kim, J. C. Kim, Y. Kim, R. Ryoo and C. U. Kim, *Appl. Catal., B*, 2016, **185**, 100-109.
185. J.-C. Kim, K. Cho and R. Ryoo, *Appl. Catal. A, Gen.*, 2014, **470**, 420-426.
186. H. S. Shin, M. Opanasenko, C. P. Cabello, R. Ryoo and J. Čejka, *Appl. Catal. A, Gen.*, 2017, **537**, 24-32.
187. Z. Qin, L. Lakiss, L. Tosheva, J. P. Gilson, A. Vicente, C. Fernandez and V. Valtchev, *Adv. Funct. Mater.*, 2014, **24**, 257-264.
188. M. Moliner, M. J. Díaz-Cabañas, V. Fornés, C. Martínez and A. Corma, *J. Catal.*, 2008, **254**, 101-109.
189. M. V. Shamzhy, O. V. Shvets, M. V. Opanasenko, L. Kurfiřtová, D. Kubička and J. Čejka, *ChemCatChem*, 2013, **5**, 1891-1898.
190. M. V. Shamzhy, C. Ochoa-Hernandez, V. I. Kasneryk, M. V. Opanasenko and M. Mazur, *Catal. Today*, 2016, **277**, 37-47.
191. T. Taniguchi, Y. Nakasaka, K. Yoneta, T. Tago and T. Masuda, *Catal. Lett.*, 2016, **146**, 666-676.
192. K. Y. Lee, S. W. Lee and S. K. Ihm, *Ind. Eng. Chem. Res.*, 2014, **53**, 10072-10079.
193. T. Taniguchi, K. Yoneta, S. Nakaoka, Y. Nakasaka, T. Yokoi, T. Tago and T. Masuda, *Catal. Lett.*, 2016, **146**, 442-451.
194. Z. J. Hu, H. B. Zhang, L. Wang, H. X. Zhang, Y. H. Zhang, H. L. Xu, W. Shen and Y. Tang, *Catal. Sci. Tech.*, 2014, **4**, 2891-2895.
195. F. Yaripour, Z. Shariatinia, S. Sahebdelfar and A. Irandoukht, *Microporous Mesoporous Mater.*, 2015, **203**, 41-53.
196. X. Su, G. Wang, X. Bai, W. Wu, L. Xiao, Y. Fang and J. Zhang, *Chem. Eng. J. (Lausanne)*, 2016, **293**, 365-375.
197. L. Q. Meng, X. C. Zhu, B. Mezari, R. Pestman, W. Wannapakdee and E. J. M. Hensen, *ChemCatChem*, 2017, **9**, 3942-3954.
198. Y. J. Ji, B. F. Shi, H. H. Yang and W. Yan, *Appl. Catal. A,Gen.*, 2017, **533**, 90-98.
199. N. Žilková, M. Shamzhy, O. Shvets and J. Čejka, *Catal. Today*, 2013, **204**, 22-29.

200. X. Yang, J. Bian, J. Huang, W. Xin, T. Lu, C. Chen, Y. Su, L. Zhou, F. Wang and J. Xu, *Green Chem.*, 2017, **19**, 692-701.
201. J. Dijkmans, D. Gabriels, M. Dusselier, F. de Clippel, P. Vanelderen, K. Houthoofd, A. Malfliet, Y. Pontikes and B. F. Sels, *Green Chem.*, 2013, **15**, 2777-2785.
202. A. Corma, V. Fornés, S. Iborra, M. a. Mifsud and M. Renz, *J. Catal.*, 2004, **221**, 67-76.
203. M. M. Antunes, S. Lima, P. Neves, A. L. Magalhães, E. Fazio, A. Fernandes, F. Neri, C. M. Silva, S. M. Rocha, M. F. Ribeiro, M. Pillinger, A. Urakawa and A. A. Valente, *J. Catal.*, 2015, **329**, 522-537.
204. M. M. Antunes, S. Lima, P. Neves, A. L. Magalhães, E. Fazio, F. Neri, M. T. Pereira, A. F. Silva, C. M. Silva, S. M. Rocha, M. Pillinger, A. Urakawa and A. A. Valente, *Appl. Catal., B*, 2016, **182**, 485-503.
205. M. M. Antunes, P. Neves, A. Fernandes, S. Lima, A. F. Silva, M. F. Ribeiro, C. M. Silva, M. Pillinger and A. A. Valente, *Catal. Sci. Tech.*, 2016, **6**, 7812-7829.
206. S. Vajda, M. J. Pellin, J. P. Greeley, C. L. Marshall, L. A. Curtiss, G. A. Ballentine, J. W. Elam, S. Catillon-Mucherie, P. C. Redfern, F. Mehmood and P. Zapol, *Nat. Mater.*, 2009, **8**, 213-216.
207. U. Heiz, A. Sanchez, S. Abbet and W. D. Schneider, *J. Am. Chem. Soc.*, 1999, **121**, 3214-3217.
208. J. M. Campelo, D. Luna, R. Luque, J. M. Marinas and A. A. Romero, *ChemSusChem*, 2009, **2**, 18-45.
209. R. J. White, R. Luque, V. L. Budarin, J. H. Clark and D. J. Macquarrie, *Chem. Soc. Rev.*, 2009, **38**, 481-494.
210. P. Munnik, P. E. de Jongh and K. P. de Jong, *Chem. Rev. (Washington, DC, U. S.)*, 2015, **115**, 6687-6718.
211. M. Wolters, L. J. W. van Grotel, T. M. Eggenhuisen, J. R. A. Sietsma, K. P. de Jong and P. E. de Jongh, *Catal. Today*, 2011, **163**, 27-32.
212. P. Munnik, M. Wolters, A. Gabrielsson, S. D. Pollington, G. Headdock, J. H. Bitter, P. E. de Jongh and K. P. de Jong, *J. Phys. Chem. C*, 2011, **115**, 14698-14706.
213. J. de Graaf, A. J. van Dillen, K. P. de Jong and D. C. Koningsberger, *J. Catal.*, 2001, **203**, 307-321.
214. A. J. van Dillen, R. J. A. M. Terörde, D. J. Lensveld, J. W. Geus and K. P. de Jong, *J. Catal.*, 2003, **216**, 257-264.
215. E. Behravesh, N. Kumar, Q. Balme, J. Roine, J. Salonen, A. Schukarev, J.-P. Mikkola, M. Peurla, A. Aho, K. Eränen, D. Y. Murzin and T. Salmi, *J. Catal.*, 2017, **353**, 223-238.
216. Y.-H. Chen, C.-Y. Mou and B.-Z. Wan, *Appl. Catal., B*, 2017, **218**, 506-514.
217. K. An and G. A. Somorjai, *Catal. Lett.*, 2015, **145**, 233-248.
218. K. Na, Q. Zhang and G. A. Somorjai, *J. Cluster Sci.*, 2014, **25**, 83-114.
219. M. Boutonnet and M. Sanchez-Dominguez, *Catal. Today*, 2017, **285**, 89-103.
220. M. Boutonnet, J. Kizling, P. Stenius and G. Maire, *Colloids Surf.*, 1982, **5**, 209-225.
221. M. Boutonnet, S. Lögdberg and E. Elm Svensson, *Curr. Opin. Colloid Interface Sci.*, 2008, **13**, 270-286.
222. S. Eriksson, U. Nylén, S. Rojas and M. Boutonnet, *Appl. Catal. A, Gen.*, 2004, **265**, 207-219.
223. R. Y. Parapat, V. Parwoto, M. Schwarze, B. Zhang, D. S. Su and R. Schomacker, *J. Mater. Chem.*, 2012, **22**, 11605-11614.
224. R. Y. Parapat, O. H. I. Saputra, A. P. Ang, M. Schwarze and R. Schomacker, *RSC Adv.*, 2014, **4**, 50955-50963.
225. T. Hanaoka, T. Miyazawa, K. Shimura and S. Hirata, *Chem. Eng. J. (Lausanne)*, 2015, **274**, 256-264.
226. A. Martínez and G. Prieto, *J. Catal.*, 2007, **245**, 470-476.
227. G. Prieto, A. Martínez, P. Concepción and R. Moreno-Tost, *J. Catal.*, 2009, **266**, 129-144.
228. S. Goel, Z. Wu, S. I. Zones and E. Iglesia, *J. Am. Chem. Soc.*, 2012, **134**, 17688-17695.
229. M. Choi, Z. Wu and E. Iglesia, *J. Am. Chem. Soc.*, 2010, **132**, 9129-9137.

230. L. Liu, U. Díaz, R. Arenal, G. Agostini, P. Concepción and A. Corma, *Nat. Mater.*, 2017, **16**, 132-138.

231. Z. Zhenchao, L. Yanlu, F. Mathias, M. Robert, M. Ulrich and Z. Weiping, *ChemCatChem*, 2018, **10**, 1-7.

232. J. Gu, Z. Zhang, P. Hu, L. Ding, N. Xue, L. Peng, X. Guo, M. Lin and W. Ding, *ACS Catal.*, 2015, **5**, 6893-6901.

233. C. Tian-Lu, K. Wen-Yu, Z. Wen-Bei, W. Hong-Hui, L. Xin-Hao and C. Jie-Sheng, *Angew. Chem., Int. Ed.*, 2016, **55**, 9178-9182.

234. L. Chang, L. Jian, Y. Shuliang, C. Changyan and S. Weiguo, *ChemCatChem*, 2016, **8**, 1279-1282.

235. A. B. Laursen, K. T. Højholt, L. F. Lundegaard, S. B. Simonsen, S. Helveg, F. Schüth, l. M. Pau, J. D. Grunwaldt, S. Kegnæs, C. H. Christensen and K. Egeblad, *Angew. Chem., Int. Ed.*, 2010, **49**, 3504-3507.

236. Z. Jian, W. Liang, S. Yi, W. Yanqin, G. B. C. and X. Feng-Shou, *Angew. Chem., Int. Ed.*, 2017, **56**, 9747-9751.

237. C. Wang, L. Wang, J. Zhang, H. Wang, J. P. Lewis and F.-S. Xiao, *J. Am. Chem. Soc.*, 2016, **138**, 7880-7883.

238. V. Dal Santo, M. Guidotti, R. Psaro, L. Marchese, F. Carniato and C. Bisio, *Proc. Royal Soc. A*, 2012, **468**, 1904-1926.

239. X. Zheng, M. N. D., N. G. T., S. W. F. and H. J. C., *ChemCatChem*, 2013, **5**, 1769-1771.

240. A. Corma, U. Diaz, V. Fornes, J. L. Jorda, M. Domine and F. Rey, *Chem. Commun. (Cambridge, U. K.)*, 1999, 779-780.

241. M. Vaarkamp, J. V. Grondelle, J. T. Miller, D. J. Sajkowski, F. S. Modica, G. S. Lane, B. C. Gates and D. C. Koningsberger, *Catal. Lett.*, 1990, **6**, 369-382.

242. M. M. Otten, M. J. Clayton and H. H. Lamb, *J. Catal.*, 1994, **149**, 211-222.

243. G. S. Lane, F. S. Modica and J. T. Miller, *J. Catal.*, 1991, **129**, 145-158.

244. K. Gora-Marek, K. A. Tarach, Z. Piwowarska, M. Laniecki and L. Chmielarz, *Catal. Sci. Tech.*, 2016, **6**, 1651-1660.

245. H. Yang, C. Ma, X. Zhang, Y. Li, J. Cheng and Z. Hao, *ACS Catal.*, 2018, **8**, 1248-1258.

246. K.-I. Shimizu and A. Satsuma, *Phys. Chem. Chem. Phys.*, 2006, **8**, 2677-2695.

247. J. Shibata, K.-i. Shimizu, Y. Takada, A. Shichi, H. Yoshida, S. Satokawa, A. Satsuma and T. Hattori, *J. Catal.*, 2004, **227**, 367-374.

248. A. Satsuma, J. Shibata, K. Shimizu and T. Hattori, *Catal. Surv. Asia*, 2005, **9**, 75-85.

249. K.-I. Shimizu, K. Sugino, K. Kato, S. Yokota, K. Okumura and A. Satsuma, *J. Phys. Chem. C*, 2007, **111**, 1683-1688.

250. V. L. Sushkevich, D. Palagin, M. Ranocchiari and J. A. van Bokhoven, *Science*, 2017, **356**, 523-527.

251. S. Grundner, M. A. C. Markovits, G. Li, M. Tromp, E. A. Pidko, E. J. M. Hensen, A. Jentys, M. Sanchez-Sanchez and J. A. Lercher, *Nat. Commun.*, 2015, **6**, 7546-7555.

252. M. J. Wulfers, S. Teketel, B. Ipek and R. F. Lobo, *Chem. Commun. (Cambridge, U. K.)*, 2015, **51**, 4447-4450.

253. J. Shan, W. Huang, L. Nguyen, Y. Yu, S. Zhang, Y. Li, A. I. Frenkel and F. Tao, *Langmuir*, 2014, **30**, 8558-8569.

254. P. P. Knops-Gerrits and W. A. Goddard, *J. Mol. Catal. A: Chem.*, 2001, **166**, 135-145.

255. E. V. Starokon, M. V. Parfenov, L. V. Pirutko, S. I. Abornev and G. I. Panov, *J. Phys. Chem. C*, 2011, **115**, 2155-2161.

256. E. A. Turitsyna, V. M. Trukhan and A. A. Shteinman, *Russ. Chem. Bull.*, 2011, **60**, 2088-2093.

257. V. R. Choudhary, A. K. Kinage and T. V. Choudhary, *Science*, 1997, **275**, 1286-1288.

258. W. Xiumei, Q. Guodong, X. Jun, L. Bojie, W. Chao and D. Feng, *Angew. Chem., Int. Ed.*, 2012, **51**, 3850-3853.

259. M. A. Culpepper and A. C. Rosenzweig, *Crit. Rev. Biochem. Mol. Biol.*, 2012, **47**, 483-492.

260. K. Yoshizawa, A. Suzuki, Y. Shiota and T. Yamabe, *Bull. Chem. Soc. Jpn.*, 2000, **73**, 815-827.
261. M. Ichikawa, *Platin. Met. Rev.*, 2000, **44**, 3-14.
262. A. Corma and H. Garcia, *Eur. J. Inorg. Chem.*, 2004, **2004**, 1143-1164.
263. B. C. Gates, *Chem. Rev. (Washington, DC, U. S.)*, 1995, **95**, 511-522.
264. P. Serna and B. C. Gates, *Acc. Chem. Res.*, 2014, **47**, 2612-2620.
265. B. C. Gates, in *Stud. Surf. Sci. Catal.*, eds. M. Absi-Halabi, J. Beshara and A. Stanislaus, Elsevier, 1996, vol. 100, pp. 49-63.
266. L. F. Rao, A. Fukuoka, N. Kosugi, H. Kuroda and M. Ichikawa, *J. Phys. Chem.*, 1990, **94**, 5317-5327.
267. U. Alper and G. B. C., *Angew. Chem., Int. Ed.*, 2008, **47**, 9245-9248.
268. P. Serna and B. C. Gates, *J. Am. Chem. Soc.*, 2011, **133**, 4714-4717.
269. D. Yardimci, P. Serna and B. C. Gates, *Chem. Eur. J.*, 2013, **19**, 1235-1245.
270. A. Uzun and B. C. Gates, *J. Am. Chem. Soc.*, 2009, **131**, 15887-15894.
271. J. Lu, B. Fu, M. C. Kung, G. Xiao, J. W. Elam, H. H. Kung and P. C. Stair, *Science*, 2012, **335**, 1205-1208.
272. J. Lu, J. W. Elam and P. C. Stair, *Acc. Chem. Res.*, 2013, **46**, 1806-1815.
273. S. L. Wegener, T. J. Marks and P. C. Stair, *Acc. Chem. Res.*, 2012, **45**, 206-214.
274. Z. Gao and Y. Qin, *Acc. Chem. Res.*, 2017, **50**, 2309-2316.
275. D. Xu, B. Wu, P. Ren, S. Wang, C. Huo, B. Zhang, W. Guo, L. Huang, X. Wen, Y. Qin, Y. Yang and Y. Li, *Catal. Sci. Tech.*, 2017, **7**, 1342-1350.
276. M. T. Reetz and W. Helbig, *J. Am. Chem. Soc.*, 1994, **116**, 7401-7402.
277. N. Vilar-Vidal, M. C. Blanco, M. A. López-Quintela, J. Rivas and C. Serra, *J. Phys. Chem. C*, 2010, **114**, 15924-15930.
278. N. Vilar-Vidal, J. Rivas and M. A. López-Quintela, *ACS Catal.*, 2012, **2**, 1693-1697.
279. B. S. Gonzalez, M. C. Blanco and M. A. Lopez-Quintela, *Nanoscale*, 2012, **4**, 7632-7635.
280. A. Corma, P. Concepción, M. Boronat, M. J. Sabater, J. Navas, M. J. Yacaman, E. Larios, A. Posadas, M. A. López-Quintela, D. Buceta, E. Mendoza, G. Guilera and A. Mayoral, *Nat. Chem.*, 2013, **5**, 775-781.
281. M. Moliner, J. E. Gabay, C. E. Kliewer, R. T. Carr, J. Guzman, G. L. Casty, P. Serna and A. Corma, *J. Am. Chem. Soc.*, 2016, **138**, 15743-15750.
282. L. Liu, D. N. Zakharov, R. Arenal, P. Concepcion, E. A. Stach and A. Corma, *Nat. Commun.*, 2018, **9**, 1-10.
283. C. Paolucci, J. R. Di Iorio, F. H. Ribeiro, R. Gounder and W. F. Schneider, in *Advances in Catalysis, Vol 59*, ed. C. Song, 2016, vol. 59, pp. 1-107.
284. D. W. Fickel, E. D'Addio, J. A. Lauterbach and R. F. Lobo, *Appl. Catal., B*, 2011, **102**, 441-448.
285. C. Paolucci, A. A. Parekh, I. Khurana, J. R. Di Iorio, H. Li, J. D. Albarracin Caballero, A. J. Shih, T. Anggara, W. N. Delgass, J. T. Miller, F. H. Ribeiro, R. Gounder and W. F. Schneider, *J. Am. Chem. Soc.*, 2016, **138**, 6028-6048.
286. S. A. Bates, A. A. Verma, C. Paolucci, A. A. Parekh, T. Anggara, A. Yezerets, W. F. Schneider, J. T. Miller, W. N. Delgass and F. H. Ribeiro, *J. Catal.*, 2014, **312**, 87-97.
287. A. M. Beale, I. Lezcano-Gonzalez, W. A. Slawinksi and D. S. Wragg, *Chem. Commun. (Cambridge, U. K.)*, 2016, **52**, 6170-6173.
288. F. Gao, E. D. Walter, M. Kollar, Y. Wang, J. Szanyi and C. H. F. Peden, *J. Catal.*, 2014, **319**, 1-14.
289. C. Paolucci, I. Khurana, A. A. Parekh, S. Li, A. J. Shih, H. Li, J. R. Di Iorio, J. D. Albarracin-Caballero, A. Yezerets, J. T. Miller, W. N. Delgass, F. H. Ribeiro, W. F. Schneider and R. Gounder, *Science (Washington, DC, U. S.)*, 2017, **357**, 898-903.
290. F. Gao, D. Mei, Y. Wang, J. Szanyi and C. H. F. Peden, *J. Am. Chem. Soc.*, 2017, **139**, 4935-4942.
291. S. Brandenberger, O. Kröcher, A. Tissler and R. Althoff, *Catal. Rev.*, 2008, **50**, 492-531.
292. L. Liu and A. Corma, *Chem. Rev. (Washington, DC, U. S.)*, 2018, **118**, 4981–5079.

293. A. Primo and H. Garcia, *Chem. Soc. Rev.*, 2014, **43**, 7548-7561.
294. M. Guisnet, *Catal. Today*, 2013, **218-219**, 123-134.
295. K. Fujimoto, K. Maeda and K. Aimoto, *Appl. Catal., A*, 1992, **91**, 81-86.
296. A. Zhang, I. Nakamura, K. Aimoto and K. Fujimoto, *Ind. Eng. Chem. Res.*, 1995, **34**, 1074-1080.
297. F. Roessner and U. Roland, *J. Mol. Catal. A: Chem.*, 1996, **112**, 401-412.
298. F. Roessner, U. Roland and T. Braunschweig, *J. Chem. Soc., Faraday Trans.*, 1995, **91**, 1539-1545.
299. H. Y. Chu, M. P. Rosynek and J. H. Lunsford, *J. Catal.*, 1998, **178**, 352-362.
300. F. Lonyi, A. Kovacs, A. Szegedi and J. Valyon, *J. Phys. Chem. C*, 2009, **113**, 10527-10540.
301. H. Chiang and A. Bhan, *J. Catal.*, 2011, **283**, 98-107.
302. J. Pastvova, D. Kaucky, J. Moravkova, J. Rathousky, S. Sklenak, M. Vorokhta, L. Brabec, R. Pilar, I. Jakubec, E. Tabor, P. Klein and P. Sazama, *ACS Catal.*, 2017, **7**, 5781-5795.
303. D. Jin, G. Ye, J. Zheng, W. Yang, K. Zhu, M.-O. Coppens and X. Zhou, *ACS Catal.*, 2017, **7**, 5887-5902.
304. T. Yue, W. Liu, L. Li, X. Zhao, K. Zhu, X. Zhou and W. Yang, *J. Catal.*, 2018, **364**, 308-327.
305. J. Kim, W. Kim, Y. Seo, J.-C. Kim and R. Ryoo, *J. Catal.*, 2013, **301**, 187-197.
306. P. Sazama, J. Pastvova, D. Kaucky, J. Moravkova, J. Rathousky, I. Jakubec and G. Sadovska, *J. Catal.*, 2018, **364**, 262-270.
307. V. M. Akhmedov and S. H. Al-Khowaiter, *Catal. Rev. - Sci. Eng.*, 2007, **49**, 33-139.
308. J. A. Martens, W. Souverijns, W. Verrelst, R. Parton, G. F. Groment and P. A. Jacobs, *Angew. Chem., Int. Ed. Engl.*, 1995, **34**, 2528-2530.
309. J. A. Martens, G. Vanbutsele, P. A. Jacobs, J. Denayer, R. Ocakoglu, G. Baron, J. A. Munoz Arroyo, J. Thybaut and G. B. Marin, *Catal. Today*, 2001, **65**, 111-116.
310. G. Sastre, A. Chica and A. Corma, *J. Catal.*, 2000, **195**, 227-236.
311. Y. Bi, G. Xia, W. Huang and H. Nie, *RSC Adv.*, 2015, **5**, 99201-99206.
312. S. Liu, J. Ren, S. Zhu, H. Zhang, E. Lv, J. Xu and Y.-W. Li, *J. Catal.*, 2015, **330**, 485-496.
313. P. Niu, H. Xi, J. Ren, M. Lin, Q. Wang, L. Jia, B. Hou and D. Li, *Catal. Sci. Technol.*, 2017, **7**, 5055-5068.
314. D. Verboekend, K. Thomas, M. Milina, S. Mitchell, J. Perez-Ramirez and J.-P. Gilson, *Catal. Sci. Technol.*, 2011, **1**, 1331-1335.
315. J. A. Martens, D. Verboekend, K. Thomas, G. Vanbutsele, J.-P. Gilson and J. Perez-Ramirez, *ChemSusChem*, 2013, **6**, 421-425.
316. X. Wu, M. Qiu, X. Chen, G. Yu, X. Yu, C. Yang, J. Sun, Z. Liu and Y. Sun, *New J. Chem.*, 2018, **42**, 111-117.
317. M. Y. Kim, K. Lee and M. Choi, *J. Catal.*, 2014, **319**, 232-238.
318. S. Tao, X. Li, G. Lv, C. Wang, R. Xu, H. Ma and Z. Tian, *Catal. Sci. Technol.*, 2017, **7**, 5775-5784.
319. F. Zhang, Y. Liu, Q. Sun, Z. Dai, H. Gies, Q. Wu, S. Pan, C. Bian, Z. Tian, X. Meng, Y. Zhang, X. Zou, X. Yi, A. Zheng, L. Wang and F.-S. Xiao, *Chem. Commun. (Cambridge, U. K.)*, 2017, **53**, 4942-4945.
320. O. Ben Moussa, L. Tinat, X. Jin, W. Baaziz, O. Durupthy, C. Sayag and J. Blanchard, *ACS Catal.*, 2018, **8**, 6071-6078.
321. H. Sammoury, J. Toufaily, K. Cherry, T. Hamieh, Y. Pouilloux and L. Pinard, *Appl. Catal., A*, 2018, **551**, 1-12.
322. N. Batalha, L. Pinard, C. Bouchy, E. Guillon and M. Guisnet, *J. Catal.*, 2013, **307**, 122-131.
323. Y. Wang, Z. Tao, B. Wu, J. Xu, C. Huo, K. Li, H. Chen, Y. Yang and Y. Li, *J. Catal.*, 2015, **322**, 1-13.
324. C. S. Song, *Chemtech*, 1999, **29**, 26-30.
325. H. Yang, H. Chen, J. Chen, O. Omotoso and Z. Ring, *J. Catal.*, 2006, **243**, 36-42.
326. J. Álvarez-Rodríguez, A. Guerrero-Ruiz, I. Rodríguez-Ramos and A. Arcoya-Martín, *Catal. Today*, 2005, **107-108**, 302-309.

327. J. Álvarez-Rodríguez, I. Rodríguez-Ramos, A. Guerrero-Ruiz, E. Gallegos-Suarez and A. Arcoya, *Chem. Eng. J. (Lausanne)*, 2012, **204-206**, 169-178.
328. P. Concepcion, Y. Perez, J. C. Hernandez-Garrido, M. Fajardo, J. J. Calvino and A. Corma, *Phys. Chem. Chem. Phys.*, 2013, **15**, 12048-12055.
329. P. D. Zgolicz, V. I. Rodríguez, I. M. J. Vilella, S. R. de Miguel and O. A. Scelza, *Appl. Catal. A, Gen.*, 2011, **392**, 208-217.
330. J. Gu, Z. Zhang, L. Ding, K. Huang, N. Xue, L. Peng, X. Guo and W. Ding, *Catal. Commun.*, 2017, **97**, 98-101.
331. M. Boronat and A. Corma, *Dalton Trans.*, 2010, **39**, 8538-8546.
332. R. Pal, L.-M. Wang, Y. Pei, L.-S. Wang and X. C. Zeng, *J. Am. Chem. Soc.*, 2012, **134**, 9438-9445.
333. B. Taylor, J. Lauterbach and W. N. Delgass, *Appl. Catal. A, Gen.*, 2005, **291**, 188-198.
334. J. J. Bravo-Suarez, K. K. Bando, J. Lu, M. Haruta, T. Fujitani and S. T. Oyama, *J. Phys. Chem. C*, 2008, **112**, 1115-1123.
335. L. Xu, Y. Ren, H. Wu, Y. Liu, Z. Wang, Y. Zhang, J. Xu, H. Peng and P. Wu, *J. Mater. Chem.*, 2011, **21**, 10852-10858.
336. M. H. Groothaert, P. J. Smeets, B. F. Sels, P. A. Jacobs and R. A. Schoonheydt, *J. Am. Chem. Soc.*, 2005, **127**, 1394-1395.
337. J. S. Woertink, P. J. Smeets, M. H. Groothaert, M. A. Vance, B. F. Sels, R. A. Schoonheydt and E. I. Solomon, *Proc. Natl. Acad. Sci. U. S. A.*, 2009, **106**, 18908-18913.
338. S. Grundner, W. Luo, M. Sanchez-Sanchez and J. A. Lercher, *Chem. Commun. (Cambridge, U. K.)*, 2016, **52**, 2553-2556.
339. G. I. Panov, V. I. Sobolev, K. A. Dubkov, V. N. Parmon, N. S. Ovanesyan, A. E. Shilov and A. A. Shteinman, *React. Kinet. Catal. Lett.*, 1997, **61**, 251-258.
340. N. S. Ovanesyan, A. A. Shteinman, K. A. Dubkov, V. I. Sobolev and G. I. Panov, *Kinet. Catal.*, 1998, **39**, 792-797.
341. P. Vanelderen, B. E. R. Snyder, M.-L. Tsai, R. G. Hadt, J. Vancauwenbergh, O. Coussens, R. A. Schoonheydt, B. F. Sels and E. I. Solomon, *J. Am. Chem. Soc.*, 2015, **137**, 6383-6392.
342. K. Narsimhan, K. Iyoki, K. Dinh and Y. Román-Leshkov, *ACS Cent. Sci.*, 2016, **2**, 424-429.
343. K. Narsimhan, V. K. Michaelis, G. Mathies, W. R. Gunther, R. G. Griffin and Y. Román-Leshkov, *J. Am. Chem. Soc.*, 2015, **137**, 1825-1832.
344. J. Shan, M. Li, L. F. Allard, S. Lee and M. Flytzani-Stephanopoulos, *Nature*, 2017, **551**, 605.
345. J. J. Spivey and G. Hutchings, *Chem. Soc. Rev.*, 2014, **43**, 792-803.
346. W. Ding, S. Li, G. D Meitzner and E. Iglesia, *J. Phys. Chem. B*, 2001, **105**, 506-513.
347. H. Zheng, D. Ma, X. Bao, J. Z. Hu, J. H. Kwak, Y. Wang and C. H. F. Peden, *J. Am. Chem. Soc.*, 2008, **130**, 3722-3723.
348. N. Kosinov, A. S. G. Wijpkema, E. Uslamin, R. Rohling, F. J. A. G. Coumans, B. Mezari, A. Parastaev, A. S. Poryvaev, M. V. Fedin, E. A. Pidko and E. J. M. Hensen, *Angew. Chem., Int. Ed.*, 2018, **57**, 1016-1020.
349. Y. Xiao and A. Varma, *ACS Catal.*, 2018, **8**, 2735-2740.
350. G. Centi, E. A. Quadrelli and S. Perathoner, *Energy Environ. Sci.*, 2013, **6**, 1711-1731.
351. H. Yang, C. Zhang, P. Gao, H. Wang, X. Li, L. Zhong, W. Wei and Y. Sun, *Catal. Sci. Technol.*, 2017, **7**, 4580-4598.
352. O. B. Ayodele, *J. CO2 Utilization*, 2017, **20**, 368-377.
353. W. J. Shen, K. W. Jun, H. S. Choi and K. W. Lee, *Korean J. Chem. Eng.*, 2000, **17**, 210-216.
354. J. A. Rodriguez, J. Evans, L. Feria, A. B. Vidal, P. Liu, K. Nakamura and F. Illas, *J. Catal.*, 2013, **307**, 162-169.
355. J. Ye, C.-j. Liu, D. Mei and Q. Ge, *J. Catal.*, 2014, **317**, 44-53.
356. Y.-X. Pan, C.-J. Liu and Q. Ge, *J. Catal.*, 2010, **272**, 227-234.
357. B. M. Szyja, D. Smykowski, J. Szczygieł, E. J. M. Hensen and E. A. Pidko, *ChemCatChem*, 2016, **8**, 2500-2507.

358. Z. Li, J. Wang, Y. Qu, H. Liu, C. Tang, S. Miao, Z. Feng, H. An and C. Li, *ACS Catal.*, 2017, **7**, 8544-8548.
359. P. Gao, S. Dang, S. Li, X. Bu, Z. Liu, M. Qiu, C. Yang, H. Wang, L. Zhong, Y. Han, Q. Liu, W. Wei and Y. Sun, *ACS Catal.*, 2018, **8**, 571-578.
360. P. Gao, S. Li, X. Bu, S. Dang, Z. Liu, H. Wang, L. Zhong, M. Qiu, C. Yang, J. Cai, W. Wei and Y. Sun, *Nat. Chem.*, 2017, **9**, 1019-1024.
361. J. Wei, Q. Ge, R. Yao, Z. Wen, C. Fang, L. Guo, H. Xu, J. Sun, J. Wei, R. Yao, Z. Wen and L. Guo, *Nat Commun*, 2017, **8**, 15174.
362. C. Wang, Z. Liu, L. Wang, X. Dong, J. Zhang, G. Wang, S. Han, X. Meng, A. Zheng and F.-S. Xiao, *ACS Catal.*, 2018, **8**, 474-481.
363. W. Dai, S. Zhang, Z. Yu, T. Yan, G. Wu, N. Guan and L. Li, *ACS Catal.*, 2017, **7**, 3703-3706.
364. Z. Jian, W. Liang, Z. Longfeng, W. Qinming, C. Chunyu, W. Xiong, J. Yanyan, M. Xiangju and X. Feng-Shou, *ChemSusChem*, 2015, **8**, 2867-2871.
365. G. M. Lari, Z. Chen, C. Mondelli and J. Pérez-Ramírez, *ChemCatChem*, 2017, **9**, 2195-2202.
366. N. Wang, Q. Sun, R. Bai, X. Li, G. Guo and J. Yu, *J. Am. Chem. Soc.*, 2016, **138**, 7484-7487.
367. Q. M. Sun, N. Wang, Q. M. Bing, R. Si, J. Y. Liu, R. S. Bai, P. Zhang, M. J. Jia and J. H. Yu, *Chem*, 2017, **3**, 477-493.